Response and Recovery of Turbulent Pipeflow Past Wall Changes Targeting Distinct Azimuthal Fourier Modes

by

Mehran Masoumifar

A thesis submitted in partial fulfilment of the requirements for the degree of

Master of Science

Department of Mechanical Engineering

University of Alberta

ABSTRACT

This study focuses on numerical evaluation of the response and recovery of turbulent pipe flow to three-dimensional perturbed wall changes at a range of Reynolds numbers. These perturbations (pipe inserts) were designed based on distinct azimuthal Fourier modes corresponding to $m = 3$ (Case I), $m = 15$ (Case II), and their superposition at $m \in 3 + 15$ (Case III). A thorough validation and verification analysis enabled creating a benchmark study in simulating perturbed wall-bounded turbulent flows using turbulence models. The long-lasting response of the flow and the recovery was examined by characterizing both the mean and turbulent fields in the wake of pipe inserts for each Reynolds number. Although a fast turbulence decay was observed immediately past the perturbation for all cases at higher Reynolds numbers, Case I showed a faster overall recovery compared to the other two cases with higher Fourier Modes. The flow response for Case I depicted a monotonic response, while the other two cases presented a non-monotonic second-order response characteristic along with a delayed recovery trend. Dominant flow structures were further identified in the downstream wake of each wall shape, which enabled a qualitative description of potential mechanisms behind the observed recovery trends. This study was then extended to the implications of Reynolds number. Increasing the Reynolds number was identified to prolong the flow recovery until it approached an asymptotic range at $Re \geq 7.5 \times 10^4$. The recovery trend was scaled with Re^4 for both the mean velocity and turbulence kinetic energy. In addition, the mean velocity along the wake centerline showed two peaks, where the location of peaks followed a power-law trend in the form of $L_p/D \propto Re^{4/3}$. The long-lasting flow response impeded the return to the fully-relaxed state at a distance of $20D$, even for the lowest Reynolds number considered here. Overall, the recovery exhibited a second-order response. This study provides a thorough characterization of targeted turbulent pipe flow response and recovery with applications in flow manipulation in pipelines for reduced drag, improved efficiency, lower rates of erosion and corrosion, as well as lower greenhouse gas emission for energy transportation.

PREFACE

The results of Chapter 5 were published in *Physics of Fluids* Journal with the following citation:

> Masoumifar, M., Verma, S., Hemmati, A. (2021). Response of turbulent pipe flow to targeted wall shapes at a range of Reynolds number. *Physics of Fluids, 33(6), 065105.*

The results from Chapter 4 are currently under review for publication in the *International Journal of Heat and Fluid Flow*:

> Masoumifar, M., Verma, S., Hemmati, A. (2021). Effects of targeted wall geometries on response of turbulent pipe flow at high Reynolds number. *Intr. J. Heat and Fluid Flow.* (*Under Review*)

The results of Chapter 3 is currently under review for publication in the *Journal of Fluids Engineering*:

> Masoumifar, M., Verma, S., Hemmati, A. (2021). How turbulence models perform in simulating pipeflow response to targeted wall-shapes?. *Journal of Fluids Engineering.* (*Under Review*)

All the simulations, data analysis, and results interpretation included in this thesis were performed by Mehran Masoumifar under the supervision of Dr. Arman Hemmati. The simulations were carried out using Compute Canada clusters. The co-author in the aforementioned papers provided assistance in the initial planning of simulations, support in discussions, and editorial input by reviewing manuscripts prior to submission. The results provided and discussion included in this dissertation are based on the work of Mehran Masoumifar, who led the authorship of manuscripts.

"Dedicated to my dear parents and brother, ***Esfandiar****,* ***Fatemeh****, and* ***Erfan****"*

For their love, endless support, encouragement, and sacrifices

ACKNOWLEDGEMENTS

Many people helped broaden my horizons at the University of Alberta, and simple words cannot sufficiently express my sincerest gratitude to them. First and foremost, I would like to thank my research supervisor, Dr. Arman Hemmati, whose key insights, helpful suggestions, and timely encouragement are reflected throughout the present studies. His guidance indeed enriched my research skills. To my academic family, Department of Mechanical Engineering and Computational Fluid Engineering Laboratory, I would like to thank you for giving me the opportunity to continue my studies at the University of Alberta. I am grateful for the positive and insightful conversations I had with colleagues and friends for their invaluable guidance. Next, I am thankful for the endless support of my parents, my brother, and other family members. They have been a source of unwavering love, encouragement, and support in all phases of my life. I would also like to acknowledge the generous financial support provided by Alberta Innovates and Canada First Research Excellence. Lastly, I want to voice my gratitude to healthcare workers during the *COVID-19* pandemic for their sacrifices.

To all those through whom this thesis is possible, I am forever grateful.

Contents

List of Tables

List of Figures

LIST OF ABBREVIATIONS, SYMBOLS, AND NOMENCLATURE

Latin Symbols

h	height
D	diameter
R	radius
x	axial location
r	radial direction
θ	azimuthal angle
A	cross-sectional area
Re	Reynolds number
Re_τ	friction Reynolds number
k	turbulence kinetic energy
I	turbulence intensity
U_b	bulk velocity in far downstream region
U_∞	bulk velocity at the inlet of smooth-wall pipe
U_{CL}	centerline velocity value
u_τ	bulk inlet friction velocity
$\overline{U_x}$	Cylindrical axial ($x-$wise) velocity component
$\overline{U_r}$	Cylindrical radial ($r-$wise) velocity component
$\overline{U_\theta}$	Cylindrical azimuthal ($\theta-$wise) velocity component
$\overline{u_x u_r}$	Reynolds shear stress component
$\overline{u_x}^2$	Reynolds normal stress component
P	pressure

P_k	turbulence kinetic energy production
L_r	recovery location
L_p	location of maximum $\overline{U_x}$
L_{pipe}	total length of the pipe
m	Fourier mode number
a_m	perturbation amplitude
Q	Q-criterion
U_η	velocity scale of the core flow region
F	force vector
c	characteristic length scale
u	velocity scale
τ_η	Kolmogorov time scale
t	time
T	averaging time interval

Greek Symbols

δ	boundary layer thickness
ρ	density
μ	dynamic viscosity
ν	kinematic viscosity
σ_{ij}	stress tensor
ε	turbulence kinetic energy dissipation rate
ω	turbulence specific dissipation rate
η	Kolmogorov length scale

φ	any flow variable

Other Symbols

∇	gradient operator
∂	partial derivative
δ	difference
$\overline{\square}$	mean value (time-averaged)
$\approx$	approximately
$\sum$	summation
$\propto$	proportional to
$\square^{\circ}$	angle of the wall displacement
$\equiv$	equivalent to

Abbreviations

$2D$	Two Dimensional
$3D$	Three Dimensional
CFD	Computational Fluid Dynamics
FVM	Finite Volume Method
DNS	Direct Numerical Simulation
LES	Large Eddy Simulation
$RANS$	Reynolds-Averaged Navier-Stokes
SST	Shear Stress Transport
RNG	Reynolds Normalization Group
PIV	Particle Image Velocimetry

LSMs	Large-Scale Motions
VLSMs	Very-Large-Scale Motions
SIMPLE	Semi-Implicit Method for Pressure-Linked Equations

Chapter 1

INTRODUCTION

The response and recovery of pipe flow perturbed by targeted wall shapes, corresponding to certain azimuthal Fourier modes, is essential in fundamental understanding of turbulent flow dynamics. Particularly, this study sets the platform to investigate the dynamics of Large-Scale Motions (Jiménez, 1998; Balakumar and Adrian, 2007) and Very-Large-Scale Motions (Kim and Adrian, 1999; Guala et al., 2006), as well as their manipulation implications on flow response and recovery. Using computational fluid dynamics (CFD), the flow past targeted perturbations (pipe-inserts) were examined in three dimensions. Three distinct wall geometries were simulated at a wide range of Reynolds numbers, which corresponded to $Re = U_\infty D/\nu = 5 \times 10^3 - 1.58 \times 10^5$. Here, D is the pipe diameter, ν is the fluid kinematic viscosity, and U_∞ is the bulk inlet velocity. This works expands on the experiments of Van Buren et al. (2017) on turbulent pipe flow over pipe-inserts with walls shapes based on certain azimuthal Fourier modes. This dissertation investigates the implications of three wall shapes (Figure 1.1) targeting Fourier modes $m = 3$, 15, and $3 + 15$ at a range of Re.

1.1 Overview

Since the pioneering work of Ludwig Prandtl in 1904 on the boundary layer theory development of viscous flows (Schlichting and Gersten, 2016), there have been numerous studies

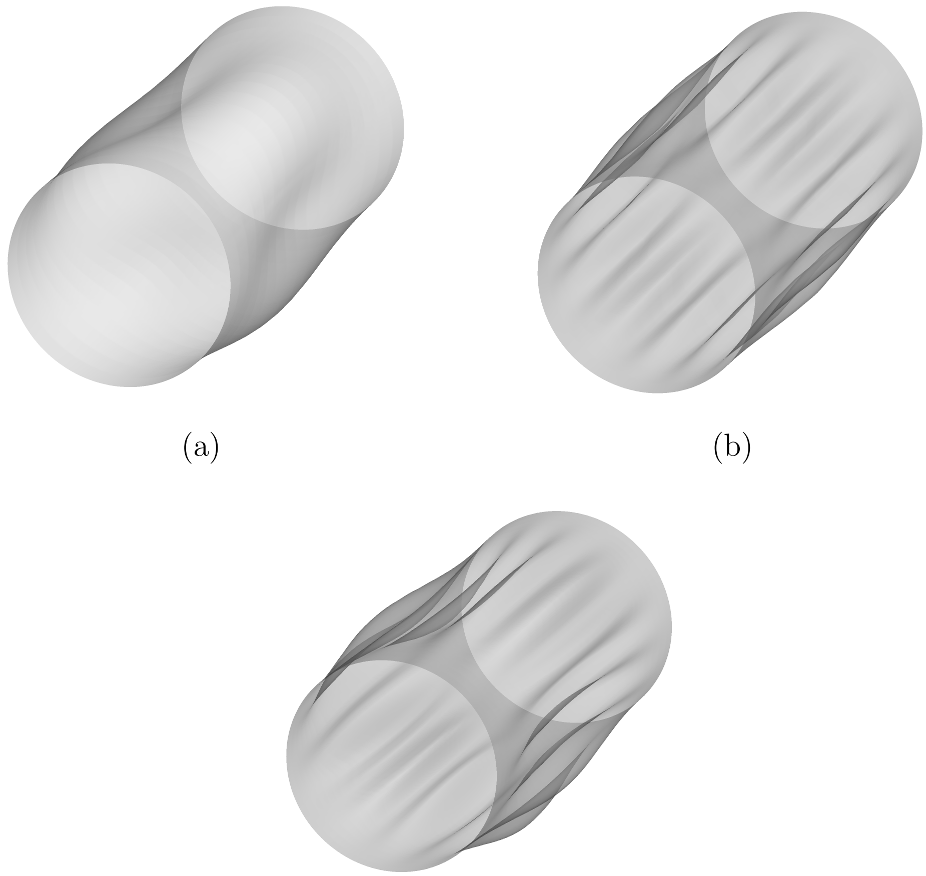

(a) (b)

(c)

Figure 1.1: Schematics of the pipe-insert resembling Fourier mode (a) $m = 3$, (b) $m = 15$, and (c) $m \in 3 + 15$.

attempted to characterize (Bradshaw and Wong, 1972; Balachandar, 1990), scale (Roache, 1982; Zagarola and Smits, 1998), and model (Deardorff et al., 1970; Launder and Spalding, 1983; Wilcox et al., 1998) the dynamics of separated flows. These phenomena can be found in internal (Simpson, 1989) and external (Von Kármán, 1963) flows alike, where the flow separation past wall-mounted obstacles or the existence of steps in elevation is often accompanied by a reattachment. This has been a challenging topic for modeling and predicting various turbulence behaviors (Good and Joubert, 1968; Eaton and Johnston, 1981; Adams and Johnston, 1988; Tomas et al., 2015; Van der Kindere and Ganapathisubramani, 2018). The flow separation is of considerable interest for several reasons. In the engineering context, rough surfaces may be used to enhance heat transfer, delay transition, reduce drag, low pressure loss, improve turbulence mixing, and manipulate the rate of erosion and corrosion (Nesic and Postlethwaite, 1990; Leonardi et al., 2003). Their application includes a wide range of engineering configurations, including pipes (Shah et al., 2012; Yamagata et al., 2014) and channel flows (Kim et al., 2001; Saito and Pullin, 2014), as well as external flows, i.e., flow over buildings in urban areas (Paterson and Apelt, 1989; Baskaran and Kashef, 1996), flow over vehicles (Hucho and Sovran, 1993; Katz, 2006), and flow past fixed-wing aircrafts (Ravindran, 1999; Gursul et al., 2014). The particular application that motivated this dissertation, however, was on lowering the greenhouse gas emissions associated with energy transportation using pipelines through enhanced axial flow acceleration, increased mixing that reduces condensation and slugging, lowered pressure losses, and minimized rates of erosion and corrosion.

Many researchers focused on the flow separation phenomenon induced by sudden variations of the wall condition over the past decades. This included large-step (defined as $h/\delta \gg 1$, where h is the perturbation height and δ presents the boundary layer thickness), small-step ($h/\delta \ll 1$), and smooth-curved boundaries. The large and small-step wall-mounted obstacles, such as backward and forward-facing steps, produced a single separation point followed by a wake region, which is not affected by the far-downstream flow conditions, i.e., presence of another perturbation. In particular, a large backward-facing step has been the topic of interest for numerous studies that characterized flow over abrupt changes in surface conditions (Bradshaw and Wong, 1972; Adams and Johnston, 1988; Simpson, 1989; Jovic and Driver, 1995). In case of internal flows, pipe flow past sudden perturbations were shown to experience contraction and thereby exhibit a class of out-of-equilibrium flows with complex characteristics (Smits et al., 1979, 2019). As a result, the flow response to the step-change revealed an overshoot of flow parameters in the regions close to perturbation, i.e., amplification of Reynolds stresses, larger pressure gradients. This introduced long-lasting changes of flow structures in the wake region that extended far downstream. Therefore, extensive studies have explored the immediate flow response and recovery past large-step wall-mounted obstacles in pipes and channels (Smits et al., 1979; Durst and Wang, 1989; Yamagata et al., 2014; Smits et al., 2019; Martinuzzi and Tropea, 1993; Leonardi et al., 2003). However, limited studies focused on the flow over small steps or perturbations. The early experimental studies of this topic, such as Durst and Tropea (1983) and Perić and Tropea (1993), investigated the turbulent flow over surface-mounted obstacles in plane and axisymmetric geometries. Later, Durst and Wang (1989) experimentally studied the response of turbulent flow past an axisymmetric small-step obstacle at a range of Reynolds numbers. This was then expanded by the experiment of Jiménez (2004), who suggested that small steps acting as isolated roughness elements have a considerable impact on the wake characteristics. More recently, Smits et al. (2019) experimentally investigated the turbulent pipe flow perturbed by a single thin square bar roughness element with bar heights of $0.05D$ and $0.1D$ at $Re = 1.56 \times 10^5$. Their analysis included the flow response and quantification of the recovery process by tracing the transport of Reynolds shear stress in the wake zone. They also observed a prolonged recovery behavior for the flow past the smaller roughness element that implied an extended region of lower skin friction downstream of the perturbation. Smits et al. (2019) looked at the feasibility of introducing sudden periodic changes in surface conditions to achieve an extended zone of lower turbulence levels, lower surface friction, and reduced drag. However, their study was limited in terms of introducing detailed recovery mechanisms and their effects with respect to Reynolds number. This was then expanded by Goswami and Hemmati (2020, 2021), who investigated the response and recovery of turbulent pipe flow over single and multiple tandem square bar roughness elements. They addressed previous experimental knowledge limitations by conducting numerical simulations using a larger domain and a wider range of Reynolds numbers ($5 \times 10^3 - 1.56 \times 10^5$).

Past studies have revealed some intriguing aspects of high Reynolds number turbulent flows subjected to small abrupt changes in surface conditions. For example, in the recent experiment of Van Buren et al. (2017) the wall shape varied sinusoidally in the axial direction, and the maximum perturbation height was comparable to the experiments of Smits et al. (2019). Their study was mainly focused on manipulation of the Large-Scale Motions (LSMs) and Very-Large-Scale Motions (VLSMs) in wall-bounded turbulence by designing the circumferential wall-shape based on specific azimuthal Fourier modes. However, there are no comprehensive studies that look at the flow response and recovery for this particular problem over a large range of Reynolds numbers. The current study addressed the existing gap in the literature on characterizing the response and recovery of turbulent pipe flow with targeted perturbations at a wide range of Reynolds numbers.

This work is part of a larger project that looks at new technologies to improve the efficiency of pipes for energy transportation towards lower greenhouse gas emissions. Thus, the application of this work in the energy industry, especially in Alberta, is enormous. However, the fundamental aspects of this study has a broad reach in industrial applications, such as sewage systems, water treatment plants, geothermal infrastructure, coolant systems, heat exchangers, and space vehicles. Here, the principal interest is in designing energy transport pipelines to provide operational benefits while enhancing the life span of facilities and reducing maintenance costs. For example, the presence of high viscous fluids, e.g., crude oil bitumen (Muñoz et al., 2016), amplifies the wall shear stress and increases friction on the pipe walls. This is also the case for water sewage pipelines, where the fluid has a mixture of various phases, i.e., dilute, slurry. Besides, blockades in pipeline systems resulting from slog formation is another prominent issue that needs to be considered while designing the system (Mendes et al., 1999). In the energy industry, abrupt variations in the form of steps (Perić and Tropea, 1993), roughness elements (Smits et al., 2019) and smooth-wall variations (Van Buren et al., 2017) can be manipulated to introduce flow disturbances and improve mixing to decrease the rate of corrosion and erosion (Ilman et al., 2014). Moreover, Smits et al. (2019) recommended that introducing sudden wall-changes in the periodic patterns can provide extended regions of lower drag in the downstream wake by minimizing pressure

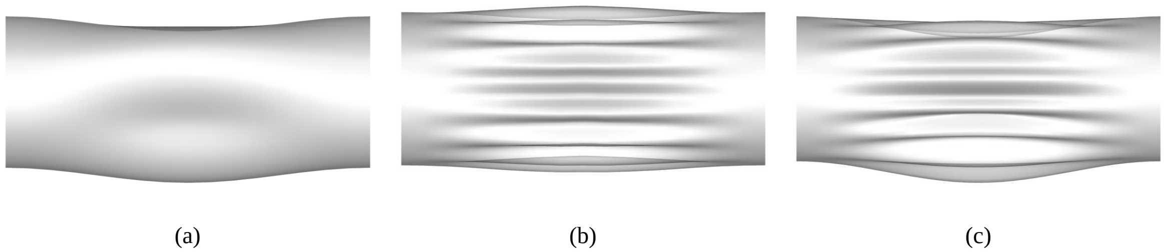

Figure 1.2: Side view of pipe-insert geometries in axial direction indicating (a) Case I, (b) Case II, and (c) Case III.

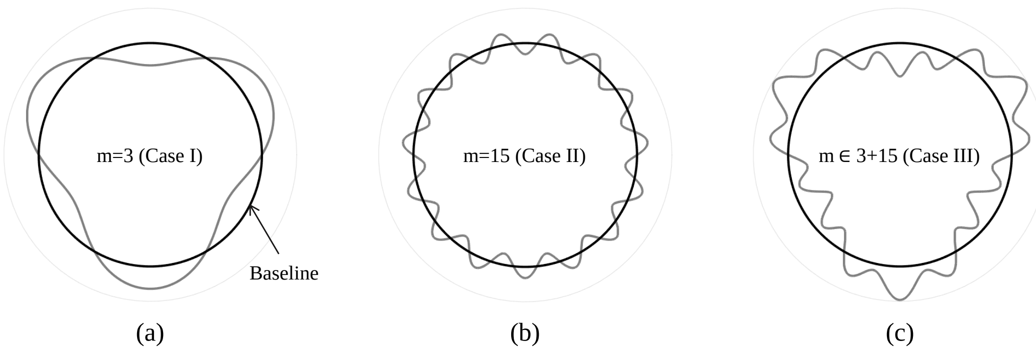

Figure 1.3: Schematics of the pipe-insert cross-sections representing (a) Case I, (b) Case II, and (c) Case III.

losses and transporting the stress concentrations away from the walls. Therefore, this can be used as a novel passive flow control technique with extensive operational benefits.

1.2 Pipe-Inserts

Pipe-inserts are three-dimensional (3D) sinusoidally varying wall geometries that were designed to target specific azimuthal Fourier modes (see Figure 1.2). In particular, three distinct azimuthal Fourier modes were targeted, corresponding to $m = 3$ (Case I), $m = 15$ (Case II), and $m \in 3+15$ (Case III). The purpose of introducing these pipe-inserts was to directly manipulate secondary flows (Prandtl, 1953; Perkins, 1970; Anderson et al., 2015) that are induced by spanwise gradients of Reynolds stresses (Van Buren et al., 2017). Gessner (1973), experimentally investigated the mean flow vorticity balance along a corner bisector and suggested that gradient of Reynolds stresses direct the flow towards the corner in the diagonal direction. Also, Einstein and Li (1958) implied that gradients of Reynolds stresses acting as the production terms of the streamwise vorticity, can induce the formation of secondary flow.

In addition, a handful of studies, e.g., Bailey and Smits (2010); Baltzer et al. (2013); Hellström and Smits (2014); Hellström et al. (2016); Van Buren et al. (2017) revealed that the azimuthal Fourier mode corresponding to $m = 3$, which was identified by 3 pairs of azimuthal structures (low/high momentum) contained the highest magnitude of turbulence kinetic energy (k). The self-similarity was further identified for another few azimuthal Fourier modes (i.e., $m \in [5, 15, 32]$) which hinted at the possibility of introducing a novel passive flow control strategy by targeting specific modes. These perturbations were introduced in the main domain, whose geometries were created based on the experiments of Van Buren et al. (2017). A schematic of the maximum variation in cross-sectional shape is presented in Figure 1.3.

The perturbation amplitude (a_m) advanced smoothly as a cosine wave in streamwise (axial) direction, where the average displacement angle of the wall with respect to the axial location was 2.8° and 1.4° for Case I and Case II, respectively, following the experiments of (Van Buren et al., 2017). The cross-sectional corrugation was outlined based on the following formulation in radial direction:

$$r(\theta, m, x) = \frac{D}{4}\left[2 + \left(\cos(\frac{\pi x}{2D}) + 1\right)\sum_{m} a_m sin(m\theta)\right]. \tag{1.1}$$

Here, r indicates the radial distance as a function of the azimuthal angle ($0 \leq \theta \leq 2\pi$), Fourier mode number (m), and the axial location ($-2D \leq x \leq 2D$). The total length of the pipe-inserts was $4D$, where $D = 2R$ represents the pipe diameter and R is the pipe radius. The amplitude of the perturbation was $a_m = 0.2$ for Case I, $a_m = 0.1$ for Case II, and $a_m \in \{0.2, 0.1\}$ for Case III, with Case III being the superposition of Case I and Case

II. The maximum perturbation height (h) was $0.1D$, $0.05D$, and $0.15D$ for Case I, Case II, and Case III, respectively. The change in cross-sectional area of the pipe-inserts was based on the following formulation (Van Buren et al., 2017):

$$\Delta A = \frac{1}{2}\sum_{m}(\frac{2a_m}{D})^2, \tag{1.2}$$

with a maximum change of 2% for Case I, 0.5% for Case II, and 2.5% for Case III.

1.3 Tools

Initially, a three-dimensional CAD model of the pipe-insert was developed for each case. The fluid domain, or pipe system, was meshed using ANSYS ICEM, as one of the most potent and well-known mesh generation tools, by means of three-dimensional hexahedral grids. The simulations were conducted using the *Open-source Field Operation And Manipulation* (OpenFOAM) as the main solver, which is formulated based on the finite volume method. "Foam" was primarily introduced by Henry Weller in 1989, where the libraries and software were designed based on C++ language for CFD simulations. Later in 2004, it was first released as an open-source finite volume software for CFD under the name of "OpenFoam", including various libraries, solvers, and pre$-$ and post$-$processing tools. A series of approaches were performed to determine the best performing solver, in which the Standard $k-\varepsilon$ turbulence model was nominated for modeling the turbulence effects in the flow, details of which are presented in Chapter 3. In terms of the turbulence modeling, detailed formulations for the Standard $k-\varepsilon$ model are provided in Chapter 2. The data obtained from simulations were then extracted and processed using a combination of Paraview, Tecplot, and MATLAB.

1.4 Motivation

Although the flow past large-scale wall-mounted obstacles ($h/\delta \gg 1$) has been studied extensively over the past few decades (Schofield and Logan, 1990; Martinuzzi and Havel, 2000; Farhadi and Rahnama, 2006; Doolan and Moreau, 2016; Yin et al., 2020), the recovery of the perturbed flow past small-scale ($h/\delta \ll 1$) wall-changes towards the equilibrium conditions of the new surface following such a transition is far from understood, to date. This includes studies on the dynamics of separated flows (Bradshaw and Wong, 1972; Kim et al., 1980; Kiya and Sasaki, 1983; Dimaczek et al., 1989; Jovic and Driver, 1995; Mollicone et al., 2017), and boundary layers (Smits et al., 1979; Hoffmann et al., 1985; Simpson, 1989). However, the investigation of flow response and recovery over small-scale uniquely curved walls at a range of Reynolds number remains unexplored. Here, numerical simulations are used to provide physical insights into the flow dynamics and recovery behavior. These insights address the existing knowledge gap in explaining how different targeted wall-shapes dictate the flow response and recovery through the development and interaction of different flow structures in the downstream wake.

This study was industrially motivated by technology developments to reduce greenhouse gas emissions in extraction, processing, and transportation of energy and other bi-products. Particularly, this study combines fundamental analysis of flow dynamics in pipes, wall-bounded turbulent boundary layers, and wakes to introduce a new concept for pipe flow manipulation. The main objective for the energy industry, which is the main end-user of the final technology, is to reduce pressure losses (reduced pump energy requirement), increase axial flow rate (led to faster transportation of products), lower rates of erosion and corrosion, and minimize condensations or slur formation. These benefits will translate to lower emissions in transportation of energy and energy-products using pipelines. It also increases the safety of these systems, which is essential for the economic and environmental prosperity of Canada.

1.5 Research Objectives

The primary research objectives are to:

(1) characterize the dynamics of flow manipulation based on targeted wall shapes;

(2) determine and characterize the turbulence response and recovery behavior past targeted wall-shapes;

(3) investigate, thoroughly, disturbed flow properties due to the pipe-insert shapes, i.e., mean axial velocity, velocity and pressure gradients, Reynolds stresses, turbulence kinetic energy;

(4) evaluate the effect of Reynolds number on flow disturbance, response, and recovery, due to targeted wall-shapes.

To this effect, the current study focuses on turbulent flow past a 3D pipe-insert that follows three distinct azimuthal Fourier modes, $m = 3$, $m = 15$, and $m \in \{3 + 15\}$. The detailed mechanisms and differences for different pipe-insert geometries are compared based on azimuthal Fourier modes at a high Reynolds number of 1.58×10^5. This comparison provides insightful information on the flow dynamics at three different targeted wall-shapes. Moreover, this study aims to detailed characterization of turbulent pipe flow disturbance, response, and recovery due to targeted perturbations, in the form of curved walls, at a wide range of Reynolds numbers ($5 \times 10^3 - 1.58 \times 10^5$). This includes developments of scaling laws for the effect of Reynolds number on recovery length, maximum stresses, and the response of the mean flow.

1.6 Novelty

The present work concentrates on addressing a knowledge gap on the response and recovery of pipe flow perturbed by wall-mounted obstacles. It is the first of its kind to characterize the effect of Reynolds number on the immediate flow response in the wake and the flow recovery in both near and far downstream regions. Another unique novelty of this research relates to the characterization of the wake structures, flow response, and flow recovery at high Reynolds numbers, based on the alternation of Fourier modes upon which the geometry was created. The detailed mechanisms and flow dynamics identified and characterized here, e.g., a non-monotonic second-order response characteristic along with a delayed recovery trend was observed for cases with higher Fourier mode wall-shapes, constitute a novel finding that advances the frontier of pipe flow dynamics and turbulent flow manipulation.

1.7 Structure of the Thesis

This thesis begins with a review of fundamental topics in fluid dynamics, a brief overview of flow modeling, and OpenFOAM as the principal platform employed to carry out the simulations. Further details on the state of the literature on the pipe flow dynamics are presented in the initial sections of Chapters 4 and 5. More specifically, these sections provide a comprehensive review of the existing literature on out-of-equilibrium flows past changes of the surface condition. The research methodology and numerical setup description, including grid quality, domain size analyses, and validation of numerical solvers, are outlined individually per study in Chapters 4 and 5. The latter chapter discusses turbulent pipe flow response to targeted wall shapes at a range of Reynolds numbers varying between $5 \times 10^3 - 1.58 \times 10^5$. This follows a thorough investigation of the implications of different targeted wall geometries on the response of turbulent pipe flow at high Reynolds numbers(1.58×10^5) in Chapter 4. Finally, the main conclusions and potential research topics for future developments are introduced in Chapter 6.

Chapter 2

BACKGROUND

This study employs computational fluid dynamics methods, tools, and techniques for a fundamental analysis of fluid flow in pipes with targeted wall shape variations. Thus, it is essential to discuss, in brief, an overview of fundamental topics in fluid mechanics, computational fluid dynamics, and turbulence modeling within the scope of this work. This sets the state of literature for this dissertation.

As stated by Batchelor (2000), a "simple" fluid can be referred to as material in which the elements can displace significantly on account of applying a sensible force. The Collins dictionary defined "dynamics" as "*the scientific study of motion, energy, and forces.*" Thereby, the definition of the term "fluid dynamics" can be presented as the study of motions, energy, and forces performed on or applied by a fluid matter. In continuum mechanics, "stress" (σ) is a measure of the internal forces that neighboring particles of a continuous material exert on each other. Thus in orthogonal coordinates, i.e., Cartesian coordinate system, stress can also be expressed as the fraction of internal forces exerted by adjacent particles by the area on which forces are applied,

$$\sigma_{ij} = \frac{F_i}{A_j} \tag{2.1}$$

Here, σ_{ij}, F_i, and A_j represent the stress tensor, force vector, and the planar area, respectively. According to Batchelor (2000), "dynamic viscosity" (μ), which is a fluid property, can be described as the fraction of tangential stress by velocity gradient:

$$\mu = \frac{\sigma_{ij}}{(\nabla_i u_j)} \tag{2.2}$$

The compressibility of a fluid matter is defined as the relative volume change on account of pressure variations (Babu, 2008). Although some fluids, such as water, are considered incompressible under natural atmospheric pressure conditions, all fluids are compressible to an extent. The exact definition of a fluid state has been classified and presented by aerodynamics experts, where the most prominent classifications were stated based on the fluid flow compressibility, viscosity, steadiness, and its randomness. Based on White and Corfield (2006), the *Reynolds number* (Re) is defined as a principal non-dimensional controlling criterion of a fluid state. Particularly, the Reynolds number determines the ratio of inertial to viscous forces, which resembles the dominant fundamental flow characteristics of the wake region. The formulation of Reynolds number is:

$$Re = \frac{\rho u c}{\mu} = \frac{uc}{\nu}, \tag{2.3}$$

in which u presents the velocity scale, c is the characteristic length scale, ρ is the density of fluid material, μ is the dynamic viscosity, and ν denotes the kinematic viscosity. As discussed earlier on definitions and classifications, the fluid's viscosity is of considerable importance in fluid dynamics. As a matter of fact, viscosity determines whether the fluid is viscous or inviscid. The tangential component of the latter is zero, and the stress tensor components are similar to that of arbitrary fluid at rest (Batchelor, 2000). A viscous fluid, however, experiences the presence of internal frictions because of the existence of velocity gradients between neighboring molecules (Batchelor, 2000). Another primary fluid parameter that characterizes the fluid flow is density (ρ). To this end, compressible flow is defined as a fluid motion with variable (inconstant) density, whereas incompressible flow consists of a fluid with a constant density. According to Anderson (2003), the incompressible flow assumption can be used for air flowing at a velocity up to 30% of the speed of sound. Moreover in wake dynamics, understanding the transient nature of the flow (that is, steady versus unsteady flow) is essential. In unsteady flows, the flow characteristics change over time, such that transient effects dominate the wake. Contrarily, flow properties associated with steady flows are not time-dependent, and their spatial variations dominate (Kuethe, 1976).

Turbulence is a complicated flow characteristic that arises at high Reynolds numbers due to propagation of perturbations and cascade of the energy associated with flow structures. Although there is not a simple definition for turbulence, the community described turbulent flows based on their particular features. These include (Davidson, 2017):

Irregularity: Turbulent flows are governed by the Navier-Stokes equations. However, they are irregular in nature and random in behavior, while exhibiting arbitrary characteristics.

Diffusivity: The momentum exchange increases between different flow layers in turbulent flow, which thereby amplifies the heat transfer and wall friction for internal flows. In addition, the diffusivity of turbulent flows is higher compared to laminar flows.

Three-dimensional: Turbulent flows are unsteady and three-dimensional in nature. However, time-averaged equations can be treated as two-dimensional for two-dimensional geometries.

Large Reynolds numbers: The transition to turbulent flow occurs with increasing Reynolds numbers due to larger fluctuations and propagation of perturbations in laminar flows. For example, transition to turbulent for pipe flows and boundary layers occur at $Re_D \simeq 2.3 \times 10^3$ and $Re_x \simeq 5 \times 10^5$, respectively.

Dissipation: The energy transport in turbulent flow follows a cascade, such that turbulence kinetic energy transfers from the largest scales to smaller scales in a cascade process. The flow is dissipative because of viscous force effects, which implies that the kinetic energy inherited in the small-scale eddies is dissipated as heat.

Continuum: The molecular-scale fluid particles are still significantly smaller than the smallest scales of a turbulent flow, and the flow is considered a continuum. Thus, turbulence is not regarded as a fluid characteristic, and it is rather a flow property. To this effect, the smallest scales in turbulent flows are characterized in terms of "*Kolmogorov Scales*". By definition, these scales are (Landahl et al., 1989):

$$\eta = (\frac{\nu^3}{\varepsilon})^{1/4} \quad , \quad \tau_\eta = (\frac{\nu}{\varepsilon})^{1/2}, \tag{2.4}$$

where, η is the length-scale, and τ_η represents the time-scale.

The continuity (conservation of mass), momentum, and energy equations are governing equations of a fluid motion that can be modified according to the state of the flow. In the current work, the pipe flow is considered to be viscous, incompressible, steady, and turbulent in Cartesian coordinate (x, y, z). We assumed that ensemble averages are steady in time, i.e., $\partial\overline{(\varphi)}/\partial t = 0$, where φ is any flow quantity. Therefore, the governing equations are (Durbin and Reif, 2011):

$$\partial_i \overline{U_i} = 0, \tag{2.5}$$

$$\overline{U_j}\partial_j\overline{U_i} = -\frac{1}{\rho}\partial_i P + \nu\nabla^2\overline{U_i} - \partial_j\overline{u_j u_i}. \tag{2.6}$$

2.1 Computational Fluid Dynamics (CFD)

The computational fluid dynamics method was first developed and introduced in the early 1930s to solve the linearized potential equations (Milne-Thomson, 1973). The advancement of technology motivated extensive research on this topic, and development of new techniques and schemes, over the past several decades. Here, the governing equations of fluid motion (e.g., Navier-Stokes and continuity equations) are solved numerically using different setups, including flow conditions, initializations, and boundary conditions (Versteeg and Malalasekera, 2007). Moreover, the accuracy and precision of numerical simulations are dependent on numerous parameters, e.g., the range of Reynolds number, boundary conditions, geometry scales, and non-linear interactions within the flow. Therefore, accurate numerical simulation of the flow characteristics in the wake of pipe flows with wall-mounted obstacles is challenging due to the complex flow behavior. The Finite Volume Method (FVM) is used in CFD codes in which the system of equations are solved by discretization of the domain into multiple control volumes or mesh elements. The FVM method has advantages over other methods in calculating high Reynolds number turbulent flows, such as reduced computational memory requirements and faster calculations. Different commercial and open-source CFD toolboxes are available that employ the FVM method. For example, ANSYS CFX, ANSYS Fluent, and STAR-CCM+ are robust commercial CFD packages. The prominent open-source CFD packages are OpenFOAM, SU2 code, and Fire Dynamics Simulator (FDS). In the current study, OpenFOAM is employed as the main platform for simulating the problem. A review of the CFD simulation setup manipulated in this dissertation is provided in Chapters 4 and 5.

2.2 Turbulence Modeling

Accurate prediction and modeling of the flow is very critical in numerical simulations, particularly when the geometry has a complex shape or the flow is at a high Reynolds number.

The performance of different RANS models, i.e., Standard $k-\varepsilon$, Realizable $k-\varepsilon$ and SST $k-\omega$, in capturing the main flow features in a pipe flow with targeted wall-shapes was investigated at the early stages of the research to identify the best tool for the numerical simulations. The results provided in Chapter 3 motivated focusing on using the Standard $k-\varepsilon$ turbulence model for extensive study of the pipe flow problem in Chapters 4 and 5. Detailed formulations for all these models are provided below, with a major emphasis on the Standard $k-\varepsilon$ model. Calculation of both time and length scales in turbulent flow at high Reynolds numbers requires a large amount of computational resources at higher costs. Therefore, RANS turbulence models were designed to reduce the computational costs while providing adequate prediction of the mean flow field. In turbulent flows, any flow variable (i.e., φ) consists of mean ($\overline{\varphi}$) and fluctuating components (φ'). RANS-based turbulence models utilize the mean flow variable ($\overline{\varphi}$) for calculations, as shown below (George, 2013):

$$\varphi(x_i,t) = \overline{\varphi}(x_i,t) + \varphi'(x_i,t), \tag{2.7}$$

$$\overline{\varphi}(x) = \lim_{T\to\infty} \frac{1}{T}\sum_{i=1}^{T} \varphi_i(x,t). \tag{2.8}$$

Here, T indicates the averaging interval. Averaging of the governing equations following the incorporation of the Reynolds decomposition returns (Durbin and Reif, 2011):

$$\partial_i \overline{U_i} = 0, \tag{2.9}$$

$$\overline{U_j}\partial_j \overline{U_i} = -\frac{1}{\rho}\partial_i P + \nu\nabla^2 \overline{U_i} - \partial_j \overline{u_j u_i}. \tag{2.10}$$

These are referred to as the RANS equations, in which the right-hand side consists of three terms, the mean pressure, viscous stresses, and the Reynolds shear stresses (averaged effect of turbulent convection). These formulations hint at the "closure problem" in turbulence. RANS solvers utilize a combination of eddy viscosity approximation and Boussinesq approximation to "close" the formulations through modeling of the Reynolds stress tensor, i.e., $-\overline{u_i u_j} \approx \nu_T[\partial_j \overline{U_i} + \partial_i \overline{U_j}]$. However, modeling of stress tensor differs between turbulence models, which can provide specific features for one versus the other, e.g., enhanced near-wall predictions. The transport equation and initial conditions of the four common turbulence models, including Standard $k-\varepsilon$, Realizable $k-\varepsilon$, $k-\omega$, and Shear Stress Transport (SST) $k-\omega$, are presented below based on OpenCFD (2019).

2.2.1 Initial Conditions

As shown by Vold (2017), the turbulence kinetic energy (k) term for an isotropic turbulent flow can be evaluated using:

$$k = \frac{3}{2}(I\, U_\infty)^2, \tag{2.11}$$

where I indicates the turbulence intensity, and U_∞ presents the inlet bulk velocity (for the pipe flow case). Similarly, the rate of turbulence dissipation (ε) can be estimated by:

$$\varepsilon = {C_\mu}^{\frac{3}{4}} \frac{k^{\frac{3}{2}}}{l}, \tag{2.12}$$

where $C_\mu = 0.09$ indicates a model constant, and $l = 0.038D$ shows the turbulent flow length-scale and stands for the hydraulic diameter of the pipe (Greenshields, 2015; Pope, 2001). Lastly, the turbulence specific dissipation rate (ω) formulation is as follows:

$$\omega = {C_\mu}^{\frac{-1}{4}} \frac{k^{\frac{1}{2}}}{l}. \tag{2.13}$$

2.2.2 Standard $k-\varepsilon$ Model

This is the most prominent simulation model for engineering applications. As it appears on its title, Standard $k-\varepsilon$ model utilizes the conservation equation for k and ε. According to Joshi and Nayak (2019), the turbulence kinetic energy (k) equation of Standard $k-\varepsilon$ turbulence model is presented as:

$$\partial_j(k\overline{U_j}) = \partial_j \left[(\nu + \frac{\nu_T}{\sigma_k})\partial_j k\right] + p_k - \varepsilon, \tag{2.14}$$

where P_k indicates the turbulent production by the interaction of mean velocity gradients and Reynolds stresses. And the turbulence dissipation rate (ε) is estimated using:

$$\partial_j(\varepsilon\overline{U_j}) = \partial_j \left[(\nu + \frac{\nu_T}{\sigma_\varepsilon})\partial_j \varepsilon\right] + \frac{C_1\varepsilon}{k}p_\varepsilon + \frac{C_2}{k}\varepsilon^2, \tag{2.15}$$

where $\nu_T = C_\mu k^2/\varepsilon$ is the eddy viscosity, P_ε represents ε production by the gradients of fluctuating velocity. C_1, C_2, σ_k, and σ_ε are presenting the model closure coefficients. The coefficient values are as follows:

$$C_1 = 1.44;\ C_2 = 1.92;\ \sigma_k = 1.00;\ \sigma_\varepsilon = 1.30. \tag{2.16}$$

2.2.3 Realizable $k-\varepsilon$ Model

The Realizable $k-\varepsilon$ turbulence model has an additional feature in which a damping function is used in the near-wall regions. This causes the turbulence to damp faster than the Standard $k-\varepsilon$ model in the near-wall area (Joshi and Nayak, 2019). In Realizable $k-\varepsilon$ turbulence model, the transport equation for k is similar to 2.14 and 2.15. However, the equation for ε changes to:

$$\partial_j(\varepsilon\overline{U_j}) = \partial_j\left[(\nu + \frac{\nu_T}{\sigma_\varepsilon})\partial_j\varepsilon\right] + \frac{C_1\varepsilon}{k}p_\varepsilon - \frac{C_2}{k+\sqrt{\nu\varepsilon}}\varepsilon^2, \tag{2.17}$$

where model constants are (Joshi and Nayak, 2019):

$$C_1 = 0.43;\ C_2 = 1.92. \tag{2.18}$$

2.2.4 Standard $k - \omega$ Model

Similar to the $k - \varepsilon$ turbulence model, the first transport variable is k, and the difference belongs to the second transport variable, that is ω (specific dissipation rate). This model is one of the conventional turbulence models that was first used by Kolmogorov (1941), and further developed and improved by Saffman (1970) and Saffman and Wilcox (1974), who demonstrated its accuracy for a wide range of turbulent flow applications. The turbulence kinetic energy transport and the turbulence specific dissipation rate (ω) equations are:

$$\partial_j(k\overline{U_j}) = \partial_j\left[(\nu + \frac{\nu_T}{\sigma_k})\partial_j k\right] + p_k - C_2k\omega, \tag{2.19}$$

$$\partial_j(\omega\overline{U_j}) = \partial_j\left[(\nu + \frac{\nu_T}{\sigma_\omega})\partial_j\omega\right] + \frac{C_1\omega}{k}p_\omega - C_2\omega^2. \tag{2.20}$$

Here, $\nu_T = k/\omega$, and closure coefficients are as follows (Joshi and Nayak, 2019):

$$C_1 = 0.56;\ C_2 = 0.075;\ C_\mu = 0.09;\ \sigma_k = 0.5;\ \sigma_\varepsilon = 0.5. \tag{2.21}$$

2.2.5 Shear Stress Transport $k-\omega$ Model

Menter (1993) Introduced the Shear Stress Transport $k-\omega$ model, in which the $k-\omega$ model is used to resolve the near-wall region, and $k-\varepsilon$ model is utilized for the remaining flow domain. In addition, SST $k-\omega$ model calculates Reynolds stresses and turbulence kinetic energy based on Standard $k-\omega$ model, and a modified dissipation rate of $\omega = \varepsilon/k$ based on Standard $k-\varepsilon$ model. Therefore, the equations for k and ω are (Joshi and Nayak, 2019):

$$\partial_j(k\overline{U_j}) = \partial_j\left[(\nu + \frac{\nu_T}{\sigma_k})\partial_j k\right] + p_k - C_1 k\omega, \tag{2.22}$$

$$\partial_j(\omega\overline{U_j}) = \partial_j\left[(\nu + \frac{\nu_T}{\sigma_\omega})\partial_j \omega\right] + \alpha S^2 - \beta\omega^2 + 2(1-F_1)\sigma_{\omega 2}\frac{1}{\omega}\partial_i k \partial_i \omega. \tag{2.23}$$

Here, the closure model coefficients are given as:

$$\begin{gathered}\alpha_1 = 0.31;\ S = \sqrt{2S_{ij}S_{ij}};\ \sigma_k = 0.85;\ \sigma_\omega = 0.50;\ \sigma_{\omega 2} = 0.856;\ \gamma_2 = 0.44 \\ \beta^* = 0.09;\ \beta_1 = 0.075;\ \beta_2 = 0.083.\end{gathered} \tag{2.24}$$

Chapter 3

MEAN PIPE FLOW SCALING & RANS MODELING

3.1 Introduction

The accuracy in the numerical modeling of pipe flows with small-scale wall-mounted obstacles is of considerable importance, especially at high Reynolds numbers. The Standard $k - \varepsilon$ turbulence model has been extensively used in industrial applications, where the flow separation and reattachment over curved surfaces are common. This is the most widely used and validated turbulence model. It has the capability to capture the mean flow physics of complex geometries cost-effectively (Haroutunian and Engelman, 1991; Launder and Spalding, 1983). This chapter provides a brief study on the performance of different RANS-based turbulence models to identify the best tool for simulating turbulent pipe flow response and recovery past targeted walls at moderate and high Reynolds numbers. This chapter is structured in such a way that a brief background is provided in Section 3.2. A description of the numerical setup is presented in Section 3.3 and followed by assessing the performance of various RANS models in Section 3.4 and the mean flow scaling in Section 3.5.

3.2 Background

Numerical simulations have been widely used in industrial applications to examine pipe flow in the presence of various obstacles and disturbances at moderate and high Reynolds numbers (Shah et al., 2012; Yamagata et al., 2014). Pipe flow past sudden wall changes including roughness elements and orifice are studied at low and moderate Reynolds numbers ($Re \leq 10^4$) using Direct Numerical Simulation (DNS) and Large Eddy Simulation (LES), e.g., Leonardi and Castro (2010), Leonardi et al. (2003), Nygård and Andersson (2013), Cui et al. (2003), and Chang and Scotti (2004). High Reynolds number cases (i.e. $10^4 - 10^6$) are simulated using Reynolds−Averaged−Navier−Stokes (RANS) models, e.g., Goswami and Hemmati (2020, 2021) and Cappelli and Mansour (2013). Despite some differences between numerical results obtained using different turbulence models (Hemmati et al., 2018), these techniques have proven reliable in capturing the main flow (bulk flow) features. Although DNS studies are limited to $Re \leq 10^4$, the lower computational cost of RANS models over LES and DNS, and reasonable engineering accuracy, increased the Reynolds number range (i.e., $10^4 - 10^6$) that is considered in these studies. For example, Cappelli and Mansour (2013) studied the flow over a wall-mounted hump using the Standard $k - \varepsilon$, $k - \omega$, Shear Stress Transport (SST) $k - \omega$ and Spalart-Allmaras models in OpenFOAM at $Re = 9.3 \times 10^5$. Comparing their results with experiments of Rumsey et al. (2004) illustrated that the Standard $k - \varepsilon$ turbulence model performed better in determining the Reynolds shear stresses and pressure coefficients compared to the other RANS models. Similarly, Fogaing et al. (2019) simulated the highly unsteady wake of a sharp-edge normal flat plate using the Standard $k-\varepsilon$, Reynolds Normalization Group (RNG) $k - \varepsilon$, $k - \omega$ and SST $k - \omega$ models at $Re = 1.2 \times 10^3$. The comparison of their results with DNS of the same wake (Hemmati, 2016) reiterated the conclusion of Cappelli and Mansour (2013) on the better relative performance of the Standard $k - \varepsilon$ model in the presence of large pressure gradients. More recently, Goswami and Hemmati (2020, 2021) analyzed the flow over square bar roughness in a turbulent pipe flow at $Re = 1.56 \times 10^5$ and compared their results with experiments of Smits et al. (2019).

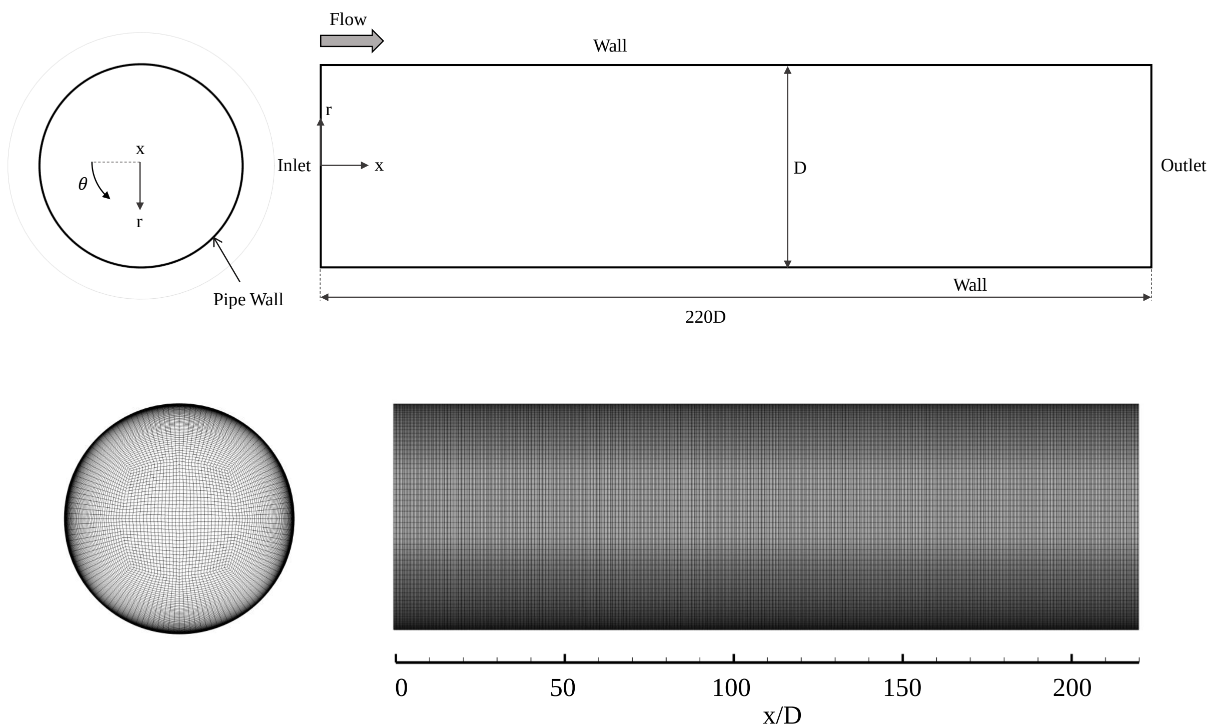

Figure 3.1: Schematic of the primary computational domain utilized in this study (not to scale) is shown in the first row, and the mesh distribution is shown in the second row (scales are different in radial and axial directions).

Once again, they observed that the Standard $k-\varepsilon$ model performed better than other turbulence models at high Reynolds numbers. However, these studies all corresponded to cases with large streamline curvatures, such as abrupt changes in the wall-shape through square elements or thin flat plates. The reasonable agreement of numerical and experimental results suggested that Standard $k-\varepsilon$ RANS model is a suitable model with capability of predicting the main flow parameters, while capturing the recovery and response of pipe flow to small modifications to the wall and abrupt flow disturbances. Here, we provide a comparative evaluation of the performance of various RANS-based turbulence models in simulating turbulent pipe flow response and recovery with smooth variations in wall-shape (targeted walls).

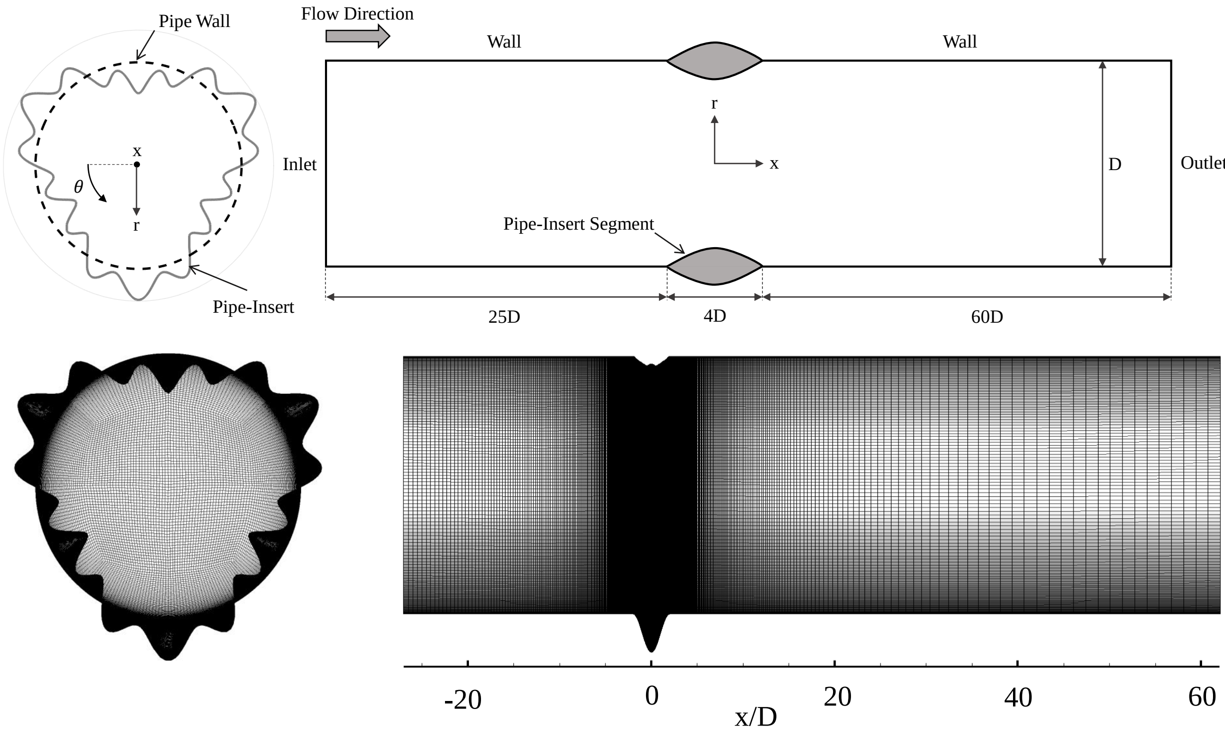

Figure 3.2: (Schematic of the main computational domain manipulated in the current study (not to scale) shown in the first row. The distribution of spatial grid over the cross-sectional area and axial direction (scales are different in radial and streamwise directions) is provided in second row.

3.3 Simulation Setup

The computational domain was designed to follow the experimental setup of Van Buren et al. (2017). In order to reduce computational costs, the three-dimensional domain was designed in two segments. The first part includes a long smooth pipe with an overall length of $220D$ that enabled the flow to achieve fully-developed conditions at the outlet boundary (see Figure 3.1). In the second part, the designated perturbation was introduced by placing a pipe-insert, the geometry of which was designed based on Case III introduced in Chapter 1.2. The schematic of the main domain is presented in Figure 3.2. The $89D$ domain length was extended from $-27D$ to $+62D$ in the streamwise or axial ($x-$) direction. The perturbation amplitude (a_m) followed a sinusoidal curve in the streamwise direction, and the wall shape in the radial direction was changed based on the variation of axial location (x), Fourier mode number (m), and azimuthal angle of θ, where the formulation was:

$$r(\theta, m, x) = \frac{D}{2}\left[1 + \frac{cos(\frac{\pi x}{2D}) + 1}{2}\sum_{m} a_m sin(m\theta)\right], \tag{3.1}$$

where $x \in [-2D, 2D]$, $\theta \in [0, 2\pi]$, $m \in (3 + 15)$, and $a_m \in \{0.2, 0.1\}$. The Reynolds number based on the bulk flow ($Re = U_\infty D/\nu$) changed between 2×10^4 and 1.58×10^5, where U_∞ indicates the bulk velocity introduced at the inlet of the $220D$ smooth pipe case, D is pipe diameter, and ν is the fluid kinematic viscosity.

A non-homogeneous $3D$ structured mesh was designed for both domains, with a total number of 6.8×10^6 and 1.22×10^7 hexahedral elements for the $220D$ domain and Case III (main domain), respectively. For the main domain, the more refined grid was placed in the vicinity of the pipe-insert section, where the grid size increased towards inlet and outlet boundaries with an expansion ratio of 1.02. The fully-developed inflow condition (Dirichlet and Neumann boundary conditions for velocity and pressure fields, respectively) was applied at the inlet boundary, which was mapped from the outlet boundary of the smooth pipe case. However, at the outlet boundary, a Neumann boundary condition was implemented for both velocity and pressure fields. In addition, a no-slip boundary condition was applied at walls, along with a standard wall-function (Liu, 2016). The friction Reynolds number was defined as $Re_\tau = u_\tau D/\nu$, where the friction velocity (u_τ) was obtained based on McKeon et al. (2004) correlations. Six Reynolds number cases were investigated: $Re = 1.58 \times 10^5$ ($Re_\tau = 7144$), 7.5×10^4 (3635), 5.0×10^4 (2525), 4.0×10^4 (2053), 2.5×10^4 (1399), and 2.0×10^4 (1149). Three turbulence models, e.g., Standard $k - \varepsilon$, Realizable $k - \varepsilon$ and SST $k - \omega$, were used in OpenFoam (Versteeg and Malalasekera, 2007) to carry out the simulations. The second-order accurate discretization schemes were implemented for both advection and diffusion terms of the RANS equations, with a convergence criterion of root-mean-square (rms) of momentum residuals of lower than 10^{-5}. A steady-state solver based

Table 3.1: Grid distribution information based on Case III. Δx^+ and $\Delta\theta^+$ resemble the grid spacing in the axial and azimuthal directions in wall units based on inflow parameters, respectively.

Study	First Cell (r^+)	$\Delta\theta^+$	Δx^+	Number of Cells
Grid 1	16	110	98	6.70×10^6
Grid 2	4	95	165	8.95×10^6
Grid 3	4	95	127	10.37×10^6
Grid 4	4	95	98	12.20×10^6
Grid 5	2	94	98	14.49×10^6

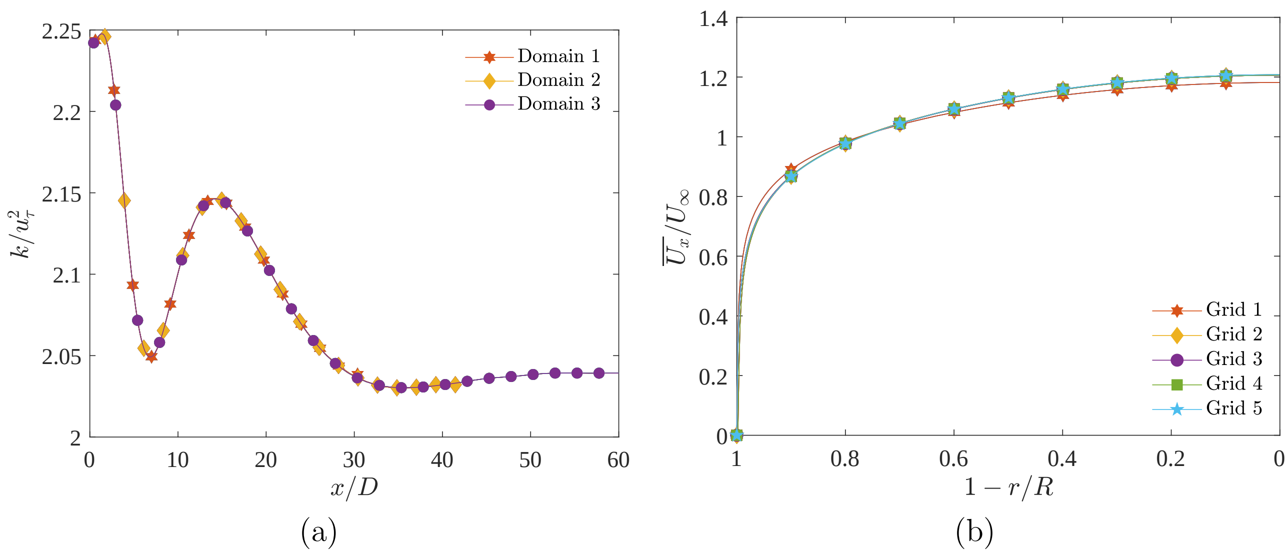

Figure 3.3: Effects of (a) domain length and (b) grid distribution on main flow features.

on *Semi-Implicit-Pressure-Linked-Equation* (SIMPLE) (Greenshields, 2015) algorithm was employed to complete the simulations. The results were normalized using the upstream friction velocity (u_τ) and bulk velocity (U_∞) at the inlet of the smooth pipe.

The simulations were verified at the initial stage, where the domain and grid sensitivity was examined comprehensively on the main domain with the aid of Standard $k-\varepsilon$ model. Three cases with an axial domain length of $59D$ (Domain 1), $69D$ (Domain 2), and $89D$ (Domain 3) were investigated. The outlet boundary was adjusted in such a way that it provides sufficient axial extent for accurate calculation of mean and turbulent fields (i.e., axial velocity and turbulence kinetic energy) along the pipe centerline. As shown in Figure 3.3(a), Domain 3 exhibited an adequate axial extent to accurately predict perturbed turbulent pipe

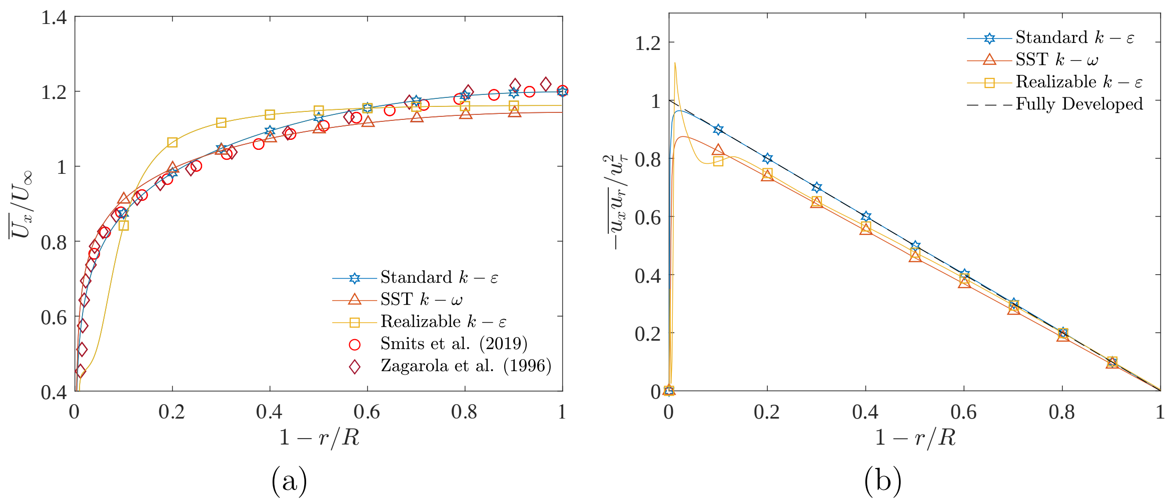

Figure 3.4: (a) Mean axial velocity, and (b) Reynolds shear stress distribution obtained using various turbulence models at $Re = 1.58 \times 10^5$.

flow characteristics in the downstream wake and therefore manipulated for further simulations. In addition, the grid sensitivity analysis was conducted by consecutive refinement of the hexahedral mesh distribution in all three directions and using five grids (see Table 3.1 for grid details). The results presented in Figure 3.3(b) indicated a difference of less than 3% among the mean velocity and Reynolds stress profiles of Grid 4 and 5. This provides us the confidence that Grid 4 can adequately capture the main flow properties. More details on the grid sensitivity and domain analysis are provided in Chapters 4 and 5.

3.4 Performance of RANS Models

The initial analysis was a validation study that involved comparing the flow predictions from different turbulence models in a pipe compared to experiments of Smits et al. (2019) at a high Reynolds number of $Re = 1.58 \times 10^5$. Turbulence models considered in this study included: Standard $k - \varepsilon$, Realizable $k - \varepsilon$ and SST $k - \omega$, whose performance in predicting the main flow features were examined relative to experiments.

Figure 3.4 shows the simulation results for a fully-developed state of a long smooth pipe with an overall length of $220D$. Figure 3.4(a) compares the mean axial velocity profiles from different models to the experiments of Smits et al. (2019) and Zagarola et al. (1996). Here, the Standard $k-\varepsilon$ turbulence model had a better agreement with experiments in comparison with other turbulence models considered here, for both core flow and regions close to the wall. The largest deviation of simulation results from experiments was less than 3%.

In addition to the mean flow parameter, the turbulence field was also examined. Specifically, the Reynolds shear stress profiles are presented in Figure 3.4(b), wherein the dashed-line indicate the "Fully Developed" profile based on the theoretical shear stress data given in Kaneda et al. (2003). Significant differences were identified for the Realizable $k-\varepsilon$ turbulence model, which failed to accurately capture Reynolds shear stresses close to the wall. The SST $k-\omega$ model, however, performed better compared to the Realizable $k-\varepsilon$ model, where a difference of $\approx 10\%$ was evident compared to the expected fully-developed value. Since Realizable $k-\varepsilon$ model employs a near-wall treatment, while SST $k-\omega$ model incorporates the enhanced near-wall treatment (Menter and Esch, 2001), the main reasoning behind such inaccuracies could be related to high Reynolds number effects. Such flow features are difficult to model numerically, as discussed previously by Hultmark et al. (2012). More information regarding the validation study at lower Reynolds numbers are provided in Chapter 5.

The performance of RANS models in capturing the pipeflow response to targeted wall-shapes and its subsequent recovery is compared in Figure 3.5. The results obtained using the Standard $k-\varepsilon$ and Reynolds Stress Models (RSM) at $Re = 10^4$ showed that the two models performed similarly in capturing the flow profiles, while the latter required substantially more computational power. The Standard $k-\varepsilon$ model case required 40 cores and 160 GB of RAM with an average simulation time of ≈ 96 hours to reach convergence within 7×10^3 iterations. The simulations based on RSM required 40 cores and 160 GB of RAM to reach convergence within 6×10^4 iterations at an average simulation time of ≈ 158 hours. The maximum variation between the Standard $k-\varepsilon$ and RSM results was less than 8% in velocity and stress profiles at $x/D = 60D$, which corresponds to a fully recovered state of the flow. However, contour of changes in the axial velocity due to the targeted wall-shapes

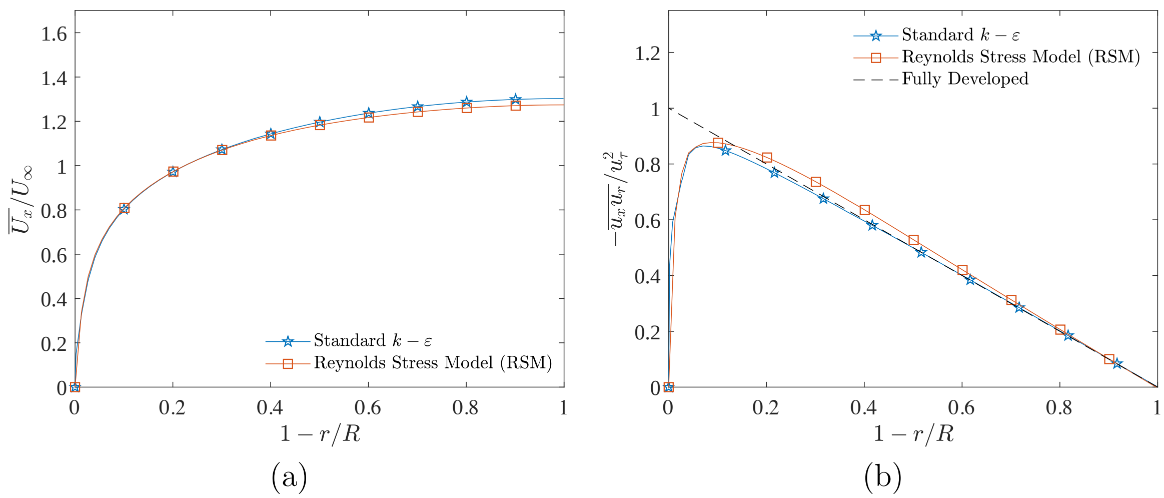

Figure 3.5: (a) Mean streamwise (or axial) velocity, and (b) the Reynolds shear stress profiles at $x/D = 60$ downstream of the pipe-insert for $Re = 1 \times 10^4$.

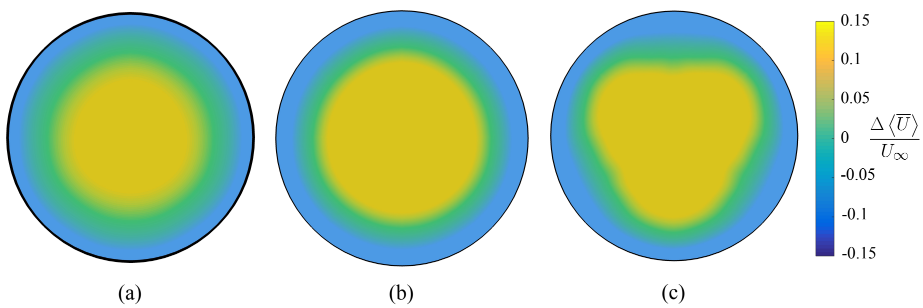

Figure 3.6: Comparing contours of axial velocity change relative to a smooth pipe at $x/D = 5$ downstream the pipe insert using the Standard $k-\varepsilon$ model at (a) $Re = 1.58 \times 10^5$ and (b) $Re = 1 \times 10^4$, compared to the results from (c) the Reynolds Stress Model results at $Re = 1 \times 10^4$.

shown in Figure 3.6 show inconsistencies of the RSM results compared to the Standard $k-\varepsilon$ model and experiments (*Figure 3c*) of Van Buren et al. (2017). The discrepancies observed in RSM results at even a low Reynolds number case correspond to the difficulties of this model in capturing main features of the flow accurately in the presence of smooth pipe wall-shape variations. This could potentially be due to the calculation of stresses near the wall. The Standard $k-\varepsilon$ model agreed well with the experiments (Van Buren et al., 2017) at high Reynolds numbers, while retaining the same trend at lower, post-transition, Reynolds number of 1×10^4.

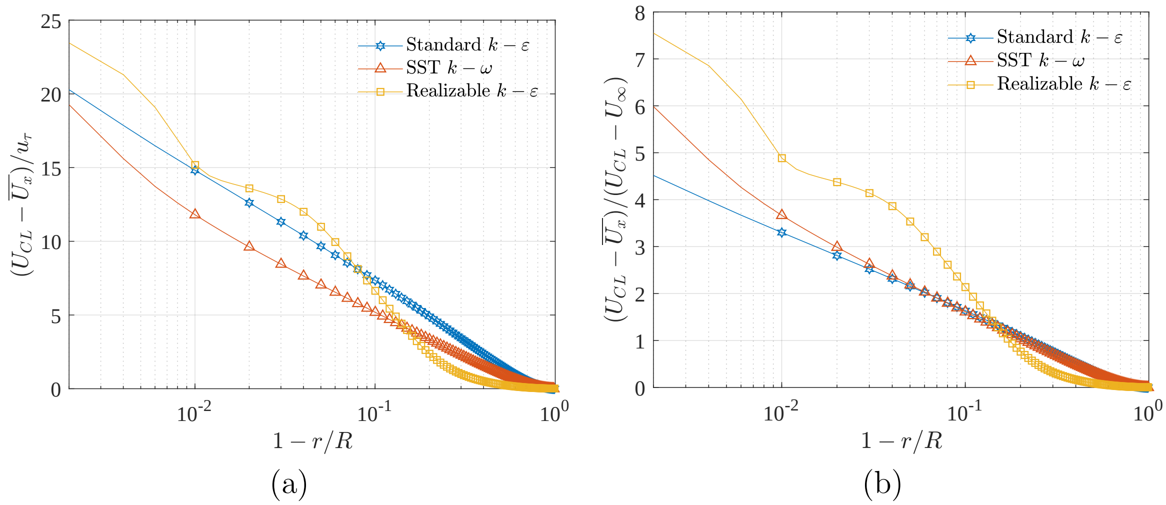

Figure 3.7: Mean axial velocity profiles of various turbulence models (a) Scaled with u_τ, (b) Scaled with $U_{CL} - U_\infty$ at $Re = 1.58 \times 10^5$.

3.5 Mean Flow Scaling

This study was further extended to analyze the performance of RANS models specifically for flows encountering smoothly varying perturbations. Particularly, the scaling of mean streamwise velocity was examined for fully-recovered state of the flow with different models. Zagarola and Smits (1998) introduced a velocity scale for the outer region of the flow, which is valid for $Re \geq 1.3 \times 10^4$, in the form of:

$$\frac{(U_{CL} - \overline{U_x})}{U_\eta} = g(r/R), \tag{3.2}$$

where U_η denotes the velocity scale for the outer region of the flow. In section 3.4, it was observed that Standard $k-\varepsilon$ and SST $k-\omega$ models exhibited a better performance than Realizable $k-\varepsilon$ model in capturing the mean flow field. As such, the proposed mean flow scaling was employed to examine how accurately turbulence models simulate the flow past perturbations at $Re = 1.58 \times 10^5$. The data were captured at $x/D = 60$. Figure 3.7 shows that both models agreed with using $(U_{CL} - U_\infty)$ for the scaling. However, results obtained from the Realizable $k-\varepsilon$ model showed discrepancies using both outer scaling methods.

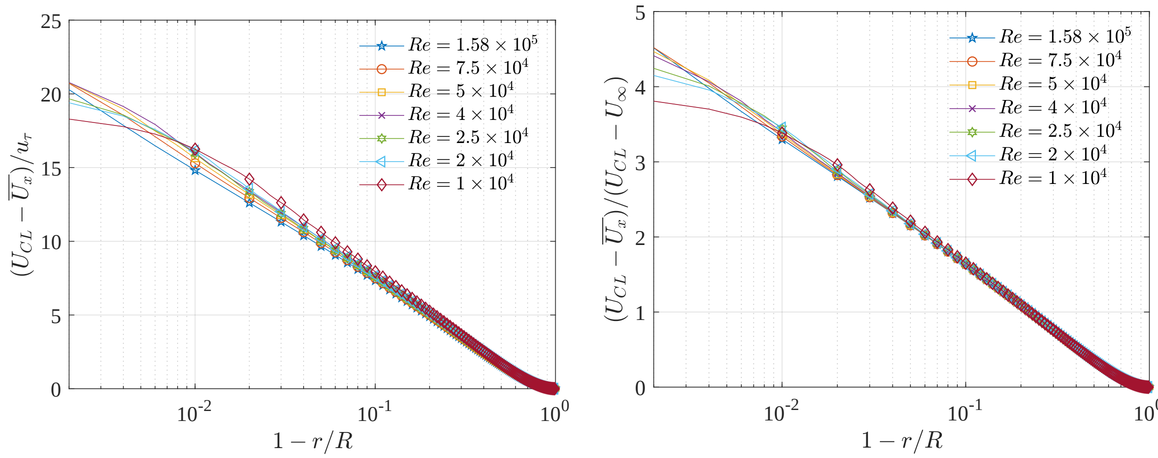

Figure 3.8: Mean flow scaling of Standard $k-\varepsilon$ turbulence model (a) Scaling with u_τ, (b) Scaling with $U_{CL}-U_\infty$.

Once the performance of different models was tested, and accuracy of the Standard $k-\varepsilon$ turbulence model was established, the analyses was extended to assess the validity of simulation data in following known scaling laws (Zagarola and Smits, 1998) that were developed with respect to Reynolds number. Figure 3.8 illustrated collapsing of the fully-developed mean velocity distribution at $x/D = 60$ at different Reynolds numbers: $1 \times 10^4 \leq Re \leq 1.58 \times 10^5$. Scaling the results with friction velocity (u_τ) did not lead to a reasonable collapse even in the outer region ($0.07 < 1 - r/R < 0.3$). However, the profiles collapsed well using ($U_{CL} - U_\infty$), especially at $(1 - r/R) > 0.03$. This was consistent with the findings of Zagarola and Smits (1998). The comparative assessment of velocity scales thus suggested that the velocity deficit ($U_{CL} - U_\infty$) was a better parameter to scale the results, compared to u_τ, in the recovered flow region far downstream of perturbation. The change in the velocity scale did not seem to affect the collapse of mean velocity profiles at the center of the pipe.

3.6 Summary

The good agreement between the Standard $k-\varepsilon$ results and experiments suggested that this approach is adequate in simulating pipeflow disturbance, response, and recovery of internal flows encountering smooth perturbations in the form of targeted wall shapes at moderate and high Reynolds numbers. The Standard $k - \varepsilon$ model can adequately predict the flow physics, despite unavoidable discrepancies (amounted to $\approx 3\% - 10\%$ in mean and turbulent flow fields) on account of inherent modeling errors. Normalizing the velocity profiles of the turbulent pipeflow past targeted wall shapes using the velocity deficit $(U_{CL} - U_{\infty})$ led to proper collapse of the mean axial velocity distribution in the outer flow region. This was found to give significantly better agreement between different Reynolds number cases, compared to the friction velocity (u_τ), and was also found consistent with the literature. Therefore, all simulations in the present research are computed using the Standard $k - \varepsilon$ formulations.

Chapter 4

EFFECTS OF TARGETED WALL SHAPES

4.1 Introduction

The implications of targeted wall-shapes on disturbance, response, and recovery of turbulent pipe flow is analyzed here using the Standard $k-\varepsilon$ model at the highest Reynolds number considered here, $Re = 1.58 \times 10^5$. Three different wall shapes were tests, as described previously in Section 1.2. The results and discussions provided in this chapter provide insightful details on characterization of the flow response and recovery due to the targeted perturbation introduced by the pipe-inserts. This chapter addresses the primary objectives (1), (2), and (3), as outlined in Section 1.5, by characterizing the pipe flow past targeted wall shapes. This chapter is set up, such that a brief background is provided in Section 4.2. The problem description along with details on the numerical setup are provided in Section 4.3, followed by verification and validation of the results in Section 5.4. Demonstration of the results and their discussion are provided in Section 4.5. A summary of the main conclusions for this chapter are outlined in Section 4.6.

4.2 Background

The response and recovery of wall-bounded turbulent flows have great importance in engineering applications, such as designing energy transportation pipelines, marine vehicles, and buildings. Wall-bounded turbulent flows at high Reynolds number (Re) with sudden changes in wall conditions represent a class of non-equilibrium flows that are not yet well-understood (Van Buren et al., 2019). These include flow over a step (Smits et al., 2019; Jiménez, 2004; Goswami and Hemmati, 2020, 2021), presence of surface curvature (Van Buren et al., 2017; Ding et al., 2019; Smits et al., 1979), and the change in surface roughness (Van Buren et al., 2019, 2020; Saito and Pullin, 2014). In the study of turbulent flow past rough walls, Jiménez (2004) indicated that small-size steps that act similar to isolated roughness elements can have a significant impact on drag, and induce changes in downstream flow features, i.e., noise production, surface pressure fluctuations, and structural vibration (Ji and Wang, 2010). Hence, the flow response and recovery past the perturbation inspired extended studies in this field. Modification of pipe wall geometry has considerable impacts on stabilizing (Muck et al., 1985) and destabilizing (Smits et al., 1979; Hoffmann et al., 1985) the flow turbulence, and the performance of passive flow control devices (Ding et al., 2019). Further, pipe flows with wall-mounted perturbations are extensively used in the energy industry and health sciences to characterize the flow field, e.g., orifice flow meters (Feng et al., 2020).

There are several numerical and experimental studies that investigated non-equilibrium wall-bounded turbulent flows. Antonia and Luxton (1971) experimentally examined the response of turbulent boundary layer past a surface roughness that transitions to a smooth wall. They found a deviation of mean velocity and Reynolds shear stress distributions from the self-preserving state in the far downstream region while observing a non-monotonic flow behavior. Later on, the effects of concave curvature on turbulent pipe flow were investigated by Smits et al. (1979). It was observed that an initial amplification of Reynolds stresses occurred that was followed by a turbulence collapse (in Reynolds stresses) in the outer layer to levels below the equilibrium state attained in the far downstream region (Smits et al., 1979). They attributed this second-order flow response to the interaction between mean shear and turbulent shear stress, which further led to long-lasting changes in turbulent flow properties. Also, studies that focused on turbulent boundary layers subjected to sudden perturbations, e.g., Smits and Wood (1985), observed slow adjustments of the flow to the new wall condition. However, pipe flow and boundary layer represented different responses in the outer regions of the flow since the pipe flow geometry restricted the large-scale motions (LSMs) in the core region (Chung et al., 2015). It should be noted that non-monotonic response was not specific to flows undergoing smooth-wall changes as was recognized in very recent studies (Van Buren et al., 2019, 2020). Durst and Wang (1989) numerically and experimentally investigated the effect of axisymmetric ring-type wall-mounted constriction in a fully-turbulent pipe flow over a range of Reynolds numbers. The overshoot of the flow response in the vicinity of the wall-mounted perturbation was observed, which eventually extended to the downstream region and was followed by a rapid decay in Reynolds stresses. The Standard $k-\varepsilon$ turbulence model further exhibited a good agreement with experimental data in terms of predicting flow characteristics. Dimaczek et al. (1989) also investigated the flow over two-dimensional planes and axisymmetric surface-mounted obstacles at moderately high Reynolds numbers ($5 \times 10^3 < Re < 5 \times 10^4$). The comparison of turbulent structures and their downstream development for two geometries highlighted the important role of upstream flow conditions in determining the flow reattachment length. Later on, Jiménez (2004) analyzed the influence of rough walls on turbulent flow and concluded that small steps (described as $h/\delta \ll 1$, where h is height of the step and δ is the boundary layer thickness), which behaved similar to the isolated roughness elements, could cause considerable change in the flow features, e.g., drag.

Hultmark et al. (2010) examined near-wall turbulence scaling in pipe flows over a wide range of Reynolds numbers ($2.4 \times 10^4 - 1.45 \times 10^5$). They identified a primary peak in turbulence intensity in the near-wall region. However, a weaker secondary peak in turbulence intensity also existed in the downstream wake, which was quite evident at high Reynolds numbers. This study was further expanded by Hultmark et al. (2012) and Hultmark et al. (2013), in which they observed a similar behavior in turbulence intensity that they identified as a prominent characteristic of high Re flows. Despite these studies, the case of turbulent pipe flows that undergo changes in wall shapes following specific azimuthal Fourier modes remains unexplored, particularly the investigation into their effects on flow response and recovery at high Reynolds numbers.

The most recent experimental studies of the response and recovery of flow past abrupt variations in wall conditions at high Reynolds numbers ($1.31 \times 10^5 - 1.56 \times 10^5$) includes Smits et al. (2019), Van Buren et al. (2019), and Van Buren et al. (2020). The first study quantified the response and recovery of the perturbed flow over axisymmetric square bar roughness elements and introduced a novel flow control method (Smits et al., 2019). The experiments were conducted using two bar heights of $0.05D$ and $0.1D$ at $Re = 1.56 \times 10^5$. They observed that perturbed flow was not fully recovered within $10D$ downstream of perturbation. A sudden contraction and expansion of the flow also occurred due to the presence of a square bar roughness element, which further induced an overshoot of flow response in the vicinity of the perturbation. Smits et al. (2019) also quantified the Reynolds shear stress recovery process. They proposed a power-law trend upon which the location of maximum Reynolds shear stress moved away from the wall toward the pipe centerline, and thus revealed the advantages of a passive flow control mechanism. Analysis of flow past the smaller bar roughness element indicated a prolonged recovery behavior that suggested an extended region of low skin friction past the bar roughness element. Smits et al. (2019) hinted at the feasibility of introducing abrupt changes in a wall-bounded flow in periodic patterns to obtain an extended region of lower turbulence levels, reduced drag, and lower surface friction. A second-order flow response was observed that indicated similarities to previous studies investigating turbulent pipe flow recovery after sudden changes in wall conditions (Smits et al., 2019). To obtain the evolution of a fully-equilibrium state, turbulence production should exceed dissipation in the near-wall region and the excess near-wall turbulence should then be transported away from the wall (Smits et al., 2019). Moreover, turbulence transport in the far downstream region appeared to be affected by the geometrical constraint of pipe flow, which was not the case for boundary-layer studies (Antonia and Luxton, 1971; Smits et al., 1979; Smits and Wood, 1985; Chung et al., 2015). More recently, Goswami and Hemmati (2020) observed that the long-lasting changes of the downstream wake resulted in a longer reattachment length compared to flows over backward-facing steps at a similar Re. The Reynolds shear stress experienced an amplification close to the bar roughness and represented a slow decay rate in the further downstream region, and therefore caused a slow and long-lasting recovery.

The response of turbulent pipe flow to a step-change in surface roughness was also analyzed by Van Buren et al. (2019, 2020). The overshoot of Reynolds stresses was observed with a peak at the location close to the step-change. The mean velocity and Reynolds shear stress distribution represented an oscillatory response and did not attain equilibrium within $60D$ downstream of the perturbation (D being the pipe diameter). They attributed this behavior to a second-order flow response that was previously identified in studies of flow past a concave curvature (Smits et al., 1979). Most recently, the response and recovery of fully-turbulent pipe flow across single (Goswami and Hemmati, 2021) and multiple (Goswami and Hemmati, 2020) small square bar roughness elements (two bar heights of $0.05D$ and $0.1D$) was examined by Goswami and Hemmati (2020, 2021) at Reynolds number of $Re = 5.00 \times 10^3 - 1.56 \times 10^5$. They also compared different Reynolds-Averaged-Navier-Stokes (RANS) turbulence models in predicting turbulent pipe flow response in the presence of small roughness elements. The Standard $k - \varepsilon$ model showed a reasonable agreement with experimental data (Smits et al., 2019), which implied that it could capture the main flow features accurately, and predict response and recovery of turbulent pipe flow effectively. These findings were in agreement with previous studies that examined the performance of turbulence models in simulating flow in pipes (Cappelli and Mansour, 2013) and wakes (Fogaing et al., 2019).

A handful of recent studies (Van Buren et al., 2017; Liu et al., 2019; Smits et al., 2019; Van Buren et al., 2020; Goswami and Hemmati, 2020, 2021) have highlighted the significant impact of upstream flow conditions in determining the overall flow response and recovery behavior, such as wall shape, perturbation height, and periodicity of wall-mounted impulses. However, there exists a knowledge gap on the effects of targeted pipe wall-shapes, based on particular Fourier modes, on response and recovery of the perturbed flow. In this chapter, we focus on the flow response and recovery by simulating a fully-turbulent pipe flow at $Re = 1.58 \times 10^5$ in the presence of wall shapes that target distinct azimuthal Fourier modes of $m = 3$, $m = 15$, and $m \in \{3 + 15\}$. This complements an earlier experimental study by Van Buren et al. (2017) at the same Reynolds number.

4.3 Problem Description

We numerically studied the response and recovery of fully-developed turbulent pipe flow past changes in wall shape following specific azimuthal Fourier modes in wall-bounded turbulence. The bulk flow Reynolds number ($Re = \rho U_\infty D/\mu$) was 1.58×10^5, such that ρ is the density, U_∞ represents the bulk axial velocity at the inlet of the smooth pipe, D is the pipe diameter, and μ is the fluid dynamic viscosity. The change in the pipe wall was introduced by placing a pipe-insert based on the study of Van Buren et al. (2017), while the flow behavior was assessed up to a distance of $60D$ past the perturbation. The perturbed inserts targeted three particular azimuthal Fourier modes corresponding to $m = 3$ for Case I, $m = 15$ for Case II, and superposition Fourier mode of $m \in \{3 + 15\}$ for Case III. The perturbation amplitude followed a sinusoidal variation in the axial direction, where the formulation for wall configuration was:

$$r(\theta, m, x) = \frac{D}{2}\left[1 + \frac{\cos(\frac{\pi x}{2D}) + 1}{2} \sum_m a_m \sin(m\theta)\right]. \tag{4.1}$$

Here, m represents the Fourier mode, $\theta \in [0, 2\pi]$ denotes the azimuthal angle, and $x \in [-2D, 2D]$ is the axial (streamwise) location. Perturbation amplitude was $a_m = 0.2$ for

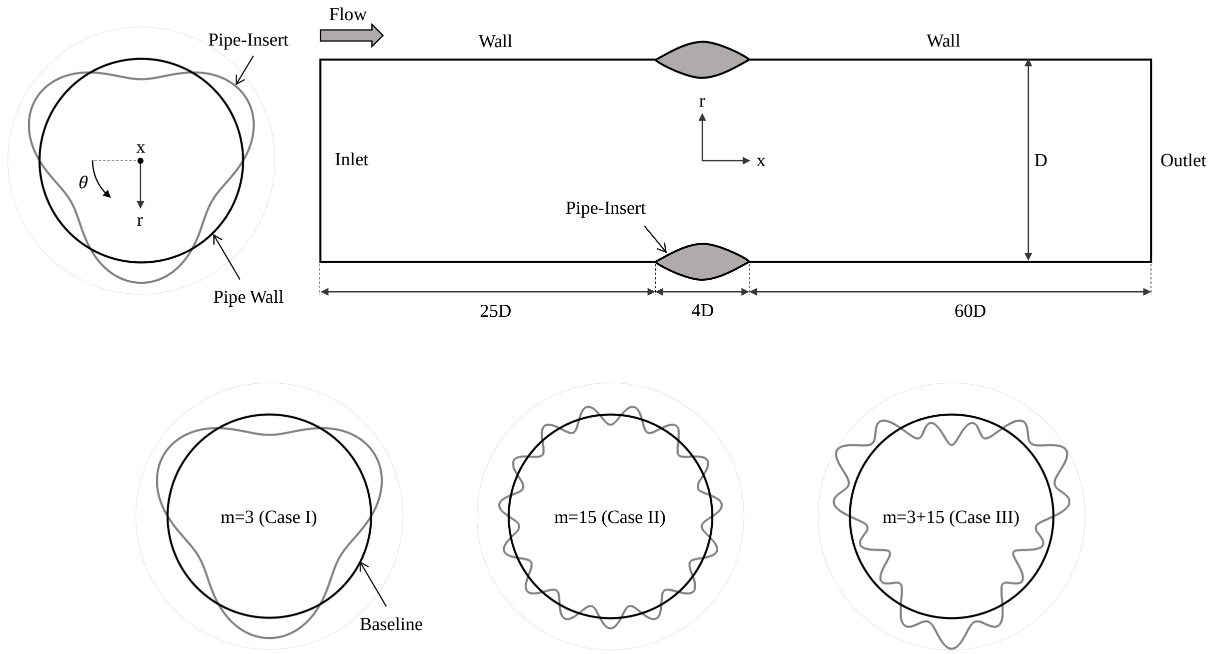

Figure 4.1: Schematic of the computational domain utilized in this study (not to scale) is shown in the first row while the pipe-insert cross-sections at $x/D = 0$ are shown in the second row.

Case I, $a_m = 0.1$ for Case II, and $a_m \in \{0.2, 0.1\}$ for Case III. The cross-sectional area of the pipe-insert followed $\Delta A = 0.5 \sum_m (2a_m/D)^2$ with a maximum change of 2%, 0.5%, and 2.5% for Case I, Case II, and Case III, respectively (Van Buren et al., 2017). Figure 4.1 presents schematics of the three-dimensional computational domain, which extended from $-27D$ to $+62D$ in the axial $(x-)$ direction. The cross-sections of three insert geometries are also depicted in Figure 4.1. The turbulent pipe flow sensitivity to the domain size was investigated by adjusting the outlet boundary location. Details on the domain sensitivity analysis are provided in later sections.

A non-homogeneous three-dimensional structured grid with a total of 12.2×10^6 hexahedral elements were used for the simulations. A higher density of grid elements was placed near the critical region of the pipe-insert segment while the grid expanded towards the inlet and outlet boundaries with a maximum expansion ratio of 1.02 (see Figure 4.2. The adequate refinement of spatial grid close to the inlet boundary, which followed a separate long section of a smooth pipe, allowed a stable transition of the fully-developed inflow profile.

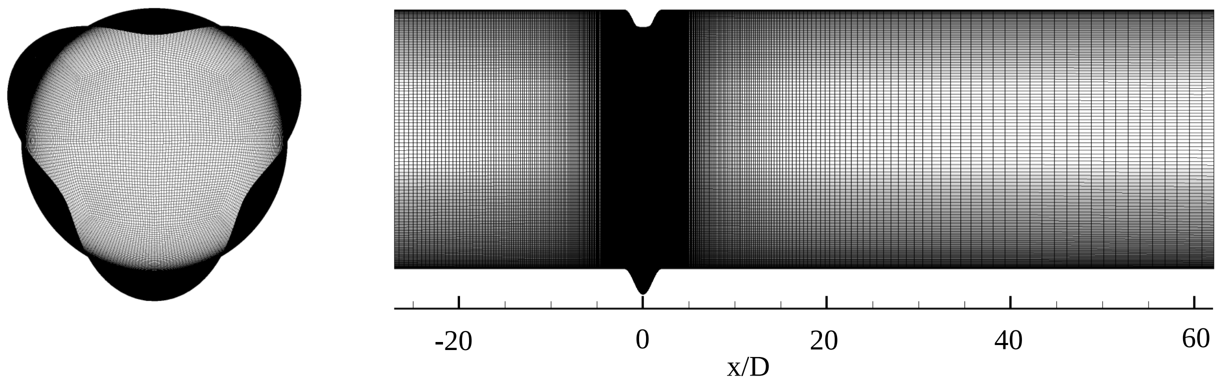

Figure 4.2: Schematic of spatial grid over the cross-sectional area and central plane of the pipe (scales are different in radial and axial directions). Case I is shown as an example.

At the inlet boundary, a three-dimensional fully-developed turbulent inflow condition was applied, i.e., Dirichlet and Neumann boundary conditions for velocity and pressure fields, respectively. This condition was mapped from a fully-developed outlet profile of a smooth pipe. The length of the three-dimensional smooth pipe was $220D$, similar to the domain size considered in experiment (Van Buren et al., 2017). This allowed us to perform a validation study using available literature at high Re, e.g., Zagarola et al. (1996) and Smits et al. (2019). The Neumann boundary condition ($\partial\varphi/\partial n = 0$, where φ is any flow variable) was imposed at the outlet boundary, which was located far from the pipe-insert segment ($60D$). The no-slip boundary condition along with a standard wall function (Liu, 2016) was set at the walls. The upstream friction velocity (u_τ) for all three cases was obtained based on McKeon et al. (2004) correlations and the friction Reynolds number was $Re_\tau = \rho u_\tau D/\mu = 7144$.

All simulations were performed in OpenFOAM, which is a finite-volume-based open-source platform (Versteeg and Malalasekera, 2007). The Standard $k-\varepsilon$ turbulence model (Launder and Spalding, 1983) was further employed based on previous studies that had shown it to perform better than the Realizable $k-\varepsilon$, $k-\omega$, and SST $k-\omega$ models in simulating such flows (Morrison et al., 1993; Shah et al., 2012), and providing accurate predictions for the mean flow compared to experiments, especially at high Re cases (Goswami and Hemmati, 2020). This has been further validated for simulating turbulent pipe flow by

Goswami and Hemmati (2020, 2021). A validation analysis was also performed for a three-dimensional smooth pipe using the Standard $k - \varepsilon$ turbulence model, the details of which are included in the next section. The second-order accurate bounded numerical schemes were utilized for discretizing both advection and diffusion terms. The convergence criteria were set based on reducing root-mean-square (rms) of momentum residuals below 10^{-5}. The discretized equations were solved using simpleFoam, which is a steady-state solver for incompressible, turbulent flows based on *Semi-Implicit-Pressure-Linked-Equation* (SIMPLE) algorithm (Greenshields, 2015). All simulations were conducted using Compute Canada clusters, each with 40 CPUs in parallel and 160 GB of memory over ≈ 120 simulation hours.

4.4 Validation and Verification

A series of verification and validation studies were carried out to ensure the accuracy of numerical simulations compared to available experimental results, e.g., Smits et al. (2019), and Zagarola et al. (1996). The flow field was normalized using the pipe diameter and radius, $D = 2R$, the maximum value of mean velocity from the fully-developed profile, i.e., bulk velocity U_b, bulk velocity at the inlet, U_∞, and upstream friction velocity (u_τ).

4.4.1 Domain Sensitivity

The effects of domain size on numerical results were examined using three cases with axial domain lengths of $59D$ (Domain 1), $69D$ (Domain 2), and $89D$ (Domain 3). Particularly, we examined the implications of the separation distance between the outlet boundary and the critical flow region. These cases were based on pipe insert configuration of azimuthal Fourier mode $m = 3 + 15$ (Case III) at $Re = 1.58 \times 10^5$. The main quantity of interest was the change in mean velocity and turbulence kinetic energy along the pipe centerline downstream of the perturbation. Figure 4.3 shows that two traced flow features were not sufficiently developed in the downstream region using Domain 1 and Domain 2. The presented results

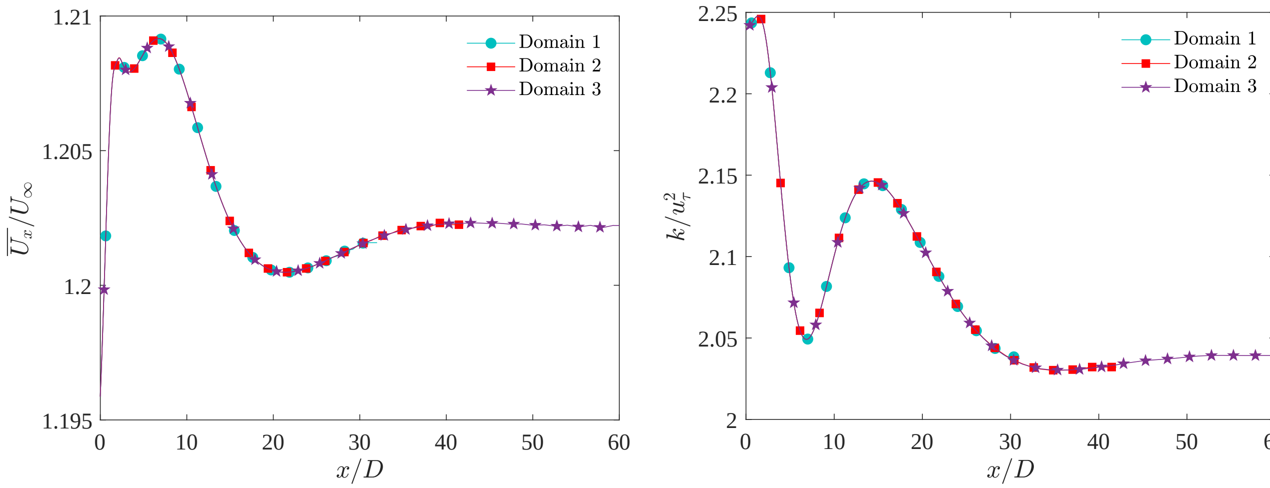

(a)

(b)

Figure 4.3: Effect of domain size on (a) mean axial velocity and (b) turbulence kinetic energy.

confirm that Domain 3 ($89D$) had sufficient axial length to properly capture the recovery of disturbed turbulent pipe flow at the highest Reynolds number studied here. The very small variations ($< 1\%$) between these cases indicated that the outlet boundary condition has no significant impact on simulating the critical flow region immediately after the pipe insert. Thus, Domain 3 was employed for all the simulations in this study.

4.4.2 Grid Sensitivity Analysis

The grid sensitivity study was designed by successively refining the hexahedral grid distribution based on the first cell spacing, which dictates the vertical extent from the wall at which equilibrium laws hold, and the grid resolution in the circumferential direction. The results from five grids are presented for Case III ($m = 3 + 15$) at $Re = 1.58 \times 10^5$. Table 4.1 outlines the parameters for each grid. For brevity, the mean flow and turbulent field results are presented only at $x/D = 11$. Velocity profiles in Figure 4.4 show a difference of less than 3% between Grid 4 and Grid 5. Reynolds shear stress profiles obtained for all grids indicated a difference of less than 3%. Thus, it is apparent that Grid 4 is adequate in capturing the mean flow features and the turbulent field in the current study.

Table 4.1: Details of the grid distributions based on Case III. Δx^+ and $\Delta\theta^+$ correspond to spacing in the streamwise and circumferential directions in wall units based on inflow parameters, respectively.

Study	First Cell (r^+)	$\Delta\theta^+$	Δx^+	Number of Cells
Grid 1	16	110	98	6.70×10^6
Grid 2	4	95	165	8.95×10^6
Grid 3	4	95	127	10.37×10^6
Grid 4	4	95	98	12.20×10^6
Grid 5	2	94	98	14.49×10^6

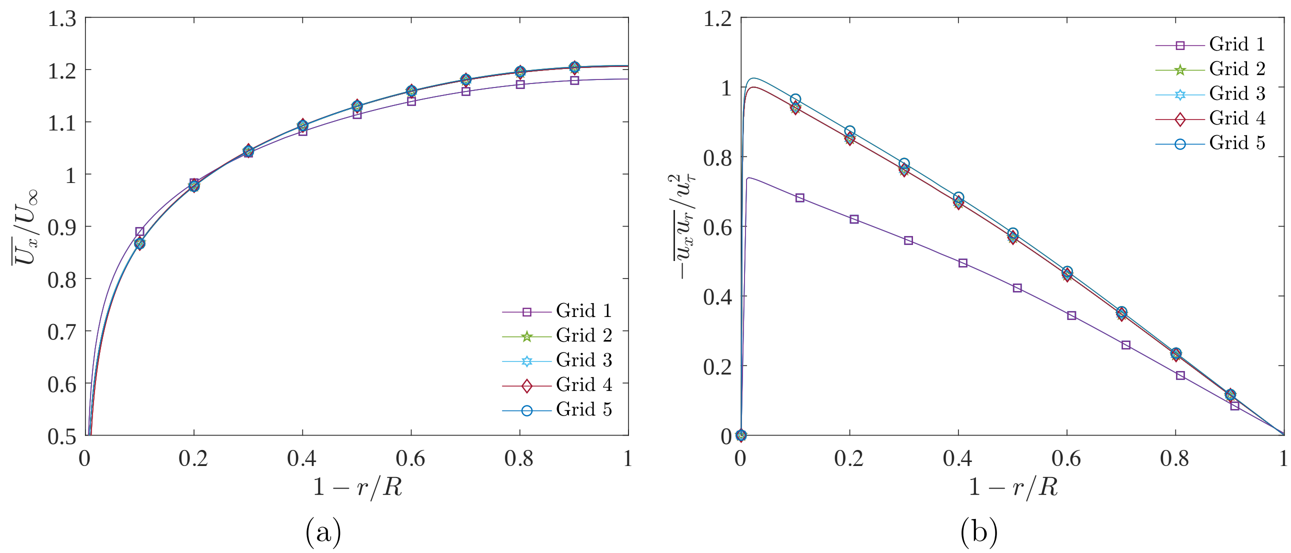

Figure 4.4: Effect of grid refinement on (a) mean axial velocity and (b) Reynolds shear stress.

4.4.3 Validation of Turbulence Model

The accuracy of numerical simulations is validated by comparing the radial mean velocity profile with experimental data. The simulation was performed for a fully-developed flow at $Re = 1.58 \times 10^5$ in a smooth pipe with a total length of $220D$ using the Standard $k - \varepsilon$ turbulence model. The numerical simulation was further performed using Realizable $k - \varepsilon$ and SST $k - \omega$ turbulence models whose results were also compared with experimental data. These results (not shown here for brevity) confirmed the better performance of Standard $k - \varepsilon$ turbulence model in accurately predicting the main flow features. The mean axial velocity profiles of the smooth pipe ($\overline{U_x}/U_\infty$) in Figure 4.5(a) exhibited a close agreement

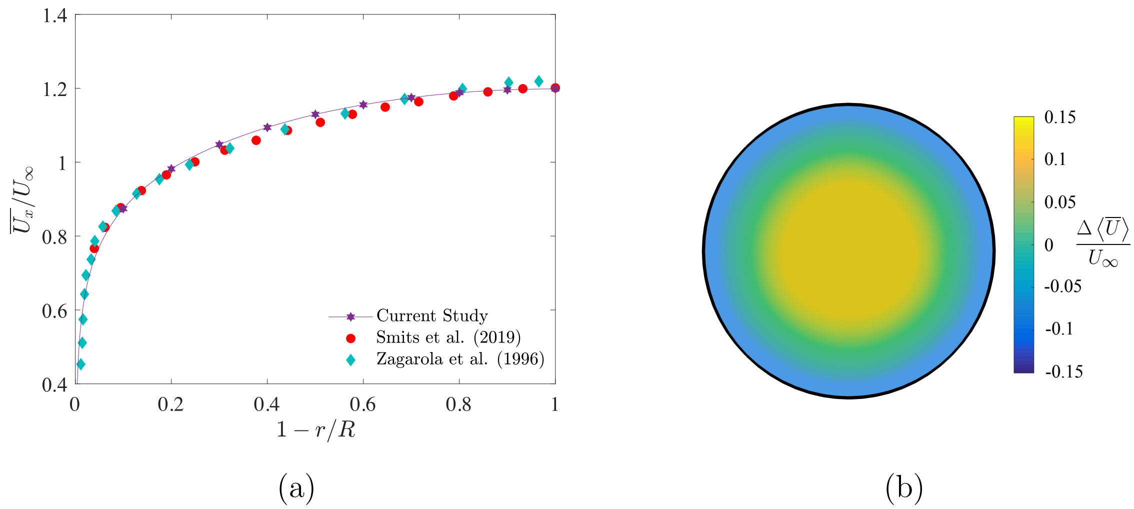

Figure 4.5: Comparison of the mean axial velocity profiles (a) between simulation and with experimental data at similar Re. (b) shows the mean axial velocity contour plot extracted at $x = 5D$.

with experiments of Smits et al. (2019) and Zagarola et al. (1996), for both the core region and close to the wall. The maximum mean centerline velocity was found to be within 3% of the experimental data. The validation study was further extended in Figure 4.5(b) to compare the mean axial velocity contour with those provided by Van Buren et al. (2017) at a similar location and Re for the same targeted modified wall shape. Here, $\Delta\left\langle\overline{U}\right\rangle = \overline{U_x} - U_\infty$. The comparison of our numerical data with experimental results provided in *Figure 3c* of Van Buren et al. (2017) suggested a good agreement, which provides more confidence in the current numerical setup. This conclusion was also consistent with previous studies that assessed the accuracy of numerical simulations and Standard $k-\varepsilon$ turbulence model: e.g., Durst and Wang (1989), Shah et al. (2012), Cappelli and Mansour (2013), Yamagata et al. (2014), and Goswami and Hemmati (2020). Therefore, the Standard $k-\varepsilon$ turbulence model was utilized to study the effects of various pipe-insert geometries on the mean flow properties and the recovery of turbulent pipe flow.

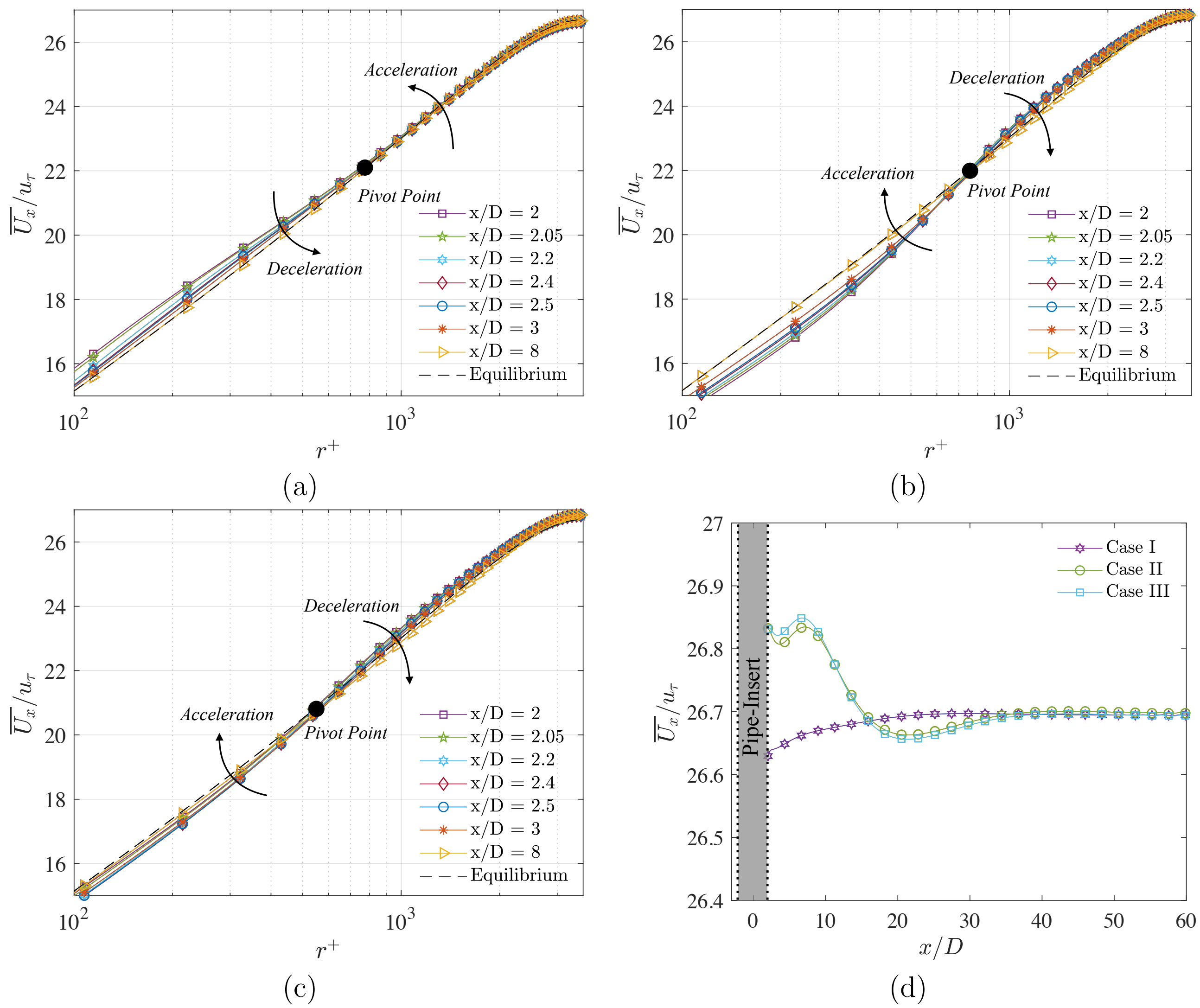

Figure 4.6: Mean axial velocity profile development for (a) Case I, (b) Case II, (c) Case III. (d) depicts axial variation along the wake centerline for all three cases.

4.5 Results and Discussion

The modified turbulent pipe flow response is first assessed through variation in mean axial velocity profiles along the radial direction for all three cases in Figure 4.6(a-c). The assessments were made at several axial locations downstream of the pipe-insert segment. The mean axial velocity ($\overline{U_x}$) was normalized by the friction velocity (u_τ), while the pipe radius was normalized by $r^+ = ru_\tau/\nu$. We examined the recovery of $\overline{U_x}/u_\tau$ within $2D - 8D$ downstream of the perturbation by tracking its overshoot and undershoot as well as its relaxation toward the equilibrium state. Data are shown for $r^+ > 10^2$ in order to assess the dominant flow response characteristics more clearly. Case I showed deceleration of $\overline{U_x}/u_\tau$ at $r^+ \approx 10^2$ and its acceleration in the outer region, $r^+ \approx 10^3$. Contrarily, Case II and Case III exhibited an increased axial velocity when approaching the wall ($r^+ \approx 10^2$), which decelerated near the outer region of the flow at $r^+ \approx 10^3$. We further observed that at $r^+ \approx 10^2$, all three cases retrieved their equilibrium state within $x = 8D$. The fully-developed state of the mean axial velocity was obtained by "pivoting" (Van Buren et al., 2020) about a central point to balance the velocity deficit. This was in agreement with the approach of Van Buren et al. (2020), which attributed the balance of velocity profile to characteristics of enclosed flows (e.g., pipe and channel flows).

In the present study, the asymptotic behavior was defined based on consecutive variations of less than 1%. In order to examine the mean axial velocity variation within the core flow region, we looked at the wake centerline profiles depicted in Figure 4.6(d). Due to the contraction of incoming flow within the pipe-insert, the mean axial-flow was observed to accelerate for all three cases. A similar overshoot response in the mean velocity distribution have been previously observed in different types of non-equilibrium flows, such as the recovery of a boundary layer from a short region of Smits et al. (1979). Case I revealed a monotonic response in approaching the fully-relaxed state while depicting recovery by $x \approx 16D$. However, Case II and Case III presented a non-monotonic behavior, where the axial mean velocity profile exhibited two peaks. Case II resembled a stronger primary peak within the pipe-insert at $x \approx 1D$ while the primary peak for Case III was located at $x \approx 2.2D$, which is outside the pipe-insert segment. Additionally, the axial location of second peak was found similar for these two cases at $x \approx 7D$. The acceleration of flow caused long-lasting effects on velocity profiles of Case II and Case III, which introduced a delayed recovery process past $x = 20D$. This delayed recovery is preceded by an undershoot below equilibrium at $x \approx 21D$. The mean axial velocity gradually adjusted to the fully-developed state at $x \approx 34D$. Therefore, the oscillatory flow response accompanied by a

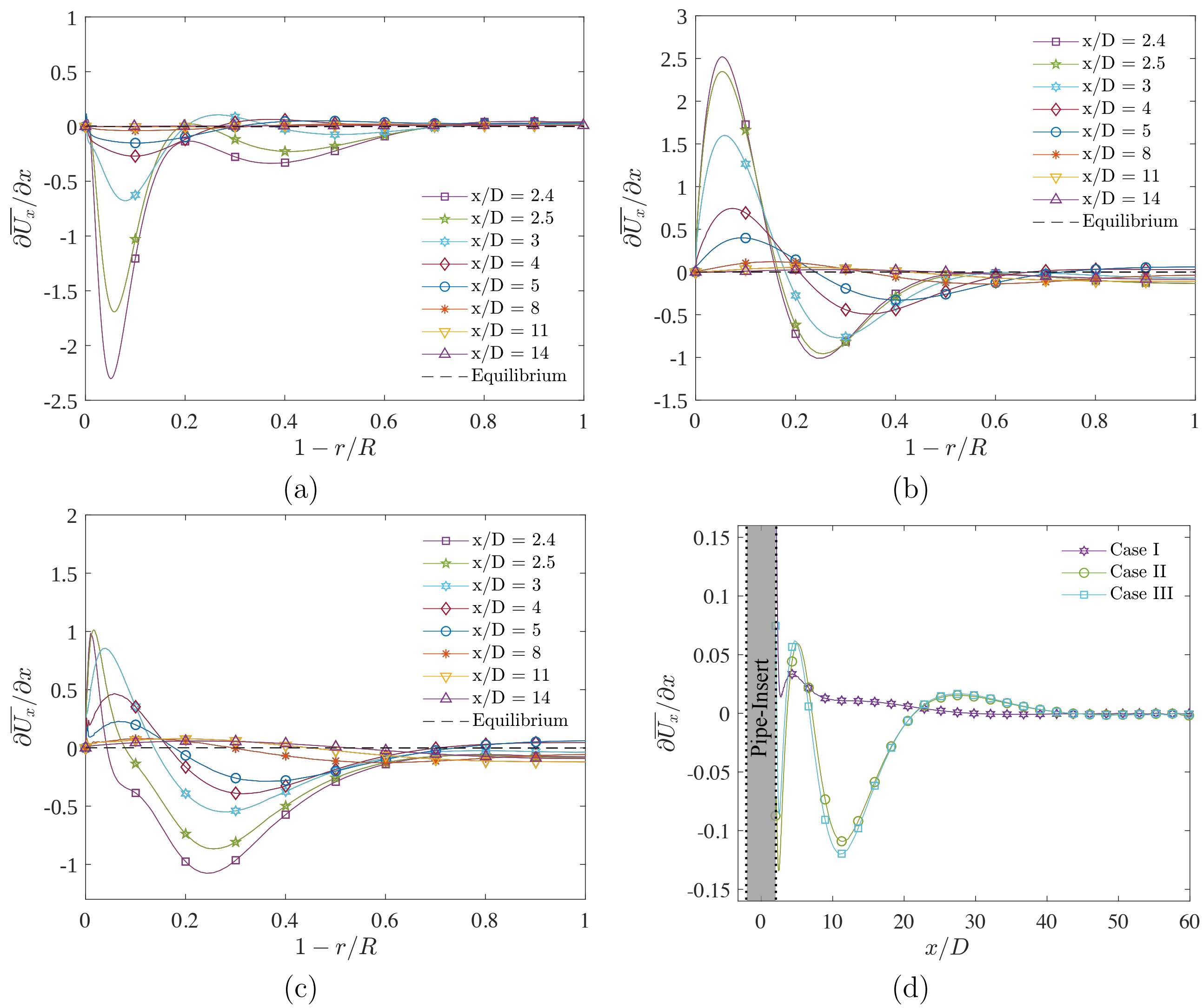

Figure 4.7: The mean axial velocity gradients along the pipe radius for (a) Case I, (b) Case II, and (c) Case III, and (d) the wake centerline for all three cases.

delayed recovery trend supports the existence of non-monotonic flow behavior. This remains consistent with observations on similar flows undergoing recovery past perturbation, such as Smits et al. (1979), Smits et al. (2019), Van Buren et al. (2020).

To further explore the mean flow features, the response of mean axial velocity gradient ($\partial \overline{U_x}/\partial x$) was investigated at several axial locations downstream of the perturbation. The radial profiles of $\partial \overline{U_x}/\partial x$ are shown in Figure 4.7(a-c). For all three cases, a larger magnitude of the velocity gradient was identified in regions corresponding to $r/R \to 1$. The collapse of velocity gradients is apparent near the pipe centerline ($r/R \to 0$), which was consistent with

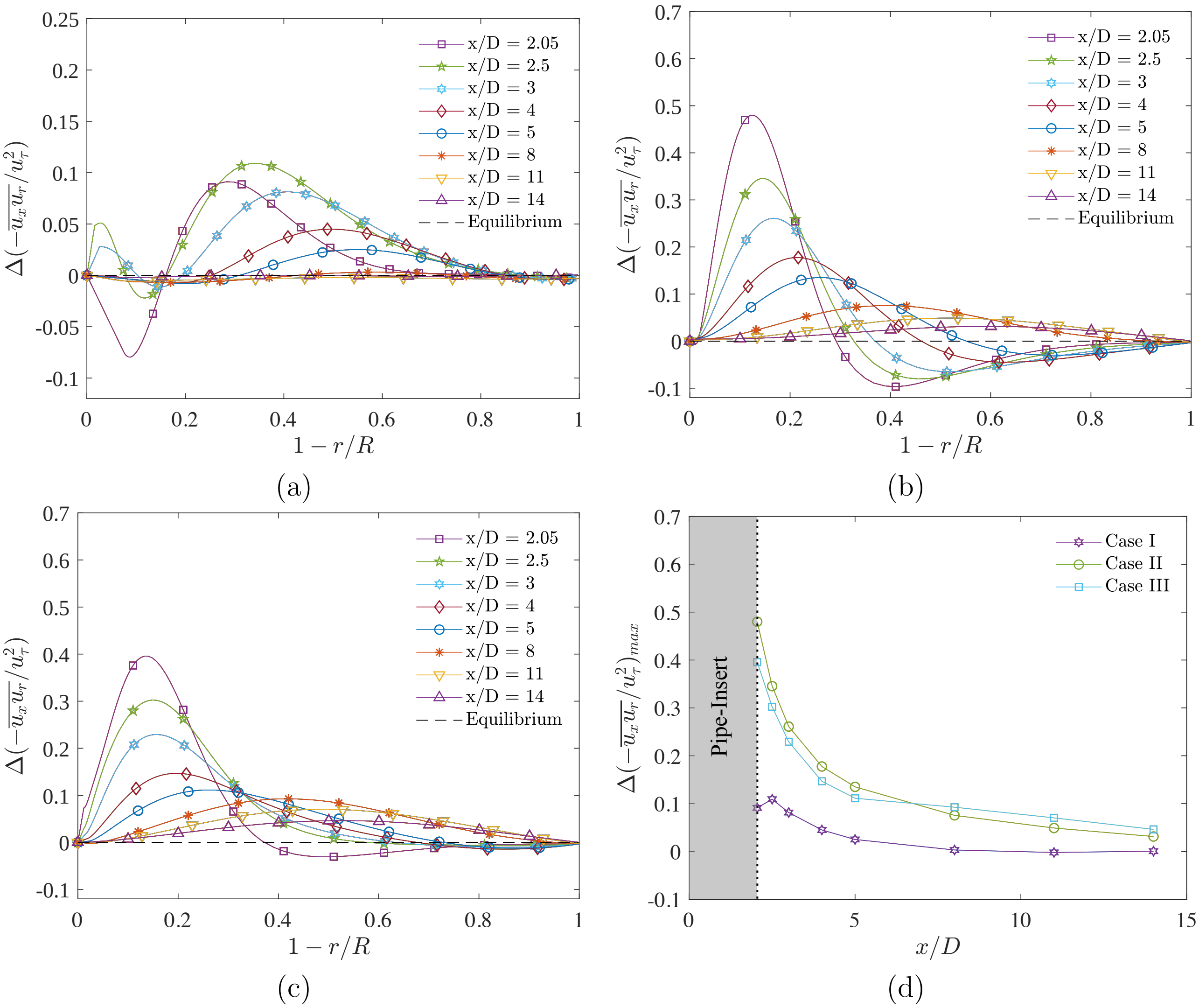

Figure 4.8: The mean axial (streamwise) Reynolds shear stress along the pipe radius for (a) Case I, (b) Case II, and (c) Case III. Downstream variation of the peak in $-\overline{u_x u_r}$ are shown in (d) for all three cases.

findings of Goswami and Hemmati (2020) for the case of a square bar roughness element with a similar height. Furthermore, the overshoot of velocity gradients attenuated and approached a self-similar state ($\partial\overline{U_x}/\partial x = 0$) as the flow gradually recovered in the downstream region. This was further in accordance with Smits et al. (2019), where the overshoot of velocity gradients in the wake region was attributed to the contraction of incoming flow on account of the square bar roughness. Moreover, negative values of $\partial\overline{U_x}/\partial x$ for Case I at wall-normal location of $0 < 1-r/R < 0.2$ coincided with deceleration observed in the mean axial velocity field close to the wall (Figure 4.6(a)). The slow recovery of $\partial \overline{U_x}/\partial x$ to the fully-developed state hinted at long-lasting impacts of the perturbation on flow, which led to a delayed recovery process. A close inspection of the centerline profile for $\partial \overline{U_x}/\partial x$ in Figure 4.7(d) revealed that Case I had a monotonic recovery trend, similar to the mean axial velocity in Figure 4.6(d), where $\partial \overline{U_x}/\partial x$ recovered within $x \approx 12D$. However, Case II and Case III showed a second-order oscillatory behavior, where the equilibrium was not achieved until $x \approx 38D$.

The variation of Reynolds stresses ($-\overline{u_x u_r}$ and $\overline{u_x{}^2}$) was examined in Figure 4.8 to assess the impacts of perturbed flow on immediate turbulence response. Downstream of the perturbation, all three cases depicted a fast decay of Reynolds stresses, which also appeared to have an overshoot above the equilibrium profile. This observation agreed with previous studies of similar flows (Smits et al., 2019; Van Buren et al., 2019; Ding et al., 2019; Van Buren et al., 2020). Downstream development of the Reynolds shear stresses with respect to fully-developed flow, as depicted in Figure 4.8(a-c), was assessed in terms of the difference with respect to the equilibrium state, $\Delta(-\overline{u_x u_r}/u_\tau{}^2)$. The flow corresponding to Case I showed that higher Reynolds shear stresses were concentrated at $0.2 < 1 - r/R < 0.6$, while the concentration was closer to pipe wall at $0 < 1 - r/R < 0.4$ for the other wall shapes. Smits et al. (2019) described that a fully-developed state was attained when additional near-wall turbulence moves away from the wall. This provided us a hint for a faster recovery process in Case I, which was also observed previously with respect to $\overline{U_x}/u_\tau$ and $\partial \overline{U_x}/\partial x$. Further, the maximum shear stress decayed and transported away from the wall towards the center of the pipe for all three cases. This behavior was also in agreement with recent studies on perturbed high Re flows (Smits et al., 2019; Goswami and Hemmati, 2020, 2021) or flows past sudden changes in wall roughness (Van Buren et al., 2019, 2020). The maximum perturbation height of the geometry considered in this study was $0.1D$, $0.05D$, and $0.15D$ for Case I, Case II, and Case III, respectively. This was comparable to perturbation heights of $0.05D$ and $0.1D$ assessed by Smits et al. (2019). This allowed us to compare the maximum overshoot of shear stresses between these two studies. The peak in $-\overline{u_x u_r}$ observed here decreased by 94%, 88%, and 40% for Case I, Case II, and Case III, respectively. Despite close similarities in bulk flow characteristics (e.g., Re), there are expected to be differences in maximum overshoot values due to both differences in geometrical characteristics of the perturbations (square bar roughness with a sharp edge compared with smooth bump perturbation in our study) and the modeling effects. Figure 4.8(d) further showed the downstream changes in the peak for the initial response of shear stresses for all three cases. At $x = 14D$, Case I attained recovery while shear stresses for Case II and Case III remained higher than the equilibrium state. A prolonged recovery process ahead of $x = 14D$ was therefore evident for Case II and Case III, along with an almost similar decay rate in $-\overline{u_x u_r}$.

The axial evolution of Reynolds normal stress ($\overline{u_x{}^2}$) is depicted in Figure 4.9, which represent the difference of $\overline{u_x{}^2}$ and the fully-developed (equilibrium) profile. Similar to Reynolds shear stress, all three cases exhibited an overshoot in response to the perturbation. Downstream of pipe-insert along the centerline, $\overline{u_x{}^2}$ initially increased. Van Buren et al. (2020) attributed the increment of $\overline{u_x{}^2}$ along the wake centerline to the response of mean axial velocity due to the balance of continuity. This was also in accordance with the flow acceleration along the centerline that was previously shown in Figure 4.6(d). For all three cases, the flow response near the pipe center was found different from that of regions located closer to the wall, wherein the initial amplification of turbulence was followed by a decay in downstream region. Since the initial turbulence response was in the near-wall region (Van Buren et al., 2020), the location closest to the pipe-insert showed a peak at a distance of $\approx 0.2R$ from the wall. The peak gradually decayed and widened in far downstream regions and eventually moved away from the wall. This trend had been observed previously in flow over a square bar roughness (Smits et al., 2019) and flow across a step-change in wall roughness (Van Buren et al., 2020) at such high Reynolds numbers. Case I showed the least variation in $\overline{u_x{}^2}$ compared to other wall shapes, while obtaining a relaxation within $x = 14D$. However, Case II and Case III presented a second-order response with a peak

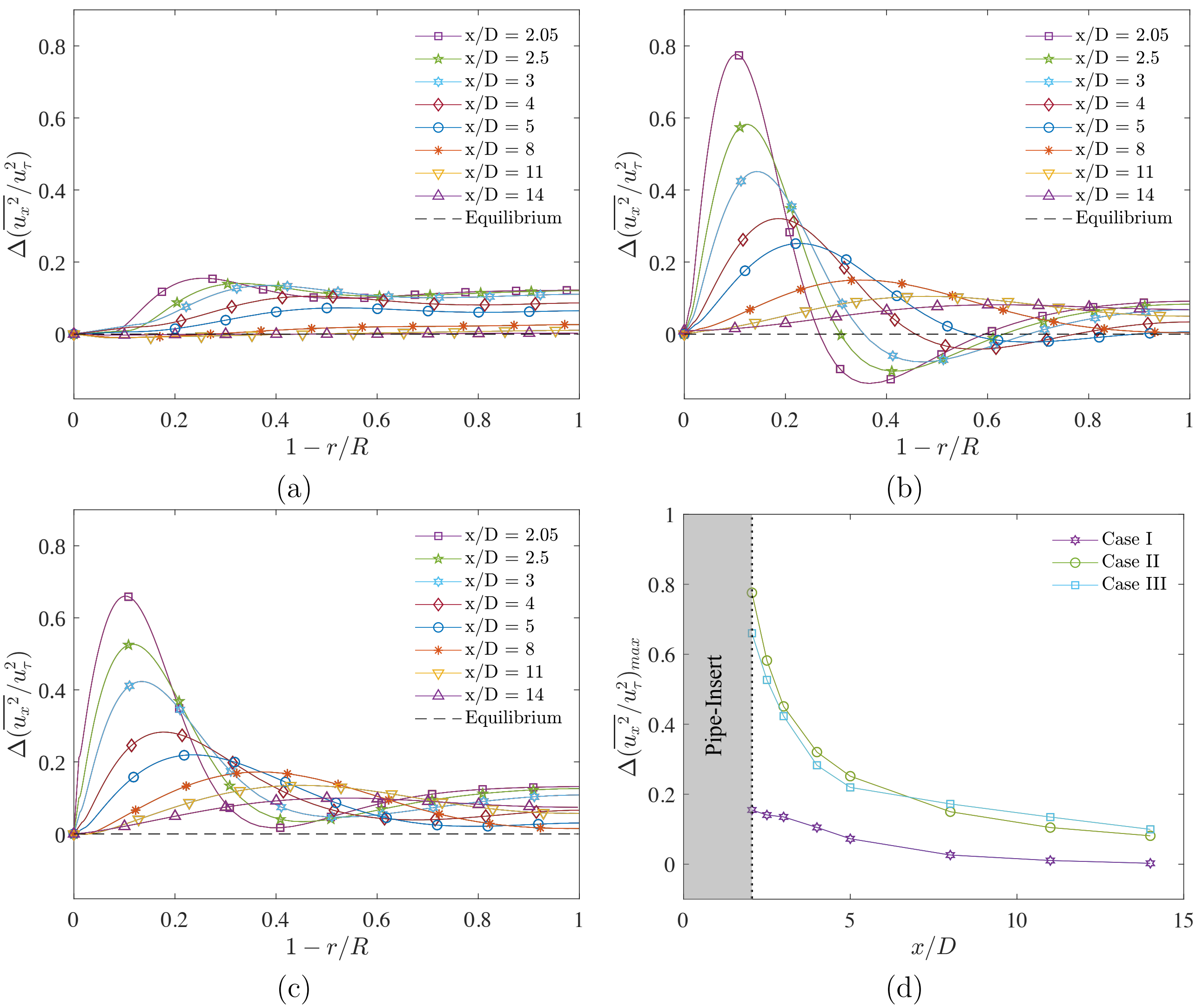

Figure 4.9: The mean axial (streamwise) Reynolds Normal stress along the pipe radius for (a) Case I, (b) Case II, and (c) Case III. Axial variation of the peak in $\overline{u_x}^2$ is shown in (d) for all three cases.

at $\approx 0.2R$ from the wall. A slow recovery rate caused the overshoot of $\overline{u_x}^2$ for these cases to remain higher than the fully-developed (equilibrium) state even at $x/D = 14$. The axial variations in the maximum values of $\overline{u_x}^2$ for all three cases are also exhibited in Figure 4.9(d). Despite the similar response behavior between Reynolds shear and normal stresses, they depicted different recovery rates. This could be associated with differences in turbulence energy budget ahead of the pipe-insert.

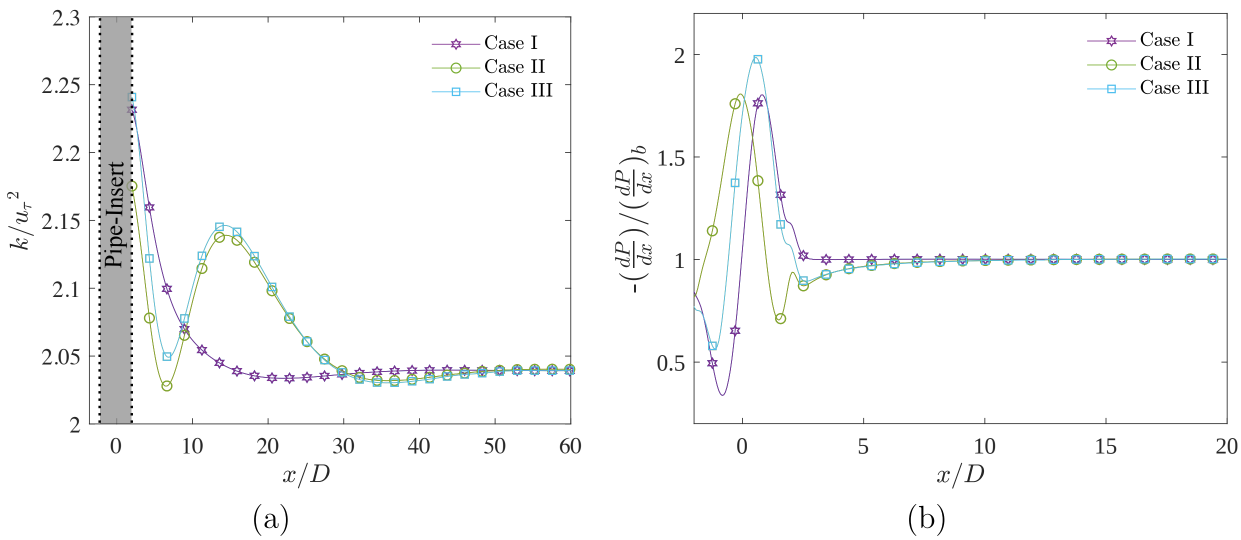

Figure 4.10: Axial development of (a) turbulence kinetic energy (k) and (b) the pressure gradient (dp/dx) along the wake centerline.

As suggested earlier, the turbulent features show different variations in the core compared to regions close to the pipe wall. Hence, the evolution of mean centerline turbulence kinetic energy (k) normalized by friction velocity (u_τ), and mean axial pressure gradient (dp/dx) normalized by the far downstream value ($x = 60D$), are depicted in Figure 4.10. Downstream of the pipe-insert ($2 < x/D < 7$), an initial sudden drop in turbulence kinetic energy was observed for all three cases. Case I again depicted a monotonic recovery trend with the flow being recovered at $x \approx 19D$. Case II and Case III, however, represented a different characteristic recovery trend. $k/u_\tau{}^2$ consisted of a secondary peak at $x \approx 14.5D$ followed by a fall below their fully-developed (equilibrium) values at $x \approx 36D$. Finally, the flow asymptotically reached a fully recovered state at $x \approx 45D$. The long-lasting and oscillatory recovery trend therefore resembled the second-order response, which was consistent with the study of Van Buren et al. (2020). Furthermore, within the pipe-insert section ($-2 \leq x/D \leq 2$), a large pressure gradient was evident for all three cases compared to equilibrium state values. Case I recovered within $1D$ ahead of the pipe-insert. Case II and Case III presented a similar recovery rate with a fully-relaxed state attained at $x = 14D$. This relatively fast recovery suggested that the velocity variations have greater contribution

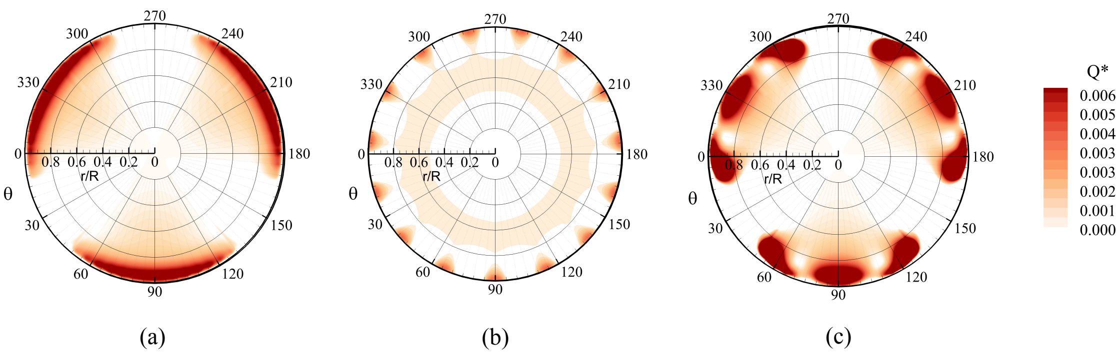

Figure 4.11: The Q-criterion contour plots for (a) Case I, (b) Case II, and (c) Case III.

towards determining the overall flow recovery behavior compared to pressure gradients. In comparison with the study of turbulent pipe flow response to rough-to-smooth step-change in roughness (Van Buren et al., 2019), axial pressure gradients depicted a delayed recovery by 40% that could be associated with the differences in Re and geometrical characteristics of the current study.

The results thus far hint that higher Fourier modes implemented in the wall shape dominate the flow disturbance and recovery. This was particularly supported by the consistency in flow recovery and response past wall shapes corresponding to the higher Fourier mode of 15 (Case II) and the superposition shape of 3 + 15 (Case III), while there were topological differences with $m = 3$ in Case I. Case II and Case III exhibited similarities in the recovery behavior of "global quantities" (Van Buren et al., 2020) (i.e., $\overline{U_x}/u_\tau$, dp/dx) as well as turbulence properties (i.e., $k/{u_\tau}^2$). The longer-lasting effect of the perturbation, which exhibited the same height, also indicates that wall modifications following a higher Fourier mode will have more profound effects on the flow. To further depict the similarities in flow features, we investigated the regions dominated by high rotations that might be evident in the downstream wake of pipe insert geometries. Figure 4.11 depict the contour plots of normalized Q-criterion ($Q^* = QD^2/U_\infty^2$) at $x = 2.5D$ for all three cases. Case I reflected three regions of high rotation, with each extending 60^o along the azimuthal direction. Case II, however, presented fifteen localized regions of high rotations that were evident at each

30^o interval along the wall. These regions also coincide with the geometrical feature of each case, where the maximum perturbation height was located (see Figure 4.1. The dominant effects of geometry observed for Case I and Case II also seem to be evident for Case III (with a superposition Fourier mode), wherein the wide regions of high rotation (observed in Case I) seem to be broken into localized elliptical regions. This appears to combined the effects from Case I and Case II. Since Case II and Case III depicted a high concentration of Reynolds shear and normal stress in the region of $0 < 1 - r/R < 0.4$, it is hypothesized that the formation of multiple localized regions of high rotation along the wall contributes to the initial intensification of Reynolds stresses, and possible disturbance of large-scale and very-large-scale motions. Thus, they lead to a prolonged recovery. Moreover, this is analogous with the experimental study of Van Buren et al. (2017) at a similar Re, which concluded that targeted Fourier mode wall shapes produced the intended flow structures (according to their corresponding Fourier mode number), and the effect of Case I with an azimuthal Fourier mode of $m = 3$, and Case II with $m = 15$ was evident in azimuthal structures of Case III with $m \in \{3 + 15\}$. These results hint at the need to expand our analysis in future studies to near-wall turbulent features, including large-scale and very-large-scale motions, and their disturbances induced by the targeted wall shapes.

4.6 Conclusions

The turbulent pipe flow response to wall changes that target particular Fourier modes ($m =$ 3, 15, and $3 + 15$) was investigated numerically at Reynolds number of 1.58×10^5. The mean axial (streamwise) velocity along the centerline depicted acceleration at $x = 2D - 7D$ for all three cases due to flow contraction within the pipe-insert. Cases of $m = 15$ and $3 + 15$ depicted two peaks in the velocity profile, which indicated characteristics of a second-order response. The response of turbulent field due to these wall modifications further indicated a second-order feature similar to a channel flow with abrupt variations of surface roughness (Saito and Pullin, 2014). A faster recovery in mean flow properties compared to the turbulent field was also observed, which was also identified in a turbulent pipe flow past a sudden change in wall roughness at high Reynolds numbers (Van Buren et al., 2020). Contrarily, the case of $m = 3$ depicted a non-oscillatory trend corresponding to a monotonic response. In particular, the lower Fourier mode wall shape demonstrated a faster recovery in both mean flow and turbulent features in comparison with the other two cases. The flow disturbance, response, and recovery due to the wall shape modifications corresponding to the higher Fourier mode ($m = 15$) dominated when low and high modes were combined ($m = 3 + 15$). This hinted at a relatively more significant impact of the higher Fourier mode wall modifications on the boundary layer structures (Adrian, 2007). In addition, the Q-criterion contours depicted regions dominated by high rates of rotation in the downstream wake. The presence of intermittent regions instead of wide distributed regions with a high rotation rate suggests a greater capability to concentrate Reynolds shear and normal stresses closer to the wall and for a longer axial distance. This could lead to a prolonged recovery process observed for cases corresponding to wall shape modifications based on higher Fourier modes.

Chapter 5

EFFECTS OF REYNOLDS NUMBER

5.1 Introduction

The implications of Reynolds number on the flow response and recovery are examined numerically using the Standard $k - \varepsilon$ turbulence model at $Re = 5 \times 10^3 - 1.58 \times 10^5$. The long-lasting flow response was examined by characterizing both the mean and turbulent field in the wake of pipe insert targeting Fourier mode of $3 + 15$ for each Reynolds number case. This chapter addresses primary objectives (3) and (4) of the thesis on the effects of Reynolds number variation on the flow behavior of targeted wall shapes outlined in Section 1.5. The chapter is structured so that the problem description and numerical setup are presented in Section 5.3, followed by a brief review of the verification and validation in Section 4.4 and presentation of the results and discussions in Section 5.5. The summary of the main findings are presented in Section 5.6.

5.2 Background

The response and recovery of wall-bounded flows to an abrupt change in surface condition have great importance in the engineering design of various systems, e.g., energy transport in pipelines and ship architecture. Turbulent flows at high Reynolds number (Re) that experience abrupt variations in surface conditions correspond to a class of perturbed or non-equilibrium flows that have not received sufficient attention (Van Buren et al., 2019), such as the flow over a small step (Smits et al., 2019; Jiménez, 2004; Goswami and Hemmati, 2020), forward and backward-facing step (Van der Kindere and Ganapathisubramani, 2018), or variations of the surface roughness (Van Buren et al., 2019, 2020; Saito and Pullin, 2014; Li et al., 2019). According to Jiménez (2004), small-sized steps that act similar to isolated roughness elements can impose a considerable impact on drag and induce significant changes in the downstream wake with different operational benefits (Ji and Wang, 2010). Despite several studies on pipe flow response to rough surfaces, a knowledge gap exists on the association of canonical wall-bounded turbulence (that is confined by a flat plate or parallel walls) with flows that encounter modifications of the surface condition. The streamlined curvature and pressure gradients significantly affect the turbulence behavior for flows over non-uniform cross-sectional regions and uniquely curved boundaries (Ding et al., 2019). These types of flow can be recognized in the energy industry (Yin et al., 2021), agriculture production (Feng et al., 2020), medicine (Hatoum et al., 2019), marine vehicles (Smits et al., 2019), and biological processes (Van Buren et al., 2019, 2020).

The physics of perturbed and non-equilibrium flows have been the focus of many researchers for decades, which has enriched our understanding of pipe flow and wall-bounded turbulence. Antonia and Luxton (1971) investigated the effect of a step-change in surface roughness (from rough to smooth) on the turbulent boundary layer and observed a non-monotonic flow response. Later on, Smits et al. (1979) studied the impact of surface condition modification on turbulent pipe flow and identified that a turbulent boundary layer exposed to a short concave curvature region initially induced an intensification of Reynolds stresses, which was followed by a fast reduction below the equilibrium state. They attributed this phenomenon to the interaction of mean shear and turbulent shear stress. Thus, there was a second-order response that led to long-lasting changes in turbulent structures. Smits and Wood (1985) also observed a slow adjustment of the flow to the new wall conditions due to step changes. The non-monotonic response was not specific to flows encountering curvature changes as was identified in a very recent study (Van Buren et al., 2019).

The numerical study of Durst and Wang (1989) on the flow over an axisymmetric ring-type wall-mounted obstacle in a turbulent pipe flow revealed overshoot of the flow response (second-order response) in proximity of the obstacle (perturbation). This was consistent with experimental results, which along with similarities on other flow features predicted by Standard $k - \varepsilon$ turbulence model, indicated a good agreement between numerical and experimental data. Dimaczek et al. (1989) also performed an experiment on the surface-mounted obstacles at moderately high Reynolds number using two-dimensional planes and axisymmetric geometries. They concluded that the upstream flow condition affected the flow reattachment length in different geometries. This was then expanded by Durst et al. (1989), who experimentally studied the response of turbulent flow past an axisymmetric obstacle at a range of Reynolds numbers. They identified two peaks in the reattachment length based on variations with Reynolds number, which corresponded to $Re = 1.2 \times 10^3$ and $Re = 3 \times 10^4$. At $Re \geq 4 \times 10^4$, however, there was a slow change in the reattachment length. Similar observations were reported by Dimaczek et al. (1989) for flow response to an axisymmetric obstacle and sudden expansion at various Reynolds numbers.

Reynolds number scaling for turbulent pipe flow was another area of extensive research. Zagarola and Smits (1998) studied the mean-flow scaling of fully-developed turbulent flow in a smooth pipe at a range of Reynolds number between 3.1×10^4 and 3.5×10^7. They determined two scaling laws (inner and outer region scaling) based on wall-normal distance, and identified the existence of a logarithmic law between the inner and outer regions (logarithmic overlap region). Furthermore, a new velocity scale was proposed in the outer region that depicted better agreement at various Reynolds numbers. The influence of turbulent flow past rough walls was then examined by Jiménez (2004), who reported that small steps that act similar to the isolated roughness elements introduce a significant change in flow features, such as drag. Later on, Hultmark et al. (2010) reported a near-wall turbulence scaling in pipe flow at a range of Reynolds numbers ($2.4 \times 10^4 - 1.45 \times 10^5$). The inner scaling region near the pipe wall indicated a good collapse of turbulence intensity. A secondary peak in turbulence intensity with a lower magnitude emerged in the wake region while increasing Re. A similar observation was also reported by Hultmark et al. (2012) and Hultmark et al. (2013), which showed that there is a secondary peak in the wake region, and it is a genuine characteristic of high Re turbulent flow. Although several studies proposed $Re-$scaling methods for the mean-flow features in a smooth pipe, there remains a gap in predicting the scaling behavior for turbulent pipe flows undergoing modifications of wall shapes following specific azimuthal Fourier modes.

Van Buren et al. (2019) and Smits et al. (2019) were the most recent experimental studies of the response and recovery of flow past sudden changes in the surface condition. These studies looked at turbulent flow over a roughness element at $Re = 13 \times 10^4 - 16 \times 10^4$. Particularly, Van Buren et al. (2019) analyzed the flow response to a step-change in roughness. They observed the oscillatory response of the mean velocity and the distribution of shear stress, which did not indicate recovery even after $60D$ downstream of the step-change, where D is the pipe diameter. A similar overshoot phenomenon was observed for the Reynolds shear stress, where the peak was identified at the nearest location to the step change. Their results hinted at a second-order feature, which was previously observed in the flow downstream of the small area with concave curvature, where the boundary layer recovered from a step-change in surface roughness (Smits et al., 1979).

Smits et al. (2019) studied the behavior of perturbed flow past axisymmetric square bar roughness elements at $Re = 1.56 \times 10^5$ along with bar heights of $0.05D$ and $0.1D$. The flow past perturbation experienced contraction and expansion that caused the overshoot of flow response in the proximity of the roughness elements and imposed long-lasting changes in the downstream wake. A long-lasting recovery process occurred because of the slow rate of collapse in the Reynolds shear stress variation after an initial intensification close to the bar roughness. They further found that the Reynolds shear stress moved away from the wall, with a power-law trend, toward the center of the pipe which presented benefits such as extended zone of lower surface friction, lower turbulence levels, and reduced drag (Smits et al., 2019).

Senturk and Smits (2019) reported one of the more recent numerical studies on pipe flow over perturbations at lower Reynolds numbers. They examined the effect of multiple-tandem roughness elements in periodic arrangements on a fully-developed laminar pipe flow at Reynolds numbers between 200 and 2000. Particularly, they focused on the effect of Re variation on the friction factor. This was then expanded by Liu et al. (2019), who assessed the impacts of changing Re on response and recovery of fully-developed pipe flow at low Re. They found that the principal factor impacting the response and recovery behavior of the flow is the height of bar roughness elements and their separation distance.

Most recently, Goswami and Hemmati (2020) assessed the response and recovery of turbulent pipe flow over single and multiple square bar roughness elements (two heights) at $Re = 1.56 \times 10^5$ to determine the implications of the number of roughness elements, their periodicity and separation patterns on flow recovery. They also presented a benchmark study on the performance of Reynolds-Averaged-Navier-Stokes (RANS) models on simulating turbulent pipe flow response in the presence of small roughness elements. They reported that in comparison to experiments of Smits et al. (2019), the Standard $k-\varepsilon$ model performed better than other conventional turbulence models at high Reynolds numbers. The reasonable agreement of their numerical results with experiments implied that the Standard $k-\varepsilon$ RANS models can adequately predict the main flow features and capture the recovery and response of pipe flow due to small wall modifications, i.e., roughness elements. This conclusion was in agreement with findings of Cappelli and Mansour (2013) and Fogaing et al. (2019) on performance of RANS models in simulating pipe flows and wakes, respectively.

Liu et al. (2019), Smits et al. (2019), and Goswami and Hemmati (2020) have shown that upstream flow conditions, including Reynolds number variations and geometric perturbations, made a substantial contribution in the flow response and recovery. Hence, the effects of changing Reynolds number on response and recovery of the flow over modified wall shapes still require further examinations. The current chapter focuses on the implications of Reynolds numbers on turbulent flow recovery past pipe wall shapes targeting specific Fourier modes, which complements an earlier experimental study by Van Buren et al. (2017) at $Re = 1.58 \times 10^5$.

5.3 Problem Description

This chapter numerically examines response and recovery of fully-developed turbulent pipe flow past changes in wall configuration resembling azimuthal Fourier modes in wall-bounded turbulence. The Reynolds number varied between 5×10^3 and 1.58×10^5 based on the bulk flow, such that $Re = U_\infty D/\nu$, where U_∞ is the bulk axial velocity at the inlet of the smooth pipe, D is the pipe diameter, and ν is fluid kinematic viscosity. Moreover, the flow response was evaluated up to a distance of $60D$ downstream of the wall change. The change in the pipe wall was implemented through a pipe insert, the geometry of which was designed based on the experiments of Van Buren et al. (2017). The perturbations on inserts targeted three distinct azimuthal Fourier modes corresponding to $m = 3$ (Case I), $m = 15$ (Case II), and $m = 3 + 15$ (Case III). Amongst all three cases, the results for Reynolds number effects are only presented for Case III ($m = 3 + 15$). However, Reynolds number effects were also evaluated for Case I and Case II, which showed similar effects for all cases. Here, only results for Case III are provided for brevity. The implications of wall shapes on recovery are discussed in a future publication. The amplitude of the perturbation followed a sinusoidal

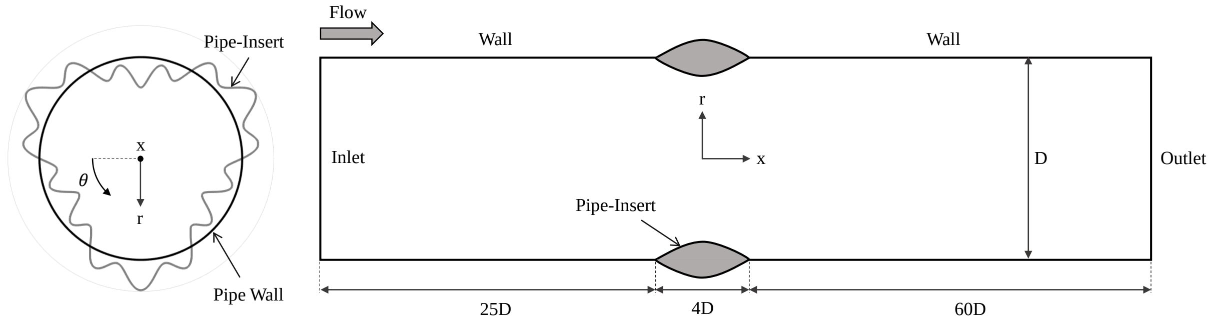

Figure 5.1: Schematic of the computational domain employed in this study (not to scale).

wave in the axial direction, while the formulation for the wall shape was:

$$r(\theta, m, x) = \frac{D}{2}\left[1 + \frac{cos(\frac{\pi x}{2D}) + 1}{2}\sum_{m} a_m sin(m\theta)\right] \tag{5.1}$$

Here, m denotes the Fourier mode, $\theta(\in [0, 2\pi])$ is the azimuthal angle, $x(\in [-2D, 2D])$ is the streamwise location, and D is the pipe diameter. Amplitude of the perturbation was $a_m = 0.2$ for Case I, $a_m = 0.1$ for Case II, and $a_m \in \{0.2, 0.1\}$ for Case III. Note that Case III is the superposition of Case I and Case II, with a maximum perturbation height of $0.15D$. The cross-sectional area of the pipe varied following $\Delta A = 0.5\sum_m (2a_m/D)^2$ with a maximum variation of 2.5% for Case III (Van Buren et al., 2017).

Schematics of the three-dimensional computational domain is shown in Figure 5.1, which extended from $-27D$ to $+62D$ in the axial ($x-$) direction. A non-homogeneous three-dimensional structured mesh was used for this analysis with a total of 12.2×10^6 hexahedral elements to simulate Case III at $Re = 1.58 \times 10^5$. For lower Re cases, a similar mesh was constructed with the same overall quality. A finer mesh was implemented near the pipe insert segment, while the grid expanded towards the inlet and outlet boundaries (see Figure 5.2) with a maximum expansion rate of 1.02. The average non-dimensional wall-normal distance (r^+) was maintained below 25 for the entire domain, which ensured proper modeling of the flow behavior in the logarithmic region, especially at high Re (Liu, 2016).

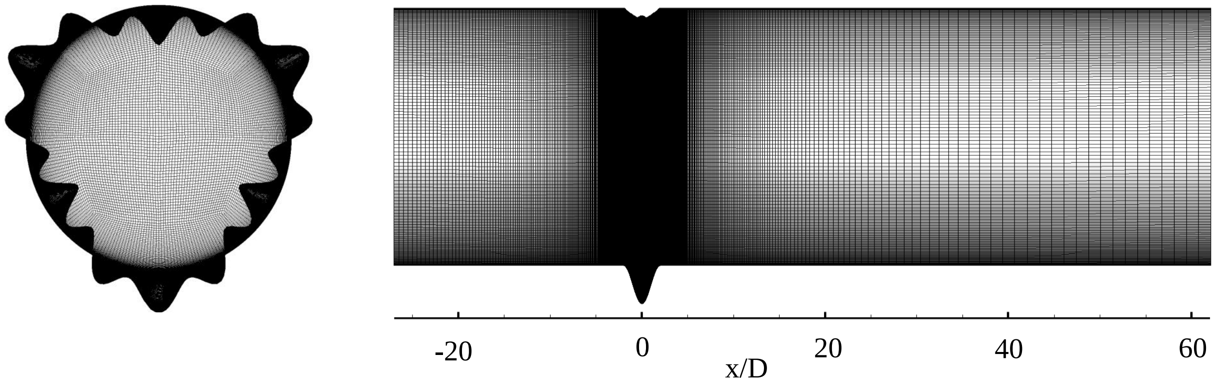

Figure 5.2: Screenshot of the spatial grid distribution over the cross-sectional area and central plane of the pipe (scales are different in radial and axial directions).

A fully-developed inflow condition was imposed on the inlet boundary, which was mapped from a fully-developed outlet profile of the smooth pipe case at the same Reynolds number. The overall length of the three-dimensional smooth pipe was $220D$, which allowed a fully-developed profile to be developed at the outlet. The mapped inflow conditions included the Dirichlet boundary condition for the velocity field and the Neumann boundary condition for pressure field (dp/dn =0). The Neumann boundary condition was applied for both velocity and pressure at the outlet boundary. For pipe walls, a no-slip boundary condition was imposed with a standard wall-function, details of which can be found in Liu (2016).

The upstream friction velocity (u_τ) for all cases were obtained based on the correlations of McKeon et al. (2004). The friction Reynolds number was defined as $Re_\tau = u_\tau D/\nu$. Nine bulk Reynolds numbers were examined, based on the inlet bulk velocity of the smooth pipe (U_∞). These corresponded to $Re = 1.58 \times 10^5$ ($Re_\tau = 7144$), 7.5×10^4 (3635), 5.0×10^4 (2525), 4.0×10^4 (2053), 2.5×10^4 (1399), 2.0×10^4 (1149), 1.0×10^4 (630), 7.5×10^3 (492), and 5.0×10^3 (343).

The Standard $k-\varepsilon$ turbulence model (Launder and Spalding, 1983) was used in OpenFOAM to simulate the flow. OpenFOAM is a finite-volume method open-source solver (Versteeg and Malalasekera, 2007), which has been extensively validated for simulating turbulent pipe flow, e.g., Goswami and Hemmati (2021) and Goswami and Hemmati (2020).

Second-order accurate discretization schemes were utilized for discretizing both advection and diffusion terms. The convergence criterion for root-mean-square (rms) of momentum residuals was set below 10^{-5}. The discretized equations were solved using a steady-state solver based on *Semi-Implicit-Pressure-Linked-Equation* (SIMPLE) (Greenshields, 2015) algorithm. According to past studies, the Standard $k-\varepsilon$ turbulence model presented better performance compared to Realizable $k-\varepsilon$, SST $k-\omega$, and $k-\omega$ in simulating such flows (Morrison et al., 1993; Shah et al., 2012). It was also shown to provide accurate predictions for the mean flow, which were in good agreement with experimental studies, especially at high Re (Goswami and Hemmati, 2020). Simulations were completed using Compute Canada clusters (Cedar and Béluga) with 40 parallel CPUs and 160 GB of memory over an average of 96 simulation hours.

5.4 Validation and Verification

The simulations are first verified through an assessment of their accuracy in terms of validation with available experimental results of Smits et al. (2019) and Zagarola et al. (1996). Verification included comprehensive grid and domain size sensitivity analyses to obtain an optimum spatial grid and domain setup, details of which are provided in Chapter 4. A brief description of the verification studies are provided here for completion. Please note that the results were normalized based on the pipe diameter and radius ($D = 2R$), maximum fully-developed mean velocity (i.e., the bulk velocity, U_b), inlet bulk velocity (U_∞), and the upstream friction velocity (u_τ).

The impacts of domain size on numerical results were investigated by adjusting the distance of outlet boundary from the pipe-insert segment. Three cases were considered with axial domain lengths of $59D$ (Domain 1), $69D$ (Domain 2), and $89D$ (Domain 3), details of which are shown in Table 5.1. The profiles of mean axial velocity and turbulence kinetic energy along the pipe centerline revealed that the simulations in Domain 3 has an adequate

Table 5.1: Spatial grid distribution details based on Case III. r^+, $\Delta\theta^+$, and Δx^+ resemble spacing in the radial, circumferential, and axial directions in wall units based on inflow parameters, respectively. L_{pipe} denotes the total length of the pipe.

Study	L_{pipe}	First Cell (r^+)	$\Delta\theta^+$	Δx^+	Number of Cells
Domain 1	$59D$	4	95	98	11.80×10^6
Domain 2	$69D$	4	95	98	11.94×10^6
Domain 3	$89D$	4	95	98	12.20×10^6
Grid 1	$89D$	16	110	98	6.70×10^6
Grid 2	$89D$	4	95	165	8.95×10^6
Grid 3	$89D$	4	95	127	10.37×10^6
Grid 4	$89D$	4	95	98	12.20×10^6
Grid 5	$89D$	2	94	98	14.49×10^6

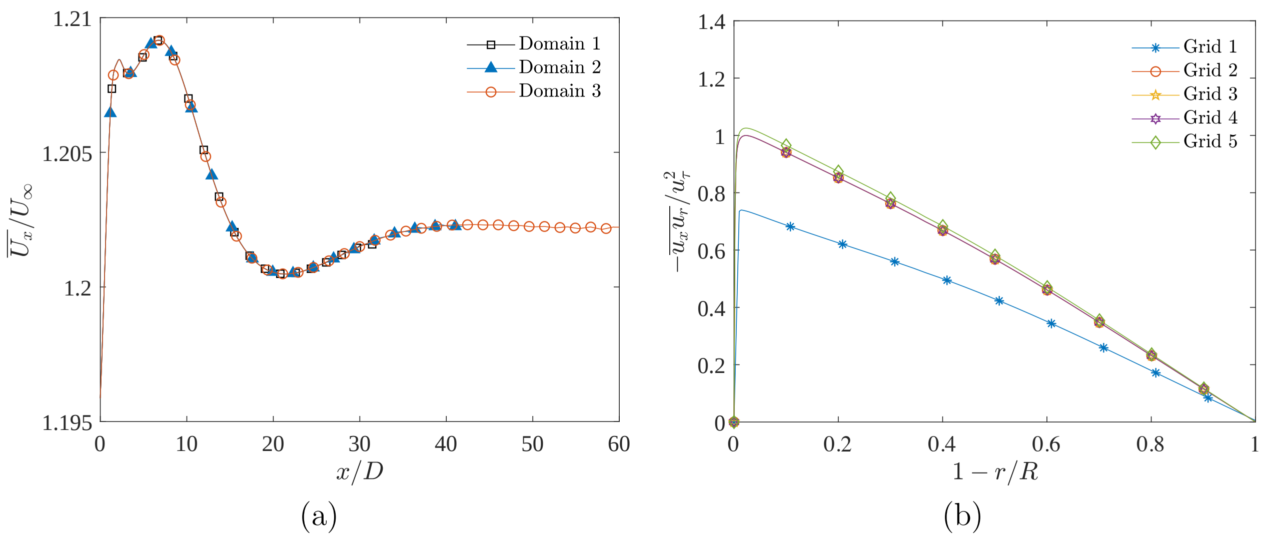

Figure 5.3: Effect of (a) domain size and (b) grid refinement on flow field predictions.

axial extent to accurately predict perturbed turbulent pipe flow recovery at $Re = 1.58 \times 10^5$. There existed a minimal difference of less than 1% between these cases (see Figure 5.3(a)), which implied that the outlet boundary condition had a negligible effect on simulating the critical flow region ahead of the pipe-insert. Hence, Domain 3 was employed for all the simulations.

The grid sensitivity analysis was completed by successively refining the hexahedral grid distribution in all direction through five grids, details of which are also outlined in Table 5.1. The results in Figure 5.3(b), and others not shown here for brevity, revealed a difference of less than 3% between Grid 4 and Grid 5 for the mean velocity field and the Reynolds shear stress profiles. Hence, it was apparent that Grid 4 was sufficient in predicting both the mean flow features and the turbulent field in the current study. Details of these results are provided in Chapter 4.

5.4.1 Validation of Turbulence Model

The accuracy of numerical simulations in capturing the flow profile is validated using a radial comparison of the mean velocity with experiments. First, the performance of various turbulence models (i.e., Standard $k-\varepsilon$, Realizable $k-\varepsilon$ and SST $k-\omega$) in capturing the main flow features was investigated and compared with experiments at $Re = 1.58 \times 10^5$, which are not shown here for brevity. The Standard $k-\varepsilon$ turbulence model presented a better agreement with experimental data. The fully-developed turbulent pipe flow in a smooth pipe with a length of $220D$ is simulated at $Re = 1.58 \times 10^5$, 1.0×10^4, and 5.0×10^3. The mean axial velocity profiles showed a close agreement with experiments of Smits et al. (2019) and Zagarola et al. (1996) in both near the wall and core regions of the flow. The maximum mean centerline velocity difference was within 3% of the experimental data. Moreover, there was a good agreement with experiments at lower Re of 5.0×10^3 and 1.0×10^4 based on the experiments of Kühnen et al. (2018), Eggels et al. (1994), and Den Toonder and Nieuwstadt (1997). The maximum difference between these data was within 5% of the experimental data. These series of validation studies confirmed that the current numerical setup is sufficiently accurate in predicting the main flow features. This conclusion is consistent with previous findings related to the accuracy of numerical simulations, and particularly the Standard $k-\varepsilon$ turbulence model (Shah et al., 2012; Cappelli and Mansour, 2013; Yamagata et al., 2014; Goswami and Hemmati, 2020).

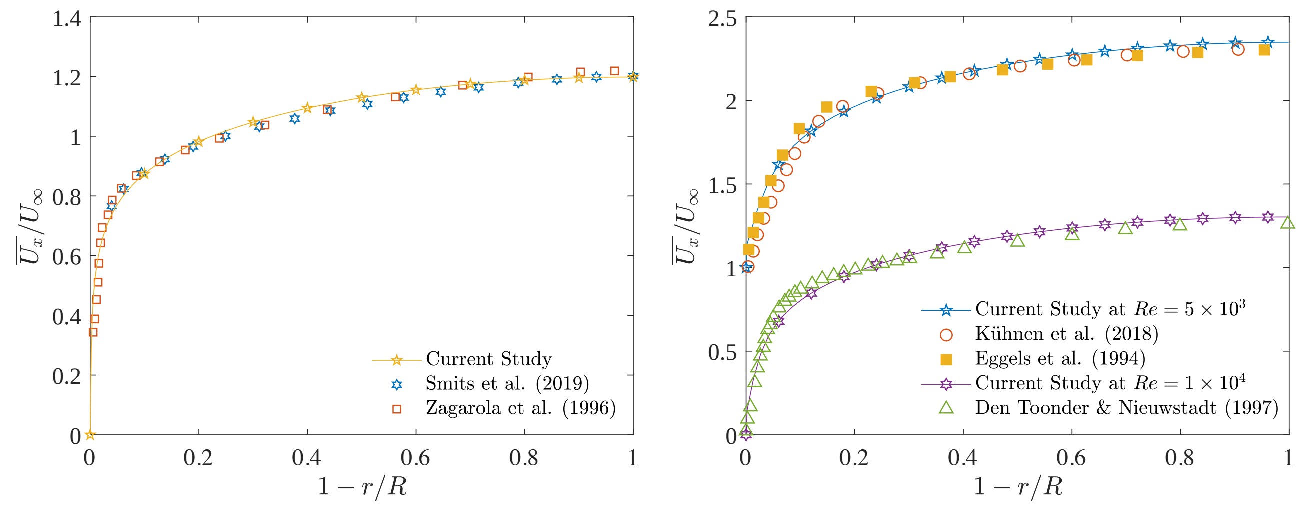

(a) (b)

Figure 5.4: Comparing the mean axial velocity from simulations with experimental results at (a) $Re = 1.58 \times 10^5$, and (b) $Re = 5 \times 10^3$ and 1×10^4, where the data corresponding to $Re = 5 \times 10^3$ was shifted by 1 non-dimensional unit in the vertical direction.

5.5 Results and Discussion

We begin by looking at the radial profiles of mean axial velocity for Case III at different streamwise (axial) locations at $Re = 1.58 \times 10^5$. The mean axial velocity profiles in Figures 5.5(a) and 5.5(b) are normalized by the friction velocity (u_τ) and bulk velocity (U_b), respectively. Here, $r^+ = ru_\tau/\nu$ represents the wall-normal distance. The friction velocity (u_τ) was calculated for the smooth-pipe at the same bulk Reynolds number. Immediately downstream of the perturbation, that is $x = 2D - 8D$, the mean streamwise velocity increased near the wall and the flow decelerated near the outer region at $r^+ \approx 10^3$. Close to wall, flow recovery was observed at $x/D = 8$, at which the mean velocity profile approached the fully-relaxed state by "pivoting" (Van Buren et al., 2020) about a middle point at a distance of $\approx 0.5R$ ($r^+ \approx 5.5 \times 10^2$). This was consistent with the observations of Van Buren et al. (2020), who attributed this to a balance of velocity deficit in pipe flows. Figure 5.5(b) shows the mean axial velocity profile ($\overline{U_x}/U_b$) along the wake centerline. The contraction within the pipe insert accelerates the mean axial flow, which is apparent from the profiles for the entire range of Reynolds numbers considered here. A close inspection of the velocity profile for

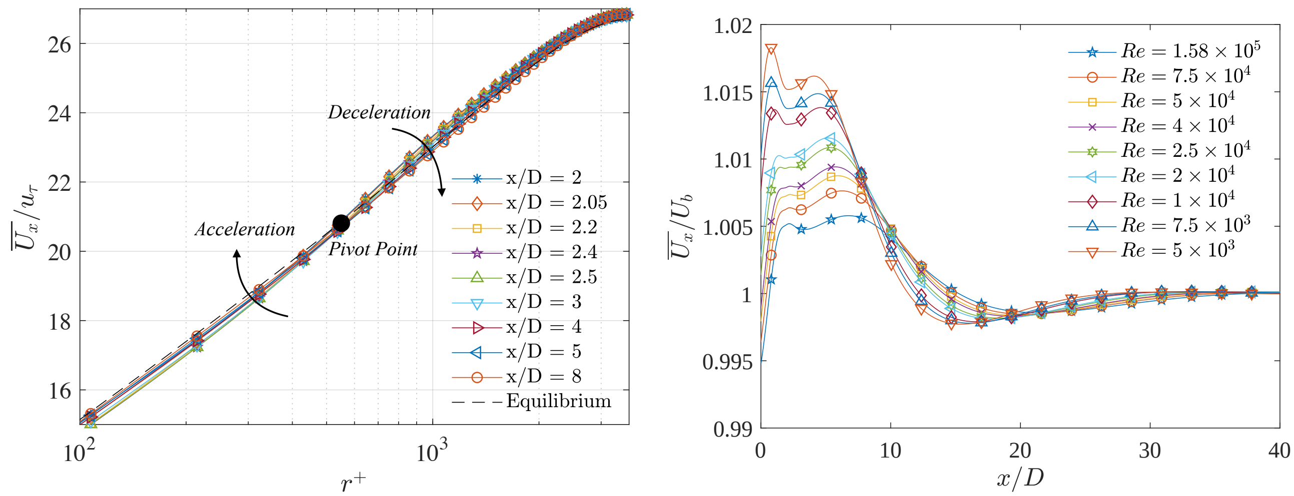

(a) (b)

Figure 5.5: Mean streamwise velocity profile development in (a) spanwise radial direction, and (b) along the wake centerline.

$Re = 1.58 \times 10^5$ revealed two peaks at $x/D \approx 2.2$ and $x/D \approx 6.8$, respectively. The latter resembled a stronger secondary peak. The accelerated flow persisted for a longer distance ($x/D = 25$) at higher Reynolds numbers, which was then followed by an undershoot below equilibrium at $x/D \approx 15$. The flow appeared to slowly recover past this point, and gradually approach a fully-relaxed state at $x/D \approx 27$. The slow and oscillatory recovery trend hinted at a non-monotonic response of the perturbed flow (Van Buren et al., 2020). Further, At lower Reynolds numbers, magnitude of the two peaks increased, while their axial location moved upstream towards the pipe insert. This implied an earlier recovery and significant Reynolds number effects on flow response. The trend of velocity profiles appeared to be altered at $Re \leq 1.0 \times 10^4$, where magnitude of the first peak was larger compared to the second peak.

The change in peak of $\overline{U_x}/U_b$ in Figure 5.5(b) was further investigated quantitatively by tracing the locations of their maximum value (L_p). The variation of L_p with Reynolds number are shown in Figure 5.6, which revealed that both peaks exhibited a power-law trend in the form of $Re^{4/3}$.

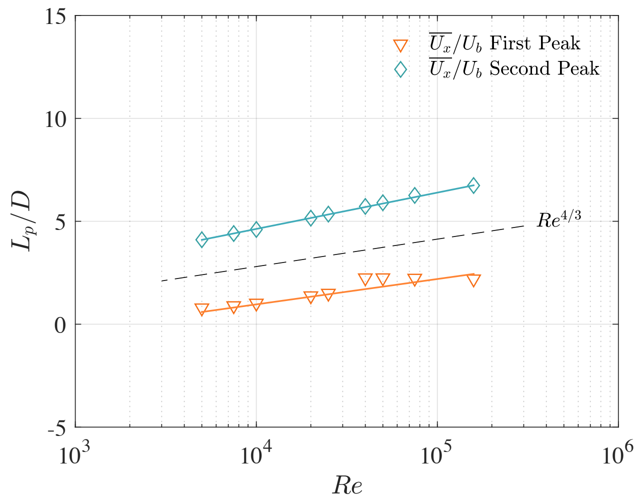

Figure 5.6: Variations of the two-peaks in the initial response of $\overline{U_x}/U_b$ obtained from different Re cases.

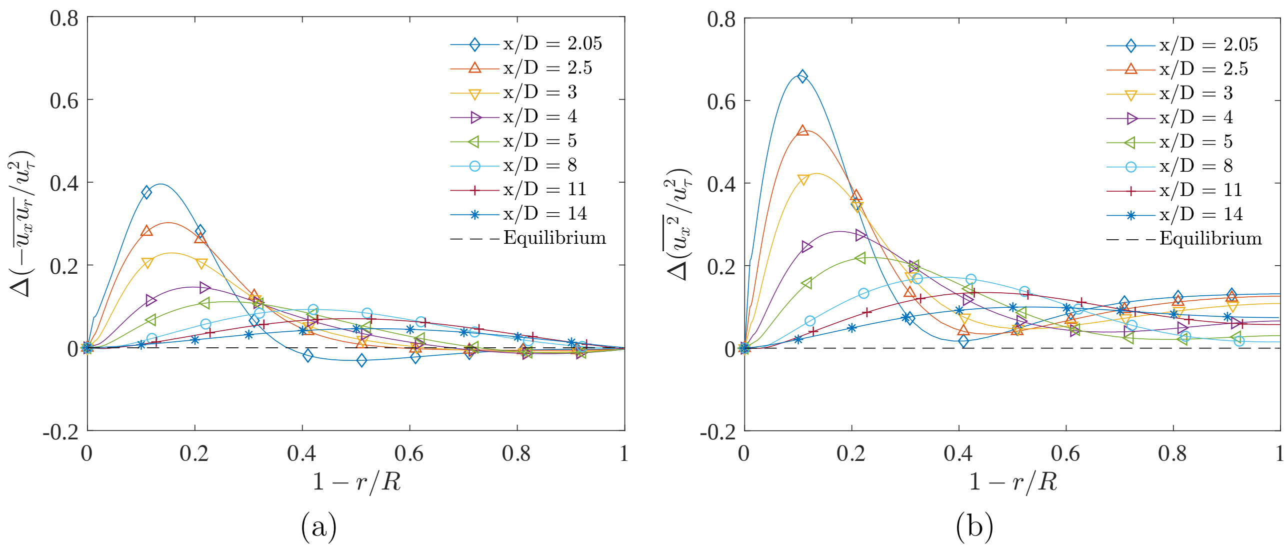

Figure 5.7: Radial profiles of (a) Reynolds shear stress, and (b) normal stress at $Re = 1.58 \times 10^5$.

The immediate turbulent flow response was also examined by looking at the behavior of Reynolds stresses. Figure 5.7 depicts the evolution of Reynolds shear stress $(-\overline{u_x u_r})$ and axial normal stress $(\overline{u_x{}^2})$ with respect to fully-developed flow profiles, where Δ indicates the difference from fully-developed state and r/R represents the non-dimensional radial coordinate. The fully-developed state refers to the conditions far downstream the pipe insert, where no further changes are observed in the flow profiles. Downstream of the pipe insert at

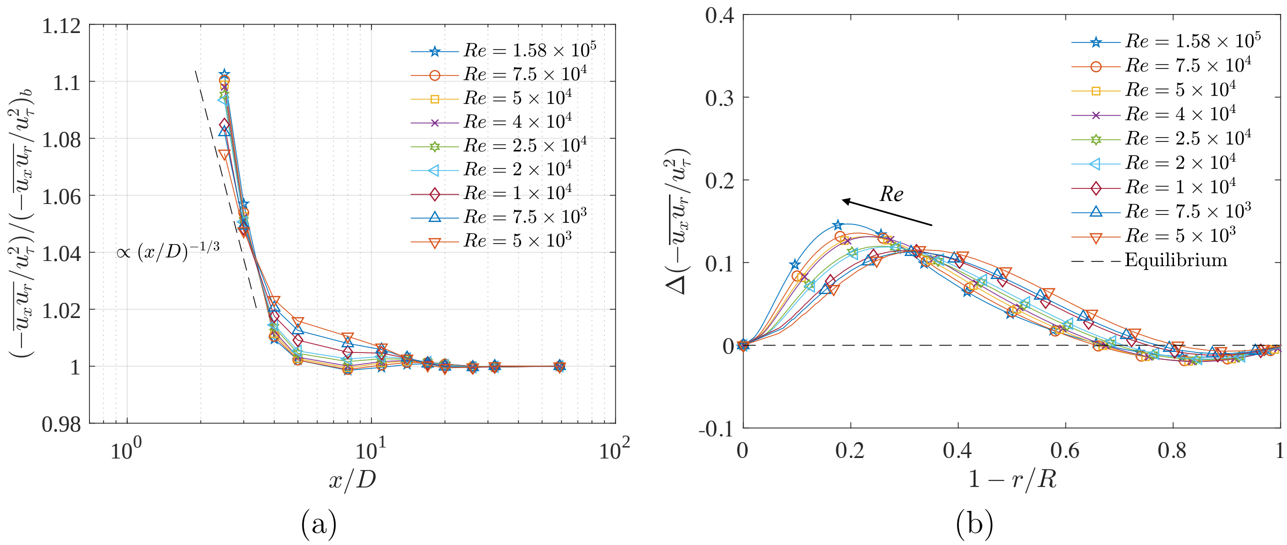

Figure 5.8: (a) The change of maximum $-\overline{u_x u_r}$ in the downstream wake as a function of x/D, and (b) Radial profiles of Reynolds shear stress at $x/D = 4$, for the entire Re range considered.

a distance of $\approx 0.15R$ from the wall, turbulence properties, i.e., $-\overline{u_x u_r}$ and $\overline{u_x}^2$, show a rapid decay and thereby overshot the fully-developed profile. This behavior was consistent with the observations of Van Buren et al. (2020) on pipe flow response to step-change in surface roughness. Further downstream at $x/D = 11$, the turbulence level was observed to remain higher than the fully-developed state. Close to the pipe insert ($x = 2.05D$), however, a peak in $\Delta(-\overline{u_x u_r})$ was observed at $\approx 0.15R$ from the wall, which decayed with increasing axial distance from the pipe insert. The overshoot of $\Delta(-\overline{u_x u_r})$ persisted longer downstream, leading to a longer recovery process that extended beyond $x/D = 14$.

Figure 5.8(a) shows the change in the maximum values of $-\overline{u_x u_r}$ with axial distance downstream of the pipe insert. The decay of $-\overline{u_x u_r}$ within $x = 2.5D - 4D$ indicated a power-law behavior in the form of $(x/D)^{-1/3}$, for all Re cases. The maximum value of $-\overline{u_x u_r}$ at $x/D = 8$ was also compared with that observed in the study of Goswami and Hemmati (2020). The peak in $-\overline{u_x u_r}$ observed here decreased by 22%. It is important to note that since maximum perturbation height in the current study ($0.15D$) was comparable to that taken in Goswami and Hemmati (2020), the difference obtained would be attributed

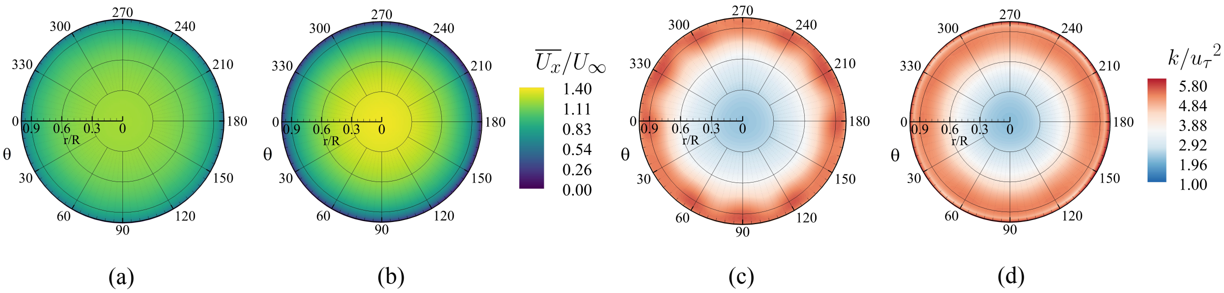

Figure 5.9: Contours of (a, b) the mean streamwise velocity, and (c, d) the turbulence kinetic energy at (a, c) $Re = 1.58 \times 10^5$, (b, d) $Re = 5 \times 10^4$ downstream of the perturbation.

to the smooth bump perturbed geometry for our study, compared to the sharp step taken in Goswami and Hemmati (2020).

A similar response behavior was observed for $\overline{{u_x}^2}$ at $\approx 0.1R$ from the wall, which consisted of a peak. This overshoot remained intact, approaching the central region of the pipe with a slow recovery rate. The overshoot of $\overline{{u_x}^2}$ was not recovered towards equilibrium even at $x/D = 14$. The flow response in the core region also appeared different from the near wall, which is further discussed later with respect to the variation of turbulence kinetic energy and mean velocity. As presented earlier, flow accelerated in the core region to balance continuity due to the flow contraction imposed by the wall perturbation. Thus, mean axial velocity response caused the overshoot of $\overline{{u_x}^2}$ in the core region ($r/R \to 0$) (Van Buren et al., 2020). As shown by Smits et al. (2019), flow approached an equilibrium state when the excess turbulence, close to the wall, moved towards the core region. This trend was also evident in the current study, as depicted by variation of Reynolds stresses in Figure 5.7. Furthermore, Figure 5.8(b) presents the variations of $\Delta(-\overline{u_x u_r})$ with respect to Re, obtained at $x/D = 4$. The peak in $\Delta(-\overline{u_x u_r})$ appeared to move towards the pipe wall with increasing Re. This also highlighted the effect of Re in delaying transport of Reynolds shear stress towards the core region. This also alters the mean velocity on account of mean momentum equation (Van Buren et al., 2020). This was consistent with the delayed recovery trends observed by Smits et al. (2019), Van Buren et al. (2020), and Goswami and Hemmati (2021).

The cross-sectional contour plots for mean axial velocity and turbulent kinetic energy are depicted in Figure 5.9 at $x/D = 3$ for the highest and lowest Re. The contours clearly depict the change in flow dynamics due to Reynolds number effects. At higher Re, the velocity field shows a decreased magnitude in the core region compared to the lower Re case, which was also observed via mean centerline axial velocity profiles presented in Figure 5.5. However, in regions close to the wall ($0.9 < r/R < 1$), a larger velocity deficit is observed for the lower Re case. The contours of turbulence kinetic energy are also presented in Figure 5.9(c, d) for the high and low Reynolds number. For the case of high Re, greater concentration of k/u_τ^2 can be observed in the region close to the wall ($0.8 < r/R < 1$), compared to the low Re case, which is in accordance with the observations made in Figure 5.8(b). This further supports the early transport of Reynolds stress away from the wall and thus achieving a faster recovery at lower Re. The flow contraction within the pipe-insert caused amplification of velocity gradients in regions close to the perturbation, which further led to the increase in Reynolds shear stress. This can be seen in the contour plots of $-\overline{u_x u_r}$ in Figure 5.10, which suggests that the shear stress increases in regions close to the wall at higher Re. In summary, both quantitative and qualitative results discussed above for Reynolds shear and normal stresses depicted similar response characteristics, while possessing different rates of recovery. This hints at differences in the variations of turbulence energy budget terms in responding to the pipe perturbations.

Figure 5.11 traces the evolution of turbulence production (P_k) and dissipation (ε) along the pipe centerline. The production term defined as,

$$P_k \equiv -\overline{u_i u_j}\frac{\partial \overline{U_i}}{\partial x_j},$$

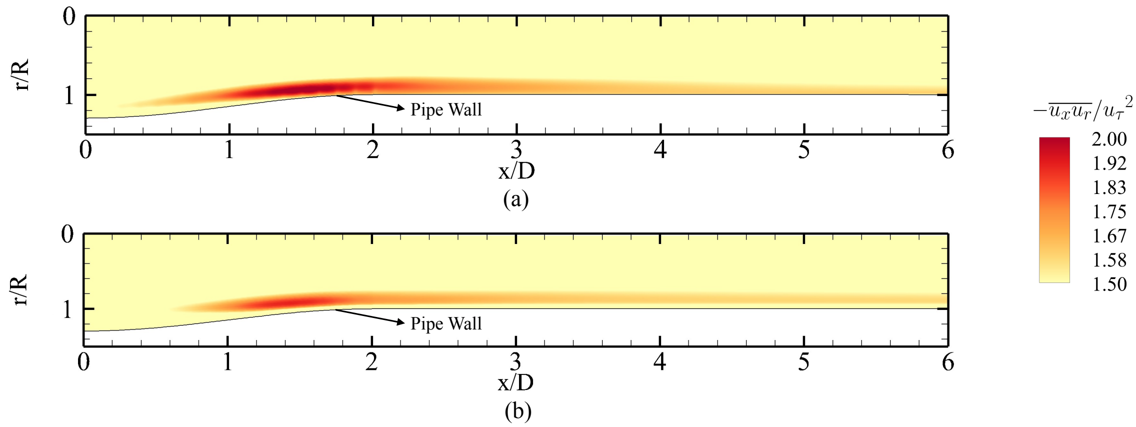

Figure 5.10: Reynolds shear stress contours at (a) $Re = 1.58 \times 10^5$, and (b) $Re = 5 \times 10^4$ in the downstream wake.

was normalized by the friction velocity (u_τ) and pipe diameter (D) (Pope, 2001; Walters et al., 2013). The dissipation rate, defined as,

$$\varepsilon = 2\nu\overline{s_{ij}s_{ij}} = {C_\mu}^{0.75}\frac{k^{1.5}}{l} \qquad \text{where} \qquad \overline{s_{ij}} = \frac{1}{2}(\frac{\partial\overline{U_i}}{\partial x_j} + \frac{\partial\overline{U_j}}{\partial x_i}),$$

was normalized using its value at the farthest downstream location, representing the fully-relaxed state (Greenshields, 2015; Pope, 2001). Close to the pipe insert ($-2 \leq x/D \leq 2$), an initial amplification of P_k was observed with a peak around $x/D \approx -0.5$. This peak was followed by a sharp decay and an overshoot around $x/D \approx 1.8$. Downstream of $x/D \approx 2$, the flow eventually recovered to a fully-developed state. The secondary peak along the wake centerline suggested that P_k decreased during the recovery relaxation process. This second-order flow response was also observed previously by Smits et al. (1979) and Smits et al. (2019). The former study observed that the second-order response was responsible for the initial intensification of Reynolds stresses, followed by a rapid decay, which was previously observed and discussed with respect to Figure 5.7. At lower Reynolds numbers, the magnitude of turbulence kinetic energy production increased at the center of the pipe insert on account of the flow contraction and thereby larger velocity gradients. The variation of turbulent dissipation rate in Figure 5.11(b) implied that the dissipative nature of the wake

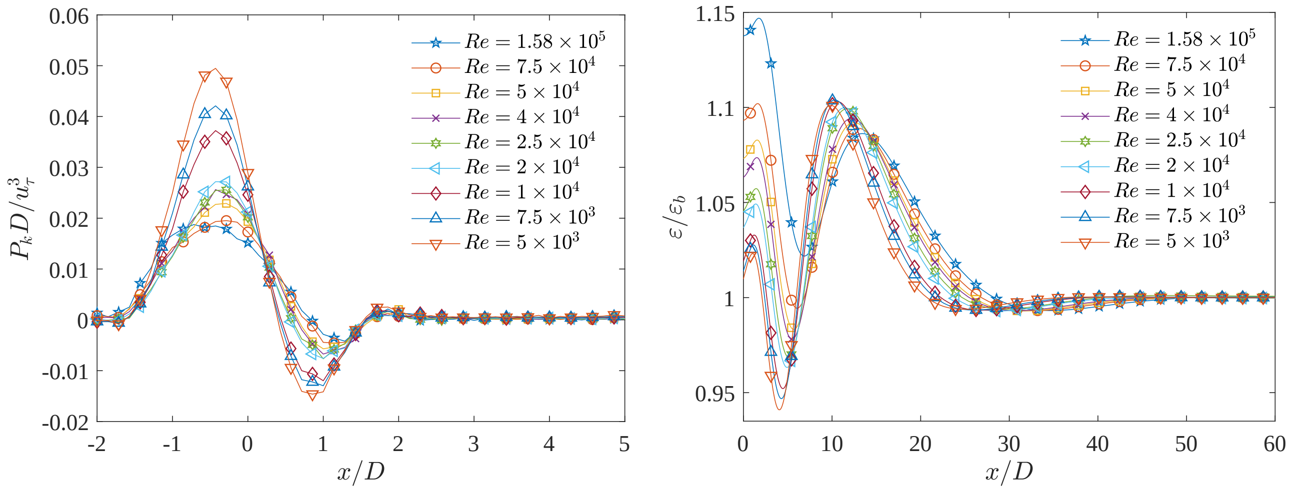

(a) (b)

Figure 5.11: Turbulence kinetic energy production (a) and dissipation (b) along the wake centerline.

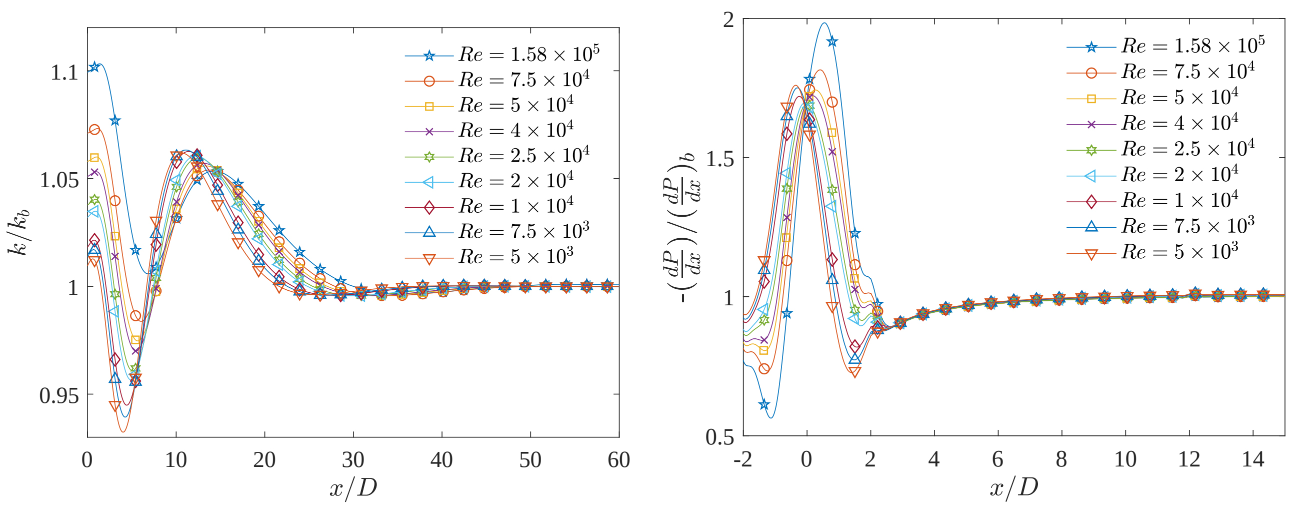

(a) (b)

Figure 5.12: Axial evolution of (a) turbulence kinetic energy, and (b) the axial pressure gradient along the pipe centerline normalized by their corresponding fully-developed state.

immediately following the pipe insert led to the collapse of velocity gradients towards their fully-developed state. Again at lower Reynolds numbers, the maximum dissipation rate moved upstream towards the pipe insert.

The evolution of time-averaged turbulence kinetic energy and axial (streamwise) gradient of pressure (dp/dx) along the centerline are shown in Figure 5.12. Here, both variables are normalized by their value at $x/D = 60$, where a fully-relaxed state was achieved. The mean turbulence kinetic energy showed small oscillations that persisted up to $x/D = 30$, hinting at a long-lasting and oscillatory recovery. These oscillations also showed resemblance to a second-order response previously observed by Van Buren et al. (2020) for pipe flow with a step-change in roughness resulting in an oscillatory response of turbulence kinetic energy. At lower Re, the peak shifted closer towards the pipe insert. In addition, the large pressure gradient existed for a short region inside the pipe insert ($-2 \leq x/D \leq 2$) compared to the values achieved in a fully-developed state. However, this quantity showed a relatively fast recovery, that is within $14D$. This implied that velocity variations dominated the recovery process compared to pressure variations. As expected, in combination with previous observations, the lower Reynolds number led to a smaller pressure gradient.

Flow recovery can be best quantified by locating the axial position where the flow profiles appear to approach an equilibrium state, i.e., fully-developed conditions. To this end, an asymptotic flow behavior was assumed if the consecutive variations in flow gradients in the axial (streamwise) direction were less than 5%. A quantitative comparison of the normalized recovery location (L_r/D) over the range of Reynolds numbers is shown in Figure 5.13. These recovery locations were obtained based on the axial (streamwise) gradient of peak mean velocity ($\overline{U_x}/u_\tau$) and turbulence kinetic energy (k/u_τ^2) downstream of the pipe insert. These results indicated that increasing the bulk Reynolds number delayed the mean flow recovery, thereby leading to a longer recovery length. The asymptotic trend was observed at $Re \geq 7.5 \times 10^4$ in Figure 5.13(a), where the variations in flow recovery length was within $\sim 3\%$ of the highest Reynolds number. Furthermore, the mean flow appeared to recover faster than the turbulent field, which implied that the turbulence field was responsible for the prolonged recovery process and the overall recovery trend. At higher Reynolds numbers, the recovery process was slower. The results in Figure 5.13(b), specifically, revealed that the flow recovery length scaled with Re^4 for both mean and turbulent fields. Previous studies had mainly focused on the recovery of the flow over a square roughness element using the same approach. Goswami and Hemmati (2020) studied the recovery by tracing the transport of

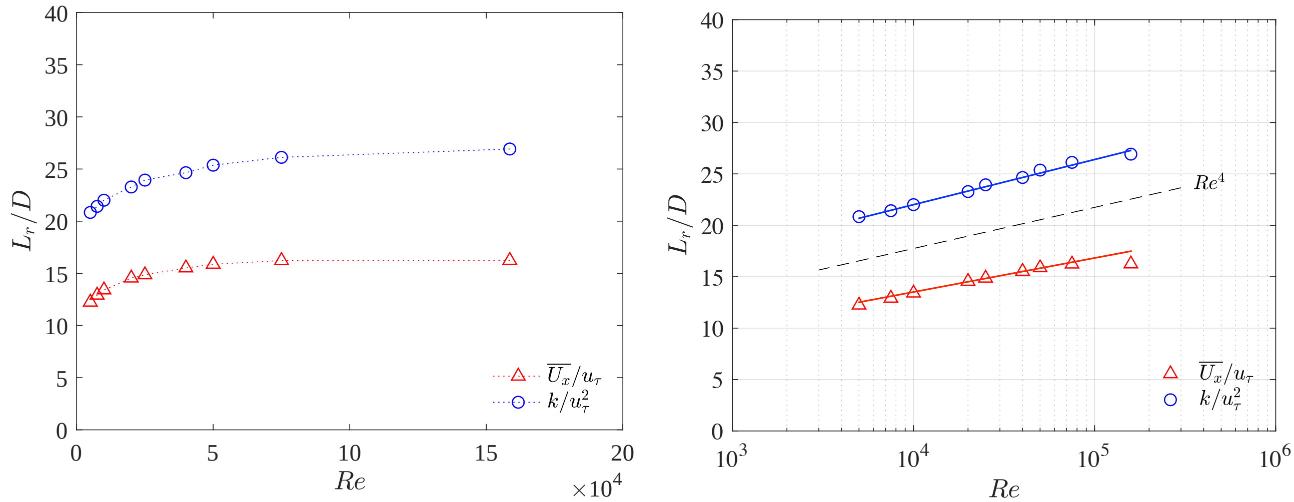

Figure 5.13: Variation of the recovery length at a range of Reynolds number for Case III in (a) linear, and (b) semi-log plotting style.

turbulence quantities (i.e., Reynolds shear stress) in the flow, based on which they observed a prolonged recovery.

Radial profiles of mean axial (streamwise) velocity gradients ($\partial\overline{U_x}/\partial x$) at different axial locations downstream of the perturbation are shown in Figure 5.14(a) for the case of $Re = 1.58 \times 10^5$. Larger velocity gradients were observed near the wall ($r/R \to 1$), which diminished and moved towards the center of the pipe ($r/R \to 0$). The larger velocity gradients near the pipe insert ($x = 2D - 8D$) coincided with the peaks in Reynolds stresses that were observed previously in Figure 5.7. Further, as the flow developed downstream, a self-similarity in terms of near-zero velocity gradient was observed. This was in agreement with the findings of Smits et al. (2019), who attributed the overshoot of velocity gradients to the contraction of flow produced by the square roughness element. The abrupt collapse of the gradients toward the pipe center was also consistent with their observations, and that of Goswami and Hemmati (2020). The slow recovery of $\partial\overline{U_x}/\partial x$ towards the pipe center therefore depicted a long recovery process. The axial profile of velocity gradients along the pipe centerline at a range of Reynolds numbers are shown in Figure 5.14(b). With increasing Re, a reduction in the magnitude of $\partial\overline{U_x}/\partial x$ was clearly observed.

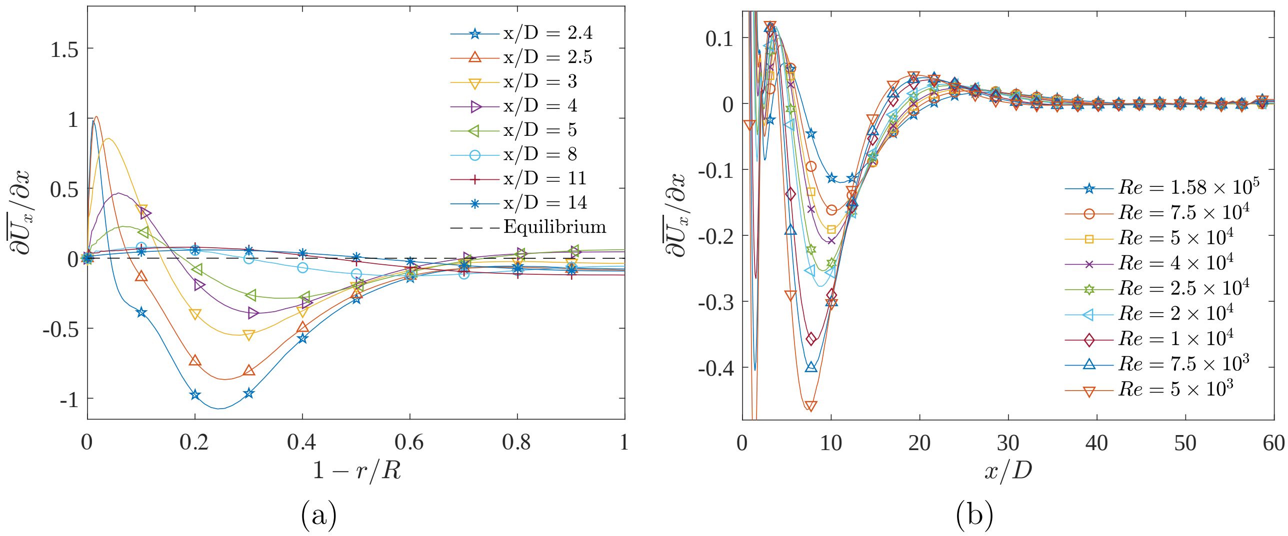

Figure 5.14: Profiles of the mean axial (streamwise) velocity gradients along (a) the pipe radius at $Re = 1.58 \times 10^5$, (b) the pipe centerline at a range of Re, both for Case III.

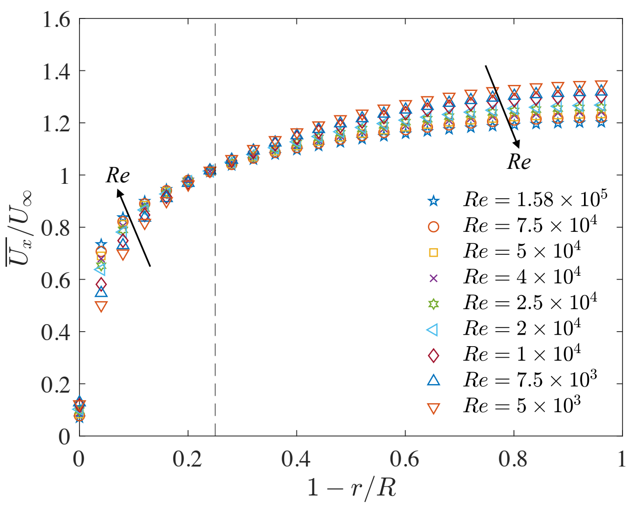

Figure 5.15: Fully recovered and fully-developed mean velocity profiles normalized by the inlet bulk velocity (U_∞).

Radial profiles of fully-developed mean velocities at $x/D = 60$ are compared for the entire range of Reynolds numbers in Figure 5.15. With increasing the Reynolds number, mean velocity decelerated near the pipe center, while it accelerated near the wall. This may be attributed to the effect of turbulence on transporting higher-momentum fluid towards the walls, as previously suggested by Malin (1997). At a distance of $\approx 0.25R$ from the wall, the bulk velocity approached the mean velocity with the corresponding location remaining independent of the Reynolds number. This observation was consistent with those of Zagarola and Smits (1998) and Furuichi et al. (2015), who developed an outer flow scaling law (see Chapter 3.5), based on which the point where mean velocity approaches bulk velocity was found to be a function of wall-normal distance (r/R).

This chapter only focused on thoroughly analyzing turbulent pipe flow response to wall geometry of Case III at a range of Reynolds number. However, the flow variations in Case I and Case II show very similar behaviors with respect to Reynolds number, although their individual flow dynamics differ substantially. These were not shown here for brevity. The effect of pipe insert shape, meaning the azimuthal Fourier modes, on the flow dynamics and response was presented in Chapter 4.

5.6 Conclusions

The response and recovery behavior of turbulent flow in a perturbed pipe were numerically analyzed at a range of Reynolds numbers between 5×10^3 and 1.58×10^5. The perturbation targeted specific Fourier modes 3, 15, and 3 + 15, while the Reynolds number effects were mainly discussed in terms of the superimposed shape ($m = 3 + 15$). The immediate flow response revealed that the mean flow accelerated near the wall and decelerated towards the center of the pipe. The mean velocity response in the wake revealed two peaks whose axial locations were observed to follow a power-law trend as $L_p/D \propto Re^{4/3}$. A fast turbulence decay past the pipe insert was also observed, which was consistent with the literature (Van Buren et al., 2020). The maximum Reynolds shear stress in the wake decayed with a power-law trend in the form of $(x/D)^{-1/3}$ for all Reynolds numbers. A long-lasting flow response was observed for the entire range of Reynolds numbers considered here, while the mean flow recovered faster than the turbulent field. The overall recovery length increased with increasing Reynolds number, and it appeared to approach an asymptotic behavior at $Re \geq 7.5 \times 10^4$. The turbulent field resembled a second-order response, similar to a channel flow with a step-change in surface roughness (Saito and Pullin, 2014). Tracking the changes in axial flow gradients within the core region suggested a slower recovery compared to the near wall region. The flow recovery length scaled with Re^4 for both mean velocity and turbulence kinetic energy.

Chapter 6

CONCLUSION

The main objective of this study was to characterization turbulent flow response and recovery over different pipe-inserts ranging from moderate to high Reynolds numbers. In particular, this thesis numerically examined the implications of wall changes that target particular Fourier modes ($m = 3$, 15, and $3 + 15$) on pipe flow response at different Reynolds numbers using RANS-based turbulence models. A thorough validation study was completed to determine the performance of different RANS turbulence models in predicting the mean flow features, such as the mean streamwise velocity profile and Reynolds stress distributions. This includes Standard $k - \varepsilon$, Realizable $k - \varepsilon$, and SST $k - \omega$. The Standard $k - \varepsilon$ turbulence model performed the best overall, implying the closest approximation to the available experimental data, which was also consistent with recent literature.

First, the effect of wall shape on flow dynamics, response, and recovery was examined at a high Reynolds number of 1.58×10^5 for the three Fourier modes. The acceleration of mean axial velocity along the wake centerline appeared at $x = 2D - 7D$ for all three cases due to flow contraction within the middle of the pipe-insert. Cases of $m = 15$ and 3+15 depicted two peaks in the centerline velocity profile, which indicated characteristics of a second-order flow response. Similar to the mean flow, turbulent field response due to these wall modifications was also a second-order feature similar to a channel flow with abrupt variations of surface roughness (Saito and Pullin, 2014). The mean flow properties presented a faster recovery compared to the turbulent field, which was analogous to a turbulent pipe flow response past an abrupt change of wall roughness at high Reynolds numbers (Van Buren et al., 2020). The case of $m = 3$, however, represented a non-oscillatory behavior corresponding to a monotonic response. Specifically, the lower Fourier mode wall shape ($m = 3$) illustrated a faster recovery trend in both mean flow and turbulent features in comparison with the other two cases. The flow disturbance, response, and recovery in the wake of perturbation geometry corresponding to the higher Fourier mode ($m = 15$) dominated when low and high modes were combined ($m = 3 + 15$). This suggested a relatively more dominance of the higher Fourier mode wall modifications on the overall characteristics of the boundary layer structures (Adrian, 2007). Moreover, the investigation of $Q-$criterion delineated flow regions dominated by higher rates of rotation in the wake of pipe-inserts. In addition, localized regions of higher rotations rates in the downstream wake was assumed to be a contributing factor in the concentration of Reynolds stresses to the region closer to the wall. This can be a reason for the prolonged recovery process observed for cases resembling perturbation geometries of higher Fourier modes.

This study was then extended to analyzing the implications of Reynolds number on the flow response and recovery due to the implementation of different pipe inserts. The simulations were performed at a wide range of Reynolds numbers between 5×10^3 and 1.58×10^5. For this part, the analyses focused on the case of m=3+15, which exhibited the most significant response and recovery behavior compared to the other two cases. The immediate flow response showed that the mean flow accelerated in regions closer to the wall and decelerated towards the center of the pipe. The mean velocity response in the wake region consisted of two peaks, whose axial locations were determined to follow a power-law trend in the form of $L_p/D \propto Re^{4/3}$. The turbulence field exhibited a fast decay past the pipe-insert, where the maximum Reynolds shear stress decayed with a power-law trend as $(x/D)^{-1/3}$ for all Reynolds numbers cases. The change axial flow gradients hinted at a slower recovery of the core flow compared to the regions close to the wall. The flow response was found to be long-lasting for the entire range of Reynolds numbers. However, the mean flow recovered faster than the turbulent field. The overall recovery length increased at higher Reynolds numbers, and it resembled the asymptotic behavior at $Re \geq 7.5 \times 10^4$. The flow recovery location was scaled with Re^4 for both mean velocity and turbulence kinetic energy properties.

6.1 Future Work

The findings of this study provide a framework to improve our knowledge and understanding of the out-of-equilibrium wall-bounded turbulent pipe flows. While a significant analysis was presented on the flow response and recovery behavior, some remaining unchallenged questions require further research, including:

(a) The implications of perturbation thickness on the flow response and recovery.

(b) The effect of pipe-insert length on the flow response and recovery.

(c) Analysis of the implications of non-Newtonian fluid features on the response and recovery of these perturbed flow.

(d) Studying the separation distance of inserts with potential pipe-angles on the response and recovery of the flow.

(e) The flow dynamics, response and recovery associated with multiphase pipe flow.

(f) The near-wall turbulence implications of the pipe-inserts, in terms of manipulation of Large-Scale motions and Very-Large-Scale motions using Direct Numerical Simulations at moderate Reynolds numbers.

(g) Examination of the detailed flow fields using Direct Numerical Simulations at different flow conditions (e.g., laminar, transition and turbulence).

(h) Implications of the pipe-inserts on heat transfer in pipe flow.

Bibliography

Adams, E. and Johnston, J. (1988). Effects of the separating shear layer on the reattachment flow structure part 2: Reattachment length and wall shear stress. *Experiments in Fluids*, 6(7):493–499.

Adrian, R. J. (2007). Hairpin vortex organization in wall turbulence. *Physics of Fluids*, 19(4):041301.

Anderson, J. D. (2003). *Modern compressible flow*. Tata McGraw-Hill Education.

Anderson, W., Barros, J. M., Christensen, K. T., and Awasthi, A. (2015). Numerical and experimental study of mechanisms responsible for turbulent secondary flows in boundary layer flows over spanwise heterogeneous roughness. *Journal of Fluid Mechanics*, 768:316–347.

Antonia, R. and Luxton, R. (1971). The response of a turbulent boundary layer to an upstanding step change in surface roughness.

Babu, V. (2008). *Fundamentals of gas dynamics*. Springer.

Bailey, S. C. and Smits, A. J. (2010). Experimental investigation of the structure of large-and very-large-scale motions in turbulent pipe flow. *Journal of Fluid Mechanics*, 651:339.

Balachandar, R. (1990). *Characteristics of separated flows including cavitation effects*. PhD thesis, Concordia University.

Balakumar, B. and Adrian, R. (2007). Large-and very-large-scale motions in channel and boundary-layer flows. *Philosophical Transactions of the Royal Society A: Mathematical, Physical and Engineering Sciences*, 365(1852):665–681.

Baltzer, J., Adrian, R., and Wu, X. (2013). Structural organization of large and very large scales in turbulent pipe flow simulation. *Journal of Fluid Mechanics*, 720:236.

Baskaran, A. and Kashef, A. (1996). Investigation of air flow around buildings using computational fluid dynamics techniques. *Engineering Structures*, 18(11):861–875.

Batchelor, C. K. G. (2000). *An introduction to fluid dynamics*. Cambridge university press.

Bradshaw, P. and Wong, F. (1972). The reattachment and relaxation of a turbulent shear layer. *Journal of Fluid Mechanics*, 52(1):113–135.

Cappelli, D. and Mansour, N. N. (2013). Performance of reynolds averaged navier-stokes models in predicting separated flows: study of the hump flow model problem. In *31st AIAA Applied Aerodynamics Conference*, page 3154.

Chang, Y. S. and Scotti, A. (2004). Modeling unsteady turbulent flows over ripples: Reynolds-averaged navier-stokes equations (rans) versus large-eddy simulation (les). *Journal of Geophysical Research: Oceans*, 109(C9).

Chung, D., Marusic, I., Monty, J. P., Vallikivi, M., and Smits, A. J. (2015). On the universality of inertial energy in the log layer of turbulent boundary layer and pipe flows. *Experiments in Fluids*, 56(7):1–10.

Cui, J., Patel, V. C., and Lin, C.-L. (2003). Large-eddy simulation of turbulent flow in a channel with rib roughness. *International Journal of Heat and Fluid Flow*, 24(3):372–388.

Davidson, L. (2017). Fluid mechanics, turbulent flow and turbulence modeling. *Chalmers University of Technology, Goteborg, Sweden (Nov 2011)*.

Deardorff, J. W. et al. (1970). A numerical study of three-dimensional turbulent channel flow at large reynolds numbers. *J. Fluid Mech*, 41(2):453–480.

Den Toonder, J. and Nieuwstadt, F. (1997). Reynolds number effects in a turbulent pipe flow for low to moderate re. *Physics of Fluids*, 9(11):3398–3409.

Dimaczek, G., Tropea, C., and Wang, A.-B. (1989). Turbulent flow over two-dimensional, surface-mounted obstacles: plane and axisymmetric geometries. In *Advances in Turbulence 2*, pages 114–121. Springer.

Ding, L., Saxton-Fox, T., Hultmark, M., and Smits, A. (2019). Effects of pressure gradients and streamline curvature on the statistics of a turbulent pipe flow. In *11th International Symposium on Turbulence and Shear Flow Phenomena, TSFP 2019*.

Doolan, C. J. and Moreau, D. J. (2016). Flow-induced noise generated by sub-boundary layer steps. *Experimental Thermal and Fluid Science*, 72:47–58.

Durbin, P. A. and Reif, B. P. (2011). *Statistical theory and modeling for turbulent flows*, volume 2. Wiley Online Library.

Durst, F., Founti, M., and Wang, A. (1989). Experimental investigation of the flow through an axisymmetric constriction. In *Turbulent Shear Flows 6*, pages 338–350. Springer.

Durst, F. and Tropea, C. (1983). Flows over two-dimensional backward—facing steps. In *Structure of Complex Turbulent Shear Flow*, pages 41–52. Springer.

Durst, F. and Wang, A. (1989). Experimental and numerical investigations of the axisymmetric, turbulent pipe flow over a wall-mounted thin obstacle. In *7th Symposium on Turbulent Shear Flows, Volume 1*, volume 1, pages 10–4.

Eaton, J. and Johnston, J. (1981). A review of research on subsonic turbulent flow reattachment. *AIAA journal*, 19(9):1093–1100.

Eggels, J., Unger, F., Weiss, M., Westerweel, J., Adrian, R. J., Friedrich, R., and Nieuwstadt, F. (1994). Fully developed turbulent pipe flow: a comparison between direct numerical simulation and experiment. *Journal of Fluid Mechanics*, 268:175–210.

Einstein, H. A. and Li, H. (1958). Secondary currents in straight channels. *Eos, Transactions American Geophysical Union*, 39(6):1085–1088.

Farhadi, M. and Rahnama, M. (2006). Large eddy simulation of separated flow over a wall-mounted cube.

Feng, G., Guo, Y., Shi, D., Gu, C., Yu, F., Long, T., and Sun, S. (2020). Experimental and numerical study of the flow characteristics of a novel olive-shaped flowmeter (osf). *Flow Measurement and Instrumentation*, page 101832.

Fogaing, M. B. T., Hemmati, A., Lange, C. F., and Fleck, B. A. (2019). Performance of turbulence models in simulating wind loads on photovoltaics modules. *Energies*, 12(17):3290.

Furuichi, N., Terao, Y., Wada, Y., and Tsuji, Y. (2015). Friction factor and mean velocity profile for pipe flow at high reynolds numbers. *Physics of Fluids*, 27(9):095108.

George, W. K. (2013). Lectures in turbulence for the 21st century. *Chalmers University of Technology*.

Gessner, F. (1973). The origin of secondary flow in turbulent flow along a corner. *Journal of Fluid Mechanics*, 58(1):1–25.

Good, M. and Joubert, P. (1968). The form drag of two-dimensional bluff-plates immersed in turbulent boundary layers. *Journal of Fluid Mechanics*, 31(3):547–582.

Goswami, S. and Hemmati, A. (2020). Response of turbulent pipeflow to multiple square bar roughness elements at high reynolds number. *Physics of Fluids*, 32(7):075110.

Goswami, S. and Hemmati, A. (2021). Evolution of turbulent pipe flow recovery over a square bar roughness element at a range of reynolds numbers. *Physics of Fluids*, 33(3):035113.

Greenshields, C. J. (2015). Openfoam-the open source cfd toolbox-user guide. *OpenFOAM Foundation Ltd*, 2(0).

Guala, M., Hommema, S., and Adrian, R. (2006). Large-scale and very-large-scale motions in turbulent pipe flow. *Journal of Fluid Mechanics*, 554:521.

Gursul, I., Cleaver, D., and Wang, Z. (2014). Control of low reynolds number flows by means of fluid–structure interactions. *Progress in Aerospace Sciences*, 64:17–55.

Haroutunian, V. and Engelman, M. S. (1991). On modeling wall-bound turbulent flows using specialized near-wall finite elements and the standard k-epsilon turbulence model. *Advances in Numerical Simulation of Turbulent Flows*, pages 97–105.

Hatoum, H., Mo, X.-M., Crestanello, J. A., and Dasi, L. P. (2019). Modeling of the instantaneous transvalvular pressure gradient in aortic stenosis. *Annals of biomedical engineering*, 47(8):1748–1763.

Hellström, L. H., Marusic, I., and Smits, A. J. (2016). Self-similarity of the large-scale motions in turbulent pipe flow. *Journal of Fluid Mechanics*, 792.

Hellström, L. H. and Smits, A. J. (2014). The energetic motions in turbulent pipe flow. *Physics of Fluids*, 26(12):125102.

Hemmati, A. (2016). Evolution of large-scale structures in the wake of sharp-edge thin flat bodies.

Hemmati, A., Wood, D. H., and Martinuzzi, R. J. (2018). On simulating the flow past a normal thin flat plate. *Journal of Wind Engineering and Industrial Aerodynamics*, 174:170–187.

Hoffmann, P., Muck, K., and Bradshaw, P. (1985). The effect of concave surface curvature on turbulent boundary layers. *Journal of Fluid mechanics*, 161:371–403.

Hucho, W. and Sovran, G. (1993). Aerodynamics of road vehicles. *Annual review of fluid mechanics*, 25(1):485–537.

Hultmark, M., Bailey, S. C., and Smits, A. J. (2010). Scaling of near-wall turbulence in pipe flow. *Journal of Fluid Mechanics*, 649:103.

Hultmark, M., Vallikivi, M., Bailey, S. C. C., and Smits, A. (2012). Turbulent pipe flow at extreme reynolds numbers. *Physical review letters*, 108(9):094501.

Hultmark, M., Vallikivi, M., Bailey, S. C. C., and Smits, A. (2013). Logarithmic scaling of turbulence in smooth-and rough-wall pipe flow. *Journal of Fluid Mechanics*, 728:376.

Ilman, M. et al. (2014). Analysis of internal corrosion in subsea oil pipeline. *case studies in Engineering Failure Analysis*, 2(1):1–8.

Ji, M. and Wang, M. (2010). Sound generation by turbulent boundary-layer flow over small steps. *Journal of Fluid Mechanics*, 654:161.

Jiménez, J. (1998). The largest scales of turbulent wall flows. *CTR Annual Research Briefs*, 137:54.

Jiménez, J. (2004). Turbulent flows over rough walls. *Annu. Rev. Fluid Mech.*, 36:173–196.

Joshi, J. and Nayak, A. K. (2019). *Advances of computational fluid Dynamics in nuclear reactor design and safety assessment*. Woodhead Publishing.

Jovic, S. and Driver, D. (1995). Reynolds number effect on the skin friction in separated flows behind a backward-facing step. *Experiments in Fluids*, 18(6):464–467.

Kaneda, M., Yu, B., Ozoe, H., and Churchill, S. W. (2003). The characteristics of turbulent flow and convection in concentric circular annuli. part i: flow. *International Journal of Heat and Mass Transfer*, 46(26):5045–5057.

Katz, J. (2006). Aerodynamics of race cars. *Annu. Rev. Fluid Mech.*, 38:27–63.

Kim, J., Kline, S., and Johnston, J. (1980). Investigation of a reattaching turbulent shear layer: flow over a backward-facing step.

Kim, K. and Adrian, R. (1999). Very large-scale motion in the outer layer. *Physics of Fluids*, 11(2):417–422.

Kim, T., Kato, S., and Murakami, S. (2001). Indoor cooling/heating load analysis based on coupled simulation of convection, radiation and hvac control. *Building and Environment*, 36(7):901–908.

Kiya, M. and Sasaki, K. (1983). Structure of a turbulent separation bubble. *Journal of Fluid Mechanics*, 137:83–113.

Kolmogorov, A. N. (1941). Equations of turbulent motion in an incompressible fluid. In *Dokl. Akad. Nauk SSSR*, volume 30, pages 299–303.

Kuethe, A. M. (1976). Foundations of aerodynamics: bases of aerodynamic design. *University of Michigan, USA, John Wiley & Sons, New York, Printed in the USA, ISBN: 0-471-50953-1.*

Kühnen, J., Song, B., Scarselli, D., Budanur, N. B., Riedl, M., Willis, A. P., Avila, M., and Hof, B. (2018). Destabilizing turbulence in pipe flow. *Nature physics*, 14(4):386–390.

Landahl, M. T., Mollo-Christensen, E., and Korman, M. S. (1989). Turbulence and random processes in fluid mechanics.

Launder, B. E. and Spalding, D. B. (1983). The numerical computation of turbulent flows. In *Numerical prediction of flow, heat transfer, turbulence and combustion*, pages 96–116. Elsevier.

Leonardi, S. and Castro, I. P. (2010). Channel flow over large cube roughness: a direct numerical simulation study. *Journal of Fluid Mechanics*, 651:519–539.

Leonardi, S., Orlandi, P., Smalley, R., Djenidi, L., and Antonia, R. (2003). Direct numerical simulations of turbulent channel flow with transverse square bars on one wall. *Journal of Fluid Mechanics*, 491:229.

Li, M., De Silva, C. M., Rouhi, A., Baidya, R., Chung, D., Marusic, I., and Hutchins, N. (2019). Recovery of wall-shear stress to equilibrium flow conditions after a rough-to-smooth step change in turbulent boundary layers. *Journal of Fluid Mechanics*, 872:472–491.

Liu, F. (2016). A thorough description of how wall functions are implemented in openfoam. *Proceedings of CFD with OpenSource Software*, pages 1–33.

Liu, Y., Li, J., and Smits, A. J. (2019). Roughness effects in laminar channel flow. *Journal of Fluid Mechanics*, 876:1129–1145.

Malin, M. (1997). Turbulent pipe flow of power-law fluids. *International communications in heat and mass transfer*, 24(7):977–988.

Martinuzzi, R. and Tropea, C. (1993). The flow around surface-mounted, prismatic obstacles placed in a fully developed channel flow (data bank contribution).

Martinuzzi, R. J. and Havel, B. (2000). Turbulent flow around two interfering surface-mounted cubic obstacles in tandem arrangement. *J. Fluids Eng.*, 122(1):24–31.

McKeon, B., Swanson, C., Zagarola, M., Donnelly, R., and SMITS, A. J. (2004). Friction factors for smooth pipe flow. *Journal of Fluid Mechanics*, 511:41.

Mendes, P. S., Braga, A., Azevedo, L., and Correa, K. (1999). Resistive force of wax deposits during pigging operations.

Menter, F. (1993). Zonal two equation kw turbulence models for aerodynamic flows. In *23rd fluid dynamics, plasmadynamics, and lasers conference*, page 2906.

Menter, F. and Esch, T. (2001). Elements of industrial heat transfer predictions. In *16th Brazilian Congress of Mechanical Engineering (COBEM)*, volume 109, page 650.

Milne-Thomson, L. M. (1973). *Theoretical aerodynamics*. Courier Corporation.

Mollicone, J.-P., Battista, F., Gualtieri, P., and Casciola, C. M. (2017). Effect of geometry and reynolds number on the turbulent separated flow behind a bulge in a channel. *Journal of Fluid Mechanics*, 823:100–133.

Morrison, G. L., Deotte Jr, R. E., Nail, G. H., and Panak, D. L. (1993). Mean velocity and turbulence fields inside a β= 0.50 orifice flowmeter. *AIChE journal*, 39(5):745–756.

Muñoz, J. A., Ancheyta, J., and Castañeda, L. C. (2016). Required viscosity values to ensure proper transportation of crude oil by pipeline. *Energy & Fuels*, 30(11):8850–8854.

Muck, K., Hoffmann, P., and Bradshaw, P. (1985). The effect of convex surface curvature on turbulent boundary layers. *Journal of Fluid Mechanics*, 161:347–369.

Nesic, S. and Postlethwaite, J. (1990). Relationship between the structure of disturbed flow and erosion—corrosion. *Corrosion*, 46(11):874–880.

Nygård, F. and Andersson, H. (2013). Numerical simulation of turbulent pipe flow through an abrupt axisymmetric constriction. *Flow, turbulence and combustion*, 91(1):1–18.

OpenCFD, O. (2019). The open source computational fluid dynamics (cfd) toolbox.

Paterson, D. and Apelt, C. (1989). Simulation of wind flow around three-dimensional buildings. *Building and Environment*, 24(1):39–50.

Perić, M. and Tropea, C. (1993). Turbulent flow over surface-mounted obstacles in plane and axisymmetric geometries. In *Physics of Separated Flows—Numerical, Experimental, and Theoretical Aspects*, pages 18–26. Springer.

Perkins, H. (1970). The formation of streamwise vorticity in turbulent flow. *Journal of Fluid Mechanics*, 44(4):721–740.

Pope, S. B. (2001). Turbulent flows.

Prandtl, L. (1953). Essentials of fluid dynamics: with applications to hydraulics, aeronautics, meteorology and other subjets.

Ravindran, S. (1999). *Active control of flow separation over an airfoil*, volume 209838. Citeseer.

Roache, P. J. (1982). Scaling of high-reynolds-number weakly separated channel flows. In *Numerical and Physical Aspects of Aerodynamic Flows*, pages 87–98. Springer.

Rumsey, C., Gatski, T., Sellers, W., Vatsa, V., and Viken, S. (2004). Summary of the 2004 cfd validation workshop on synthetic jets and turbulent separation control. In *2nd AIAA Flow Control Conference*, page 2217.

Saffman, P. and Wilcox, D. (1974). Turbulence-model predictions for turbulent boundary layers. *AIAA journal*, 12(4):541–546.

Saffman, P. G. (1970). A model for inhomogeneous turbulent flow. *Proceedings of the Royal Society of London. A. Mathematical and Physical Sciences*, 317(1530):417–433.

Saito, N. and Pullin, D. (2014). Large eddy simulation of smooth–rough–smooth transitions in turbulent channel flows. *International Journal of Heat and Mass Transfer*, 78:707–720.

Schlichting, H. and Gersten, K. (2016). *Boundary-layer theory*. Springer.

Schofield, W. and Logan, E. (1990). Turbulent shear flow over surface mounted obstacles.

Senturk, U. and Smits, A. J. (2019). Roughness effects in laminar pipe flow. *arXiv preprint arXiv:1905.12479*.

Shah, M. S., Joshi, J. B., Kalsi, A. S., Prasad, C., and Shukla, D. S. (2012). Analysis of flow through an orifice meter: Cfd simulation. *Chemical engineering science*, 71:300–309.

Simpson, R. L. (1989). Turbulent boundary-layer separation. *Annual Review of Fluid Mechanics*, 21(1):205–232.

Smits, A., Ding, L., and Van Buren, T. (2019). Flow over a square bar roughness. In *Proceedings of Turbulence and Shear Flow Phenomena*, volume 11.

Smits, A. and Wood, D. (1985). The response of turbulent boundary layers to sudden perturbations. *Annual Review of Fluid Mechanics*, 17(1):321–358.

Smits, A. J., Young, S., and Bradshaw, P. (1979). The effect of short regions of high surface curvature on turbulent boundary layers. *Journal of fluid mechanics*, 94(2):209–242.

Tomas, J., Pourquie, M., and Jonker, H. (2015). The influence of an obstacle on flow and pollutant dispersion in neutral and stable boundary layers. *Atmospheric Environment*, 113:236–246.

Van Buren, T., Floryan, D., Ding, L., Hellström, L., and Smits, A. (2020). Turbulent pipe flow response to a step change in surface roughness. *Journal of Fluid Mechanics*, 904.

Van Buren, T., Hellström, L., and Smits, A. (2019). Turbulent pipe flow response to rough-to-smooth step change in roughness: Flow structure. In *Proceedings of Turbulence and Shear Flow Phenomena*, volume 11.

Van Buren, T., Hellstrom, L. H., Marusic, I., and Smits, A. J. (2017). Turbulent pipe flow response to wall changes targeting specific azimuthal modes. In *Tenth International Symposium on Turbulence and Shear Flow Phenomena*. Begel House Inc.

Van der Kindere, J. and Ganapathisubramani, B. (2018). Effect of length of two-dimensional obstacles on characteristics of separation and reattachment. *Journal of Wind Engineering and Industrial Aerodynamics*, 178:38–48.

Versteeg, H. K. and Malalasekera, W. (2007). *An introduction to computational fluid dynamics: the finite volume method*. Pearson education.

Vold, M. (2017). Three-dimensional numerical modeling of water flow in a rock-blasted tunnel. Master's thesis, NTNU.

Von Kármán, T. (1963). *Aerodynamics*. McGraw-Hill paperbacks : Science, mathematics and engineering. McGraw-Hill.

Walters, D., Bhushan, S., Alam, M., and Thompson, D. (2013). Investigation of a dynamic hybrid rans/les modelling methodology for finite-volume cfd simulations. *Flow, turbulence and combustion*, 91(3):643–667.

White, F. M. and Corfield, I. (2006). *Viscous fluid flow*, volume 3. McGraw-Hill New York.

Wilcox, D. C. et al. (1998). *Turbulence modeling for CFD*, volume 2. DCW industries La Canada, CA.

Yamagata, T., Ito, A., Sato, Y., and Fujisawa, N. (2014). Experimental and numerical studies on mass transfer characteristics behind an orifice in a circular pipe for application to pipe-wall thinning. *Experimental thermal and fluid science*, 52:239–247.

Yin, G., Andersen, M., and Ong, M. C. (2020). Numerical simulations of flow around two tandem wall-mounted structures at high reynolds numbers. *Applied Ocean Research*, 99:102124.

Yin, G., Nitter, B., and Ong, M. C. (2021). Numerical simulations of turbulent flow through an orifice plate in a pipe. *Journal of Offshore Mechanics and Arctic Engineering*, 143(4):041903.

Zagarola, M., Smits, A., Orszag, S., and Yakhot, V. (1996). Experiments in high reynolds number turbulent pipe flow. In *34th Aerospace Sciences Meeting and Exhibit*, page 654.

Zagarola, M. V. and Smits, A. J. (1998). Mean-flow scaling of turbulent pipe flow. *Journal of Fluid Mechanics*, 373:33–79.